Microscopic Origin of Macroscopic Strength in Granular Media:
A Numerical and Analytical Approach

Thesis by
Alex Xavier Jerves Cobo

In Partial Fulfillment of the Requirements for the
degree of
Doctor of Philosophy

CALIFORNIA INSTITUTE OF TECHNOLOGY
Pasadena, California

2016
Defended April 13, 2016

Alex Xavier Jerves Cobo
ORCID: 0000-0002-6556-8727

ACKNOWLEDGEMENTS

I would like to begin by thanking the members of my thesis committee — Drs. José Andrade, Michael Ortiz, Oscar Bruno, and Domniki Asimaki — for their guidance, feedback, and advice during my time at Caltech. I am indebted to my advisor, Dr. José Andrade, for his patience, enthusiasm, support, and encouragement to pursue topics that I found truly original as well as exciting. In the same way, I would like to thank Reid Y. Kawamoto, Carlos F. Ávila, Sergio A. Galindo-Torres, Jaime D. Lopez, Pablo A. Torres, and Utkarsh Mital for their collaboration, feedback, and support throughout my research and life at Caltech.

I would also like to thank my family for the support they have given me throughout my entire life. In particular I must acknowledge my parents, Rubén and María Elena, for their encouragement, quiet patience, and unwavering love, as well as my brother, Rubén Fernando, for his invaluable support.

ABSTRACT

Constitutive modeling in granular materials has historically been based on macroscopic experimental observations that, while being usually effective at predicting the bulk behavior of these type of materials, suffer important limitations when it comes to understanding the physics behind grain-to-grain interactions that induce the material to macroscopically behave in a given way when subjected to certain boundary conditions.

The advent of the discrete element method (DEM) in the late 1970s helped scientists and engineers to gain a deeper insight into some of the most fundamental mechanisms furnishing the grain scale. However, one of the most critical limitations of classical DEM schemes has been their inability to account for complex grain morphologies. Instead, simplified geometries such as discs, spheres, and polyhedra have typically been used. Fortunately, in the last fifteen years, there has been an increasing development of new computational as well as experimental techniques, such as non-uniform rational basis splines (NURBS) and 3D X-ray Computed Tomography (3DXRCT), which are contributing to create new tools that enable the inclusion of complex grain morphologies into DEM schemes.

Yet, as the scientific community is still developing these new tools, there is still a gap in thoroughly understanding the physical relations connecting grain and continuum scales as well as in the development of discrete techniques that can predict the emergent behavior of granular materials without resorting to phenomenology, but rather can directly unravel the micro-mechanical origin of macroscopic behavior.

In order to contribute towards closing the aforementioned gap, we have developed a micro-mechanical analysis of macroscopic peak strength, critical state, and residual strength in two-dimensional non-cohesive granular media, where typical continuum constitutive quantities such as frictional strength and dilation angle are explicitly related to their corresponding grain-scale counterparts (e.g., inter-particle contact forces, fabric, particle displacements, and velocities), providing an across-the-scale basis for better understanding and modeling granular media.

In the same way, we utilize a new DEM scheme (LS-DEM) that takes advantage of a mathematical technique called level set (LS) to enable the inclusion of real grain shapes into a classical discrete element method. After calibrating LS-DEM with respect to real experimental results, we exploit part of its potential to study

the dependency of critical state (CS) parameters such as the critical state line (CSL) slope, CSL intercept, and CS friction angle on the grain's morphology, i.e., sphericity, roundness, and regularity.

Finally, we introduce a first computational algorithm to "clone" the grain morphologies of a sample of real digital grains. This cloning algorithm allows us to generate an arbitrary number of cloned grains that satisfy the same morphological features (e.g., roundness and aspect ratio) displayed by their real parents and can be included into a DEM simulation of a given mechanical phenomenon. In turn, this will help with the development of discrete techniques that can directly predict the engineering scale behavior of granular media without resorting to phenomenology.

PUBLISHED CONTENT AND CONTRIBUTIONS

J. E. Andrade et al. "Multiscale 'tomography-to-simulation' framework for granular matter: the road ahead". In: *Géotechnique Letters* 2 (2012), pp. 135–139. DOI: 10.1680/geolett.12.00023. URL: http://dx.doi.org/10.1680/geolett.12.00023.

Alex X. Jerves participated in the conception of the project, wrote a section of the manuscript, and contributed with figures.

Alex X. Jerves and José E. Andrade. "A micro-mechanical study of peak strength and critical state". In: *International Journal for Numerical and Analytical Methods in Geomechanics* (2015), pp. 1184–1202. ISSN: 1096-9853. DOI: 10.1002/nag.2478. URL: http://dx.doi.org/10.1002/nag.2478.

Alex X. Jerves participated in the conception of the project, derived all the equations, theories and formulations, ran the simulations, analyzed the data, wrote the the manuscript, and created the figures.

Alex X. Jerves, Reid Y. Kawamoto, and José E. Andrade. "Effects of grain morphology on critical state: a computational analysis". In: *Acta Geotechnica* (2015), pp. 1–11. ISSN: 1861-1133. DOI: 10.1007/s11440-015-0422-8.
URL: http://dx.doi.org/10.1007/s11440-015-0422-8.

Alex X. Jerves participated in the conception of the project, derived the theories and physical conclusions, analyzed the data, wrote the the manuscript, and created the figures.

Alex X. Jerves, Reid Y. Kawamoto, and José E. Andrade. "A geometry-based algorithm for cloning real grains". In: *Granular Matter* (2015), In review, GRMA-D-16-00064, 2016.

Alex X. Jerves participated in the conception of the project, derived the process and algorithm, ran the simulations, coded the algorithm, analyzed the data, wrote the of the manuscript, and created the figures.

TABLE OF CONTENTS

LIST OF ILLUSTRATIONS

Number *Page*

LIST OF TABLES

Chapter 1

INTRODUCTION

1.1 General Overview

Phenomenological and discrete modeling

Inhomogeneity and anisotropy are two fundamental properties of granular materials that make them very difficult to model and understand. Hence, granular modeling has been historically approached from three different perspectives, i.e., experiments, continuum mechanics, and grain-to-grain mechanics, making it sometimes difficult to have a well connected framework that includes these three approaches under a unique and comprehensive general theory. Fortunately, nowadays, the increasing computational power and new experimental techniques such as in situ 3D X-ray Computed Tomography (3DXRCT) [28] have given rise to new potential bridges that can contribute to connect micro (grain) and macro (continuum) scales by means of experimental, theoretical, and numerical tools that can be applied to the two physical scales [5, 6].

On the other hand, one of the main challenges in connecting experimental, discrete, and continuum modeling is precisely translating micro-scale physical features into their continuum counterparts. Hence, kinetics and topology at the grain scale have to be somehow related to continuum typical quantities such as strain and stress, or, in the constitutive sense, to mechanical parameters like internal friction and dilatancy. Thus, a fundamental question arises: what is the micro-mechanical origin of macro-mechanical behavior? Or, in other words: what is the fundamental information that is transmitted from scale to scale?

The inclusion of real grain morphology

Throughout the history of geomechanics, the role played by grain morphology in the physical behavior of granular media has been broadly accepted. However, even though some works [17, 49] have already looked into the connections between these two apparently different sides of the same phenomenological coin, there is still a handful of important relationships to be unraveled. Furthermore, due to the complex morphological characteristics of real grains, this subject has been mostly studied from the experimental setting, which, when effective, a good amount of time and resources need to be expended in designing, setting up, and running a given

experiment. This has always represented a major issue that has given rise to the use of emergent techniques such as computational simulation through mathematical models and numerical methods that, once validated and calibrated, can mimic the real experiment, allowing for the study of the same phenomena in a faster as well as less expensive way.

A series of explicit and implicit numerical models called discrete element methods (DEM) [23] has been widely used since the late 1970s to understand grain-to-grain interactions and their connections with the material's macroscopic behavior. Yet these numerical techniques face several limitations related to capturing the shapes and textures of real grains. Many models and assumptions ranging from polyhedral grain shapes [26, 1] to rotational constraints of the grains [60] have been used to account for the effects produced by real shapes in granular processes.

With the advent of new computational techniques, discrete element methods have also incorporated more sophisticated techniques such as particle clustering [27] that have allowed for better and more accurate approaches of reality. However, none of these techniques have completely succeeded in mimicking the effects of particle morphology as well as quantifying the amount of detail needed when capturing a real grain shape to obtain a similar quantitative and qualitative mechanical behavior to the one displayed by the real material. The combination of new experimental techniques (as the one mentioned in the last subsection) and mathematical representation of real shapes through the use of NURBS [44] has proven very effective but computationally costly, so more efforts are needed in order to gain computational efficiency with these new technologies, which, in turn, will allow us to quantify and qualify the dependency of macroscopic granular phenomena such as critical state on the grain morphology.

Approaching the engineering scale from the grain-scale

From a general point of view, it seems that the current gap between grain-scale modeling and continuum scale characterization is quite large. As imaging techniques are increasingly gaining sophistication and accuracy [61, 28], there continues to be a lack of effort on bringing discrete granular simulation techniques closer to the engineering scale and applications. In this regard and to our knowledge, there is only one pioneering work that includes discrete modeling of real granular materials at the grain scale [45]. However, the approach taken by the aforementioned work is restricted to combining discrete element and finite element schemes to model spe-

cific regions of interest with real shaped grain-to-grain interactions and then bypass the phenomenological information to a continuum constitutive model that governs the whole domain under study.

Therefore, at some point, discrete models with real grain shapes have to be able to directly match the so-called engineering scale as well as its potential applications. For this to happen, some other limitations have to first be overcome. For instance, on the experimental side, XRCT equipment is usually expensive, needs experienced technicians to be manipulated, and is not available at every institution around the globe for practical purposes, and the size of the scanned samples is limited to a few thousand grains. Hence, the emergent need for new computational tools capable of extracting the main morphological properties of a small sample of real grains and, with them, generating an arbitrary number of new real shaped grains with similar morphological properties that once included into a DEM simulation, this can be carried out at any desired scale, is limited only by the availability of computational power.

1.2 Motivation

An analytical-computational framework that can be used to study the connections between grain and continuum scales, isolating the effects of inter-particle contact forces, grain kinematics, and grain morphology/fabric on the macroscopic mechanical behavior of a given granular material (e.g. strength, dilation, and critical state), would help us to unravel fundamental mechanisms at the micro level that govern the strength build-up at the continuum scale. At the same time, this framework can take advantage of cutting-edge experimental and computational techniques such as 3D X-ray computed tomography (3DXRCT), non-uniform rational B-splines (NURBS), and level sets (LS), that for first time have enabled the development of new discrete element (DEM) schemes (e.g. NURBS-DEM, LS-DEM) capable of creating numerical avatars from a sample of real grains and including them into DEM simulations. Here the available digitalized information extracted from a real sample of a few thousand grains can be used to replicate some important morphological and geometrical features creating new digital grains with similar features. This would give us the capability of minimizing the dependency on real information (original real samples), while still being computationally able to generate as many grains with certain given real features as desired, thus taking discrete computational calculations and models to a new level that would directly approach the engineering scale by means of discrete computational techniques.

1.3 Research Objective

We look at the research objective in relation to the recent development of new experimental and computational techniques that have enabled the inclusion of real grain shapes in discrete element simulations such as 3D X-ray computed tomography (3DXRCT) [43] and level set (LS) methods [33]. These, in turn, have induced the development of new frameworks for the study of granular materials as is the case of the tomography-to-simulation framework [6], from which we take advantage in the present work to look deeper into the grain-scale physics behind the continuum behavior of a granular media.

The research objective is therefore to obtain new analytical expressions, trends, and computational tools that allow us to have a better understanding of the mechanical connections between grain-level quantities (e.g. contact forces and grain morphology) and continuum scale phenomenological parameters such as the ones describing strength, dilation, and critical state as shown by Figure 1.1.

Below, we list the main components required to meet this research objective.

1. **Analytical expressions:** The development of new analytical expressions relating continuum phenomenological parameters to grain level mechanics is a logical as well as necessary step to take as part of the tomography-to-simulation framework [6]. Analytical expressions not only enable us to make quantitative predictions but also are a formal crystallization of physical principles and laws that, at the same time, lend scientist and engineers the capability of extracting meaning by further studying them so more related phenomena can be understood and predicted. In specific, granular media mechanics requires more analytical expressions to be used as formal tools that provide a deeper understanding of the physical laws and connections that furnish the micro-mechanical origin of macroscopic strength, i.e., friction and dilation angles as well as critical state parameters.

2. **Trends and curves:** Looking for trends and correlations between two or more physical phenomena is also a necessary part when it comes to further understand the connections and relations that may or not exist among them. Moreover, finding the mentioned trends is, in fact, another step towards deriving new analytical expressions, that, as described in point 1 of this section, are important formal tools that help to develop as well as establish new paradigms and frameworks in science and engineering. In the present work,

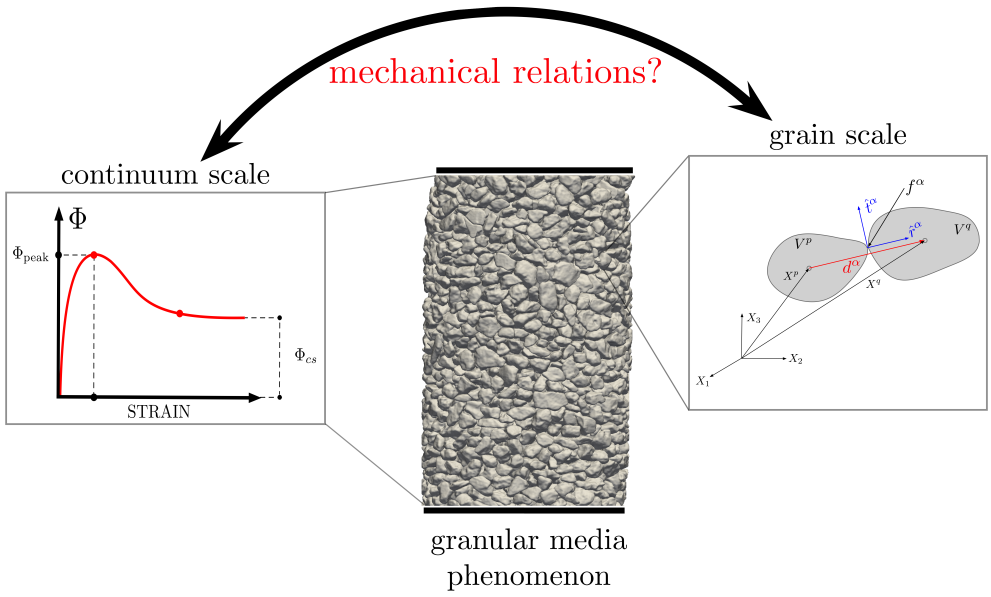

Figure 1.1: Micro origin of macro strength in granular media: this figure summarizes and describes the main objectives of the present work. A confined granular material develops shear strength, therefore displaying solid-like behavior. Thus, the granular material's strength Φ and related physical phenomena such as the case of dilation, whose origin is deeply related to the material's discrete nature, have been historically studied from a macroscopic/continuum point of view, without actually taking into account, in an accurate way, grain level features such as grain morphology, contact forces, and grain kinematics that furnish the phenomenology captured at the continuum level. Hence, the present work uses cutting-edge computational tools to unravel some of the most fundamental physical connections between the grain and continuum scale levels from an analytical point of view, as well as to keep pushing the envelope towards more advanced computational techniques of representing and reproducing (cloning) the core morphological features that make a specific granular medium display particular mechanical features.

we look for trends that relate grain morphology (roundness and sphericity) to critical state parameters (critical state line slope, critical state line intercept, and critical state friction angle). Then, these trends can be used in future works to derive new analytical expressions that help to understand physical laws and governing connections between these two scales at critical state.

3. **Computational tools:** The constant development of tools that help to improve and enrich a new framework such as tomography-to-simulation [6] is an important task towards providing it with all the necessary joints that help to connect and articulate all its parts. Since the aforementioned framework

includes experimental, analytical, and computational tools, an objective of the present work is also to provide it with new computational tools that enhance its current capabilities. Specifically, we look into the development of a "cloning" process that, departing from a sample of a few thousand real grains enables us to "create" an arbitrary number of new digital grains that have similar morphological properties, so discrete calculations with real-like shapes can be taken to a new level that approaches the continuum scale directly from the use of discrete methods.

1.4 Contribution

The contribution of the work described in this thesis is the development of a new analytical-computational framework to study the physical relations between grain and continuum scales. On the analytical side we have derived expressions and trends that relate macroscopic parameters such as fraction angle, dilation angle, and critical state parameters to grain-scale quantities such as contact forces and grain morphology/fabric. At the same time, these expressions and trends have allowed us to understand fundamental mechanisms at the grain level, which furnish the physics displayed at the continuum scale (e.g. buckling of contact points and rotational mechanisms directly related to peak strength and volume preservation, or the influence of morphological details on critical state parameters). On the computational side we have used cutting-edge discrete element (DEM) schemes such as LS-DEM to carry out part of our analytical studies as well as introduced a first geometric stochastic cloning (GSC) algorithm to digitally "clone" real grain shapes. This algorithm reduces the dependency of computations that include real grain shapes on the amount of real grain images obtained from a 3D X-ray computed tomography (3DXRCT) by enabling us to generate an arbitrary number of new digital grains that satisfy the same morphological features as the once yielded by their real counterparts.

1.5 Overview of Thesis

This thesis is organized as follows:

In Chapter 2, analytical expressions connecting macroscopic parameters, namely, friction Φ and dilation Ψ angles to grain scale quantities such as inter-particle contact forces $\boldsymbol{f}^{\alpha}$, brach vectors (fabric) $\boldsymbol{d}^{\alpha}$, and grain kinematics $\boldsymbol{u}^{\alpha}$, $\dot{\boldsymbol{u}}^{\alpha}$ are derived. Hence, further analyses are carried out and two necessary and sufficient conditions for peak strength Φ_{peak} are obtained at the continuum and grain levels. In the same

way, we use analytical expressions to study the micro-mechanisms that furnish the volume preserving condition at critical state, i.e., rotational modes and inter-particle friction independence.

In Chapter 3, a two-dimensional analysis of the connections between grain morphology (roundness and sprericity) and macroscopic critical state parameters, namely, critical state friction angle Φ_{cs}, critical state line slope λ, and critical state line intercept Γ is carried out numerically by taking advantage of state-of-the-art experimental and numerical technics such as 3D X-ray computed tomography (3DXRCT) and level set schemes (LS) that, combined with a classical discrete element method (DEM), enable us to computationally simulate grain-to-grain interactions that include real grain shapes. Hence, we derive trends that provide us with a deeper insight into the relations between the aforementioned morphological and critical state parameters. Similarly, the effect of "imperfections" on real grains is studied by carrying out similar DEM simulations with idealized/simplified grains, which are morphologically equivalent to their real counterparts.

Chapter 4 introduces a first geometric stochastic cloning (GSC) algorithm to "clone" real grain shapes. This algorithm is based on the statistical distributions of morphological features such as aspect ratio, minimum principal directions, spherical radius, and roundness, which are digitally extracted from a parent sample of real grains obtained by combining 3D X-ray computed tomography (3DXRCT) and level sets (LS). The algorithm generates new real shaped grains (clones) that follow the same morphological patterns of the real grains in the parent sample. For this, a stochastic sampling method such as the acceptance-rejection Monte-Carlo scheme is used together with a laplacian (curvature) based smoother. In turn, this cloning algorithm enables us to (departing from a real parent sample with a few thousand grains) generate an arbitrary number of new grains that display similar morphological characteristics.

Finally, Chapter 5 summarizes some key developments of this dissertation. In the same way, limitations of the current work are discussed as well as future directions of research are given. To make this thesis flow better, content repetition is minimized as much as possible.

This thesis is mostly based on published journal articles [6, 32, 33]. However, there may be some repetition of concepts as in the case of Chapter 4, which is in the process of being published as a journal article as well.

Chapter 2

A MICRO-MECHANICAL STUDY OF PEAK STRENGTH AND CRITICAL STATE

Published on: *International Journal for Numerical and Analytical Methods in Geomechanics* [32].

2.1 Introduction

Continuum and discrete modeling of confined granular materials have been two intensively studied and developed fields in the past 50 years. In the case of continuum modeling, we can trace pioneering works on dilation all the way back to the last part of the 19th century [71], or even to the last part of the 18th century for works on granular strength [21]. Thus, these foundational works gave rise to an increasingly number of fundamental publications along the 20th century [55, 25, 40, 48]. On the other hand, discrete modeling can be traced back to the origins of newtonian mechanics [57]. However, discrete modeling of confined granular materials was not truly exploited until the end of the 1970's with the advent of a simple but powerful computational tool known as the discrete element method (DEM) [23]. With this tool and the availability of better computational capabilities, in terms of processing and memory, the simulation of actual arrays of particles was made possible and available for the scientific community for first time. Thus, ever since the late 1970s, important contributions on modeling and understudying the governing physics of the grain scale have been made [78, 79, 2, 59].

A third field has emerged as a consequence of the advances in continuum and discrete modeling of granular materials. This new area of study attempts to find connections and relations between the continuum (macro) and discrete (micro) scales, so it goes 'multi-scale', and specially, continuum modeling can be enhanced with fundamental information gathered from the micro-scale. Pioneering as well as essential contributions have been made in this regard to connect stress, strain, and stiffness to the grain-scale, or to measure the impact of orthotropicity and inhomogeinity inherent to granular materials [46, 90, 74, 16, 39, 59, 15]. Discrete simulation and experimentation have also been used to study and understand granular behavior from a qualitative and statistical point of view. For instance, Radjaï and Roux [29] have worked on critical state and hysteric processes in two dimen-

sional granular materials using DEM simulation, or Mooney et al. [56] have carried out similar work from the experimental setting. Thus, the mentioned works have established a strong theoretical and experimental foundation for a new framework in which further studies can be carried out. Hence, in the present work, and taking advantage of the aforementioned framework, we aim for an enhancement of our physical knowledge about the material's behavior at its most fundamental scale through a deeper analysis of the mechanisms acting at the grain-scale level and inducing strength. In other words, we attempt to add a couple of words to the answer of a very fundamental question, namely: how does the grain-scale affect the macroscopic behavior?

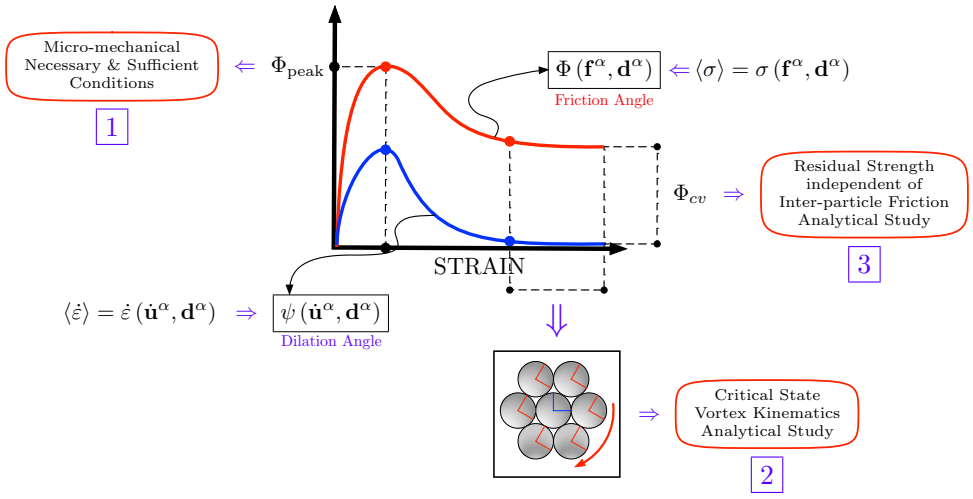

Figure 2.1: Pictorial sketch of the subjects tackled by the present work and its corresponding contributions.

Based on the multi-scale philosophy just described, the objective of this work is, as shown by Figure 3.6, to connect three basic grain-scale properties, i.e., contact forces $\boldsymbol{f}^{\alpha}$, fabric $\boldsymbol{d}^{\alpha}$, and contact velocities $\dot{\boldsymbol{u}}^{\alpha}$, to two fundamental macro-mechanical constitutive quantities such as strength Φ, and dilation ψ. Thus, we aim to get a few steps closer towards answering the ultimate question: *what are the main microscopic mechanisms inducing macroscopic peak strength, critical state, and residual strenght?* Hence, we begin the present work by investigating the micro-mechanics of two essential macroscopic physical quantities: average stress $\langle\boldsymbol{\sigma}\rangle$, and average strain rate $\langle\dot{\boldsymbol{\varepsilon}}\rangle$. Explicit expressions for these two quantities in terms of contact forces, fabric, and contact velocities are used [9, 80, 46, 90, 74, 18, 59], and derived in the case of the average strain rate. Once these micro-macro relations have

been established, we are able to connect micro-mechanics to strength and dilation via the non-associative Mohr-Coulomb failure criterion, where stress and strain rate invariants (deviatoric and volumetric) are directly related to the material's strength $\tau_{\max} = \bar{p}\sin(\Phi)$, and dilation $\dot{\varepsilon}_v \approx 2\,\dot{\varepsilon}_s \sin(\psi)$, as shown by Figures 2.8 and 4.3. Consequently, explicit expressions for hydrostatic pressure $\bar{p}$, maximum shear $\tau_{\max}$, and dilation angle ψ, in terms of contact forces, fabric, and contact velocities are obtained. This takes us to the heart of the present work, where, as depicted by Figure 3.6: First, two conditions for peak strength Φ_{peak} are inferred, and for which, corresponding grain-scale expressions are found. Second, vortex-like micro-mechanical mechanisms furnishing critical state (or steady state) [51, 19] are unraveled analytically in terms of grain-scale kinematics. Third, the sensitiveness and independence of these vortex-like mechanisms on the inter-particle friction coefficient μ, for low and high enough values of μ, respectively, is proven analytically. This, at the same time, is directly related to the sensitiveness and independence of the residual strength Φ_{cv}, on low and high enough values of μ [66]. These conditions and expressions provide us with a deeper insight into mechanisms governing peak strength such as buckling and high frictional activity as well as a broader physical understanding of the sensitivity and independence of residual strength on the values of the inter-particle friction coefficient μ.

Hence, the key contribution of the work presented here is the enhancement of the theoretical knowledge about the micro-mechanisms inducing and governing peak strength, critical state and residual strength in confined non-cohesive two-dimensional polydisperse packings undergoing loading conditions.

Finally, in order to validate the analytical expressions, physical interpretations, and the concepts developed in the present work, we use Discrete Element Modeling (DEM) [23] to simulate two types of assemblies: a polydisperse sample, and a similar packing but surrounded by a regular boundary belt (see: Section 4.4, for more details). The 'experiments' are detailed and illustrated at the end of each section.

2.2 Macro-strength and micro-mechanics

Let us begin the discussion by introducing an expression that enables us to compute the average Cauchy stress [18] of an sample of particles as a function of the inter-particle contact forces and the corresponding branch vectors (see Figure 4.2(a)). This expression is given by

$$\langle \boldsymbol{\sigma} \rangle = \frac{1}{V} \sum_{\alpha=1}^{Nc} \boldsymbol{d}^{\alpha} \otimes \boldsymbol{f}^{\alpha} \tag{2.1}$$

where $\langle \boldsymbol{\sigma} \rangle$ is the sample's average stress, V is the sample's total volume, and the branch vector, $\boldsymbol{d}^{\alpha}$, at the α-th contact point (vector connecting the centroids of two particles in contact at the α-th contact point, see Figure 4.2(a)) is expressed in components as $\boldsymbol{d}^{\alpha} = d_1^{\alpha}\hat{\boldsymbol{e}}_1 + d_2^{\alpha}\hat{\boldsymbol{e}}_2 = |\boldsymbol{d}^{\alpha}|\cos(\delta^{\alpha})\,\hat{\boldsymbol{e}}_1 + |\boldsymbol{d}^{\alpha}|\sin(\delta^{\alpha})\,\hat{\boldsymbol{e}}_2$, where δ^{α} is the angle between $\boldsymbol{d}^{\alpha}$ and the x-axis (global frame of reference), and $\hat{\boldsymbol{e}}_1$, $\hat{\boldsymbol{e}}_2$ are the basis vectors corresponding to the x and y directions, respectively, of the mentioned global (cartesian) frame of reference.

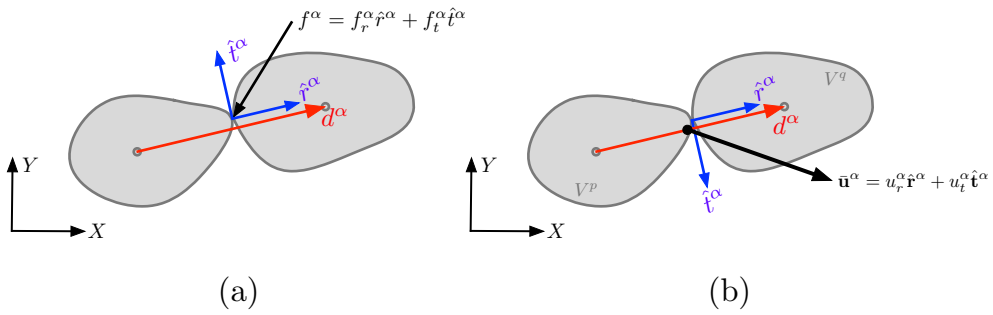

Figure 2.2: Inter-particle contact force represented in its normal and tangent (to the contact point) components. (b): Inter-particle average displacement represented in its normal and tangent (to the contact point) components, which, in this case, are placed so the tangent component points outwards of the counterclockwise oriented CCB (see: Figure 2.7).

Moreover, as shown in Figure 4.2(a), we also use local, normal, $\hat{\boldsymbol{r}}^{\alpha}$, and tangent, $\hat{\boldsymbol{t}}^{\alpha}$, coordinates at each contact point. Hence, we are now able to express the α-th contact force as $\boldsymbol{f}^{\alpha} = f_r^{\alpha}\hat{\boldsymbol{r}}^{\alpha} + f_t^{\alpha}\hat{\boldsymbol{t}}^{\alpha}$, where $\hat{\boldsymbol{r}}^{\alpha} = \sin(\phi^{\alpha})\hat{\boldsymbol{e}}_1 - \cos(\phi^{\alpha})\hat{\boldsymbol{e}}_2$, $\hat{\boldsymbol{t}}^{\alpha} = \cos(\phi^{\alpha})\hat{\boldsymbol{e}}_1 + \sin(\phi^{\alpha})\hat{\boldsymbol{e}}_2$, and ϕ^{α} is the angle between the unit vector tangent to the α-th contact point, $\hat{\boldsymbol{t}}^{\alpha}$, and the x-axis (global frame of reference).

Thus, the tools that we have defined and described so far will be used in the following sections to *derive micro-mechanical expressions and conditions for peak strength that, at the same time, will allow us to obtain meaningful physics* that can help us to improve our understanding about the role played by quantities such as contact forces and fabric on the build up of macroscopic peak strength of confined granular arrays under loading conditions.

Mohr-Coulomb and friction angle

At the core of classical constitutive modeling of granular materials we find the Mohr-Coulomb [14] failure criterion which, in the two-dimensional case, is described by the expression: $\tau_{\max} = \sigma \tan(\Phi) + c$, as shown in Figure 2.8. Here, $\tau_{\max}$ is the maximum shear stress, $\bar{p}$ is the hydrostatic pressure, Φ is the so-called internal friction angle, and c is the cohesion inherent to the granular material being modeled. It is clear that the Mohr-Coulomb criterion defines a line of material state (represented by $\tau_{\max}$ and $\bar{p}$) and what are now seen as fundamental constitutive properties such as friction angle Φ and cohesion c. In this work, we will focus on cohesionless materials and therefore assume $c = 0$.

Furthermore, using Figure 2.8, we recall the definition of macroscopic friction angle and its relation to principal stresses, namely,

$$\sin(\Phi) = \frac{\tau_{\max}}{\bar{p}} = \frac{\Lambda_1 - \Lambda_2}{\Lambda_1 + \Lambda_2} \quad , \quad 0 \leq \sin(\Phi) < 1 \tag{2.2}$$

This last expression in combination with the tools and concepts described at the beginning of this section (see equation (2.1), Figure 4.2, and their corresponding discussion) will allow us in the following subsection (2.2) to explicitly link macroscopic strength, Φ, to micro-mechanical quantities such as contact forces and fabric, and ultimately, unravel micro-mechanical conditions for macroscopic peak strength Φ_{peak}.

Peak strength

Linked to the important property of *mobilized friction angle*, is the concept of a limiting or *peak friction angle*, as depicted in Figure 2.3. The peak or limiting friction angle Φ_{peak} *represents the ultimate frictional strength that can be mobilized by a material under given density and confinement*. This ultimate macroscopic frictional strength as well as its links to grain-scale mechanics has been extensively studied and understood in the last decades, going from very specific cases such as works on regular packings [75, 84] to more general works [50, 88, 72]. However, a fundamental question remains to be answered: *what are the specific micro-mechanical processes or conditions that make an assembly of confined particles reach macroscopic peak strenght* Φ_{peak} *when undergoing loading?* Generalization of previous cited works is still required to shed light into the aforementioned question.

Thus, in this subsection, we look for ways of generalizing the previous work for

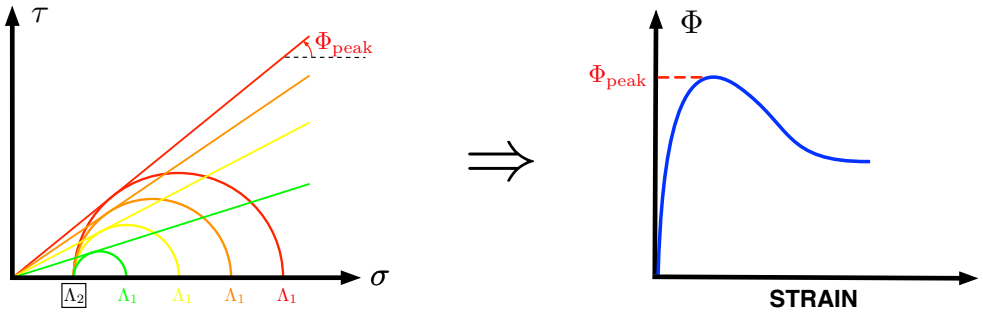

Figure 2.3: Limit friction angle, Φ_{peak}, defined as the maximum strength reached by a given assembly of granular materials as Λ_2 is kept constant while Λ_1 increases quasi-statically.

more sophisticated two-dimensional arrays where arbitrary size discs (polydispersity), and arbitrary shape particles are included. To begin with this analysis, note that $\dot{\Phi} = 0 \;\Rightarrow\; \overline{\sin\left(\Phi\right)}^{\cdot} = 0$. Then, maximizing the right-hand-side of equation (2.2) in time ($\overline{\tau_{\max}/\bar{p}}^{\cdot} = 0$), we obtain

$$\frac{d\bar{p}}{\bar{p}} = \frac{d\tau_{\text{peak}}}{\tau_{\max}} \quad \Rightarrow \quad \sin\left(\Phi_{\text{peak}}\right) = C \quad \Rightarrow \quad \underbrace{\Lambda_1^{\text{peak}} = K\Lambda_2}_{\substack{\text{Mohr-Coulomb} \\ \text{failure criterion}}}$$

where C and K are constant values. Thus, to simplify our analysis (but without losing generality), we take the bi-axial loading case in which one of the loads, Λ_2, is kept constant, while the other, Λ_1, is increased quasi-statically as shown in the left part of Figure 2.3. Hence, maximizing $\sin\left(\Phi\right)$ in time (see equation (2.2)) gives us

$$\overline{\frac{\Lambda_1 - \Lambda_2}{\Lambda_1 + \Lambda_2}}^{\cdot} = 0 \quad \Rightarrow \quad \dot{\Lambda}_1 \underbrace{\Lambda_2}_{\text{arbitrary}} = 0 \quad \Rightarrow \quad \boxed{\dot{\Lambda}_1 = 0}$$

Now, note from Figure 2.8 (Mohr's circle [62]) that $\Lambda_1 = \bar{p} + \tau_{\max}$, so applying our last result ($\dot{\Lambda}_1 = 0$) to this expression, we find that at maximum strength: $\dot{\bar{p}} + \dot{\tau}_{\max} = 0$. However, from the left part of Figure 2.3, note that in the case of monotonic loading, and until reaching peak strength: $\dot{\Lambda}_1,\ \dot{\bar{p}},\ \dot{\tau}_{\max} \geq 0$. From the current analysis, we therefore obtain two necessary and sufficient conditions that must be satisfied, namely

$$\boxed{\dot{\bar{p}} = 0 \quad \text{and} \quad \dot{\tau}_{\max} = 0} \tag{2.3}$$

These semi-Lagrangian conditions imply that when the peak strength, Φ_{peak}, is reached in bi-axial loading conditions, not only is Λ_1 at its maximum, but $\bar{p}$ and $\tau_{\max}$ also reach their maximum values.

Now, let's try to understand the meaning and implications of these two macroscopic necessary and sufficient conditions for maximum strength, from the micro-mechanical point of view, where inter-particle contact forces, and fabric are the main variables governing the physical behavior. Applying the local frame of reference described by Figure 4.2(a) to expressions (2.1), we have that

$$\bar{p} = \frac{1}{2V}\sum_{\alpha=1}^{Nc}|\boldsymbol{d}^{\alpha}|[f_r^{\alpha}\sin(\phi^{\alpha}-\delta^{\alpha}) + f_t^{\alpha}\cos(\phi^{\alpha}-\delta^{\alpha})]$$

$$\tau_{\max} = \frac{1}{2V}\sqrt{\left\{\sum_{\alpha=1}^{Nc}|\boldsymbol{d}^{\alpha}|[f_r^{\alpha}\sin(\phi^{\alpha}+\delta^{\alpha}) + f_t^{\alpha}\cos(\phi^{\alpha}+\delta^{\alpha})]\right\}^2}$$

$$\overline{+\left\{\sum_{\alpha=1}^{Nc}|\boldsymbol{d}^{\alpha}|\,[f_r^{\alpha}\cos(\phi^{\alpha}+\delta^{\alpha}) - f_t^{\alpha}\sin(\phi^{\alpha}+\delta^{\alpha})]\right\}^2}$$

Combining these last equations with conditions (2.3), we arrive at

$$\boxed{\sum_{\alpha=1}^{Nc}\dot{f}_1^{\alpha}d_1^{\alpha} = 0 \quad \text{and} \quad \sum_{\alpha=1}^{Nc}\dot{f}_2^{\alpha}d_2^{\alpha} = 0} \iff \boxed{\sum_{\alpha=1}^{Nc}|\boldsymbol{d}^{\alpha}|\,\dot{f}_r^{\alpha} = 0 \quad \text{and} \quad \sum_{\alpha=1}^{Nc}\boldsymbol{d}^{\alpha}\times\dot{\boldsymbol{f}}_t^{\alpha} = 0} \tag{2.4}$$

which have to be satisfied at peak strength, and are the micro-mechanical counterpart of conditions (2.3). Furthermore, note that we assume that, at peak strength, most of the fabric does not present significant changes from its original configuration at the beginning of the loading process, so $|\dot{\boldsymbol{f}}^{\alpha}|\,|\boldsymbol{d}^{\alpha}| \gg |\boldsymbol{f}^{\alpha}|\,|\dot{\boldsymbol{d}}^{\alpha}|$. This condition holds for sufficiently dense packings undergoing quasi-static bi-axial loading.

We still can go deeper into our microscopic analysis of peak strength. Provided that the assumptions of constant fabric made in the last paragraph hold, the only way in which conditions (2.4) can hold, is if $\dot{\boldsymbol{f}}^{\alpha} \approx 0$ contactwise. From numerical experimentation (as shown in the examples below), we have that at peak strength

$$\boxed{\sum_{\alpha=1}^{Nc}\left|f_1^\alpha\right| \;,\; \sum_{\alpha=1}^{Nc}\left|f_2^\alpha\right| \;,\; \sum_{\alpha=1}^{Nc} f_r^\alpha \;,\; \sum_{\alpha=1}^{Nc}|f_t^\alpha| \quad \text{are maximum @ peak}} \tag{2.5}$$

The two first results can be interpreted as buckling conditions for a two-dimensional array implying that when peak strength is reached, the sum of its vertical contact forces reaches its "critical value", in analogy with classical column theory. The third result shows that when peak strength is reached, the array also achieves its maximum confining pressure. This result is consistent with the last result (provided a Coulomb friction like law, $\left|f_t^\alpha\right| = \mu f_r^\alpha$, holds for the normal and tangent components of the contact forces), where, if the normal contact forces, f_r^α, are maximum, a peak value in the tangent contact forces, f_t^α, is also expected. Thus, this last result also implies very high dissipative activity when peak strength is reached as will be further studied as well as shown in examples 2.2 and 2.3.

Example

In this example we have a two-dimensional polydisperse packing (see Figure 2.4 (Left)) composed of 1438 discs with average diameter of 0.6 units, and ±66.74% of polydispersity. The discs have an inter-particle friction coefficient of $\mu = 0.5$ [69], and a friction coefficient of $\mu_w = 1E^{-6}$ on all the walls. The sample departs from a hydrostatic state of stress of 100 units of pressure and then undergoes quasi-static axial loading along the vertical axis while keeping the horizontal stress constant. This numerical experiment is carried out by using an implicit DEM scheme [35], where: $k_r = k_t = 7.5E^4$ (units of force per unit of length) are the effective normal and tangent stiffness, respectively, $\dot{u}_2 = 7.5E^{-5}$ (units of length per unit of time) is the vertical loading velocity at the upper wall, and $\theta = 1$ is a numerical integration parameter and restitution coefficient (backward Euler and perfectly inelastic collision, respectively). The peak friction angle yielded by this simulation is $\Phi_{\text{peak}} = 29.25°$, as shown by Figure 2.4 (Right).

For this example, as illustrated by Figures 2.4 (Right) and 2.5 in agreement with the peak strength micro-mechanical conditions given by expression (2.5): friction angle Φ, $\sum_{\alpha=1}^{Nc} f_r^\alpha$, and $\sum_{\alpha=1}^{Nc}\left|f_t^\alpha\right|$ arrive at their respective maximum values at $\sim 3.56\%$ of axial strain. Then, according to Figure 2.5, once the array leaves maximum strength, $\sum_{\alpha=1}^{Nc} f_r^\alpha$ and $\sum_{\alpha=1}^{Nc}\left|f_t^\alpha\right|$ exhibit a sharp softening process, which is similar to that observed for the friction angle Φ. Thus, towards 9% of axial strain, the onset of the steady-state is observed. Moreover, note that according to the peak strength

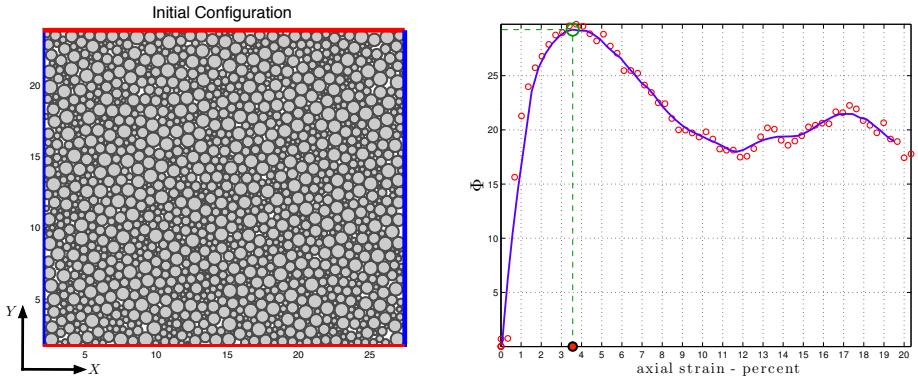

Figure 2.4: Left: Polydisperse packing of 1438 discs with inter-particle friction coefficient, $\mu = 0.5$, in a square container ($\sim 25.303 \times 22.15$ square units) with frictionless walls, and subject to quasi-static axial loading parallel to the vertical axis. The sample departs from an initially hydrostatic loading state of 100 units of pressure. Right: Graph of the evolution of the mobilized friction angle, Φ versus axial strain (percentage).

micro-mechanical conditions in equation (2.5) and Figures 2.4 (Right), 2.5 (Right), together with Coulomb's friction law ($\left|f_t^\alpha\right| \leq \mu f_r^\alpha$), we conclude that maximum dissipation occurs at the same time as peak strength Φ_{peak}, i.e., the largest number of sliding contact points along the entire loading process and/or the maximum value of the corresponding tangent components occur when peak strength is reached.

For the horizontal and vertical inter-particle contact forces, as depicted by Figures 2.4 (Right) and 2.6, $\sum_{\alpha=1}^{Nc}\left|f_1^\alpha\right|$ and $\sum_{\alpha=1}^{Nc}\left|f_2^\alpha\right|$ also satisfy the peak strength conditions (2.5). However, the behavior in this case is in contrast with that presented by Figure 2.5. Here, the value of $\sum_{\alpha=1}^{Nc}\left|f_2^\alpha\right|$ decays faster than $\sum_{\alpha=1}^{Nc}\left|f_1^\alpha\right|$, suggesting "buckling" of the assembly (total lost of the original fabric configuration and onset of flow), with its consequent drop in the lateral confinement and corresponding loss of strength.

2.3 Critical state and micro-kinematics

Having studied and unraveled some of the links between peak strength and its corresponding micro-mechanical mechanisms in terms of contact forces and fabric, we now attempt to touch upon *the micro-kinematical mechanisms governing the so-called critical state*, which, at the continuum level, depends directly on another important parameter, namely, *dilation*. However, unlike internal friction, which is directly dependent on the stress, dilation is better described as a kinematic phe-

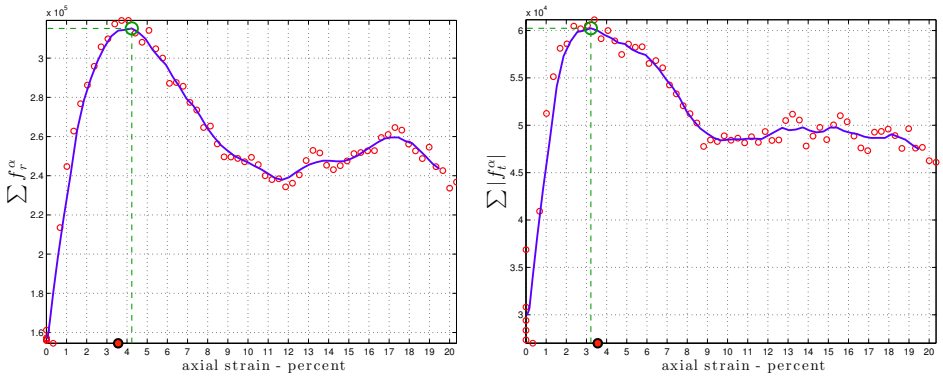

Figure 2.5: For the assembly in Figure 2.4 (Left). Left: Sum of the normal components of the contact forces, $\sum_{\alpha=1}^{Nc} f_r^\alpha$, versus axial strain (percentage). Right: Sum of the tangent components of the contact forces (in absolute value), $\sum_{\alpha=1}^{Nc} \left|f_t^\alpha\right|$, versus axial strain (percentage). The red dot with black boundary on the axial strain axis shows the actual value at which the friction angle reaches its peak Φ_{peak} (see: Figure 2.4 (Right))

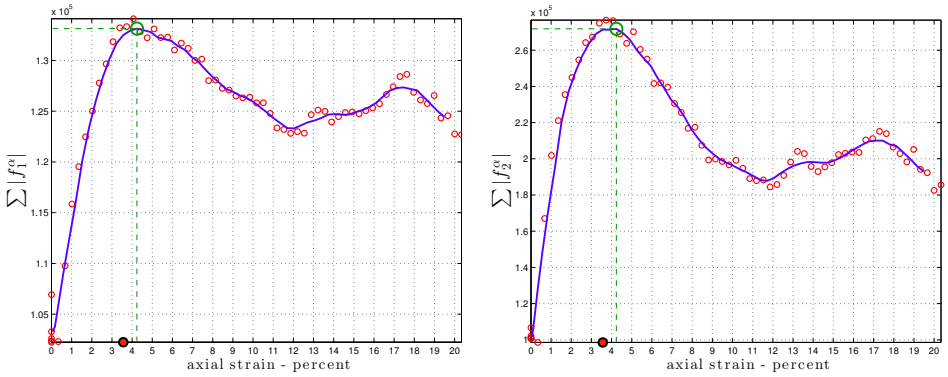

Figure 2.6: For the array in Figure 2.4 (Left). Left: Sum of the horizontal components of the contact forces, $\sum_{\alpha=1}^{Nc} \left|f_1^\alpha\right|$, versus axial strain (percentage). Right: Sum of the vertical components of the contact forces (in absolute value), $\sum_{\alpha=1}^{Nc} \left|f_2^\alpha\right|$, versus axial strain (percentage). The red dot with black boundary on the axial strain axis shows the actual value at which the friction angle reaches its peak Φ_{peak} (see: Figure 2.4 (Right))

nomenon that involves plastic volume changes [92], as illustrated by Figure 4.3. Thus, neglecting elastic strain rates we can directly connect dilatancy to the total strain rates, which we assume as plastic. Hence, in order to link dilation to its micro-kinematical counterparts, we begin this section with the derivation of a new

expression [10, 8, 91] that enables us to explicitly relate the *average strain rate* $\langle\dot{\boldsymbol{\varepsilon}}\rangle$ of an assembly of particles to micro-kinematical quantities such as *branch vectors* $\boldsymbol{d}^{\alpha}$ and *velocities* $\boldsymbol{v}^{\alpha}$ (or $\dot{\boldsymbol{u}}^{\alpha}$).

Here, we define the small strain rate tensor as in [93]:

$$\dot{\boldsymbol{\varepsilon}} := \frac{1}{2}(\boldsymbol{v}\otimes\boldsymbol{\nabla} + \boldsymbol{\nabla}\otimes\boldsymbol{v}) \tag{2.6}$$

Now, using equation (2.6), we can compute the average strain rate $\langle\dot{\boldsymbol{\varepsilon}}\rangle$ of a domain Ω with boundary $\partial\Omega$, with corresponding volume V and surface S,

$$\langle\dot{\boldsymbol{\varepsilon}}\rangle = \frac{1}{2V}\int_{\partial V}(\boldsymbol{v}\otimes\hat{\boldsymbol{n}} + \hat{\boldsymbol{n}}\otimes\boldsymbol{v})dS \tag{2.7}$$

where the identity $\nabla\cdot(\boldsymbol{v}\otimes\boldsymbol{I}) = (\boldsymbol{v}\otimes\boldsymbol{\nabla})\cdot\boldsymbol{I} + \boldsymbol{v}\otimes(\boldsymbol{\nabla}\cdot\boldsymbol{I}) = \boldsymbol{v}\otimes\boldsymbol{\nabla}$ and then the divergence theorem has been applied. Then, discretizing expression (2.7) for two-dimensional granular media whose boundary particles are successively in contact with the following particle as links of a closed chain or loop (closed-connected boundary or CCB), as shown by Figure 2.7, we arrive at the following expression:

$$\boxed{\langle\dot{\boldsymbol{\varepsilon}}\rangle = \frac{1}{V^{CCB}}\sum_{\alpha=1}^{Nc^{CCB}}|\boldsymbol{d}^{\alpha}|\mathrm{sym}(\boldsymbol{v}^{\alpha}\otimes\hat{\boldsymbol{t}}^{\alpha})} \tag{2.8}$$

where, V^{CCB} is the volume (area) enclosed by the CCB, Nc^{CCB} is the number of inter-particle contact points contained by the CCB and equal to the number of particles contained by the CCB (only for the two-dimensional case). In the same way, $|\boldsymbol{d}^{\alpha}|$ is the length of the branch vector corresponding to the α-th inter-particle contact point in the CCB, and

$$\boldsymbol{v}^{\alpha} = \frac{1}{2}(\boldsymbol{v}^{p,\alpha} + \boldsymbol{v}^{q,\alpha}) \quad , \quad \boldsymbol{v}^{p,\alpha} = \frac{\partial}{\partial t}\boldsymbol{x}_c^{p,\alpha} \quad , \quad \underbrace{\hat{\boldsymbol{t}}^{\alpha} = \sin(\delta^{\alpha})\hat{\boldsymbol{e}}_1 - \cos(\delta^{\alpha})\hat{\boldsymbol{e}}_2}_{\text{for discs}}$$

where, the super indices p and q represent the "master" (or basis) and "slave" particles in contact, respectively, at the α-th contact point of the CCB, and the sub-index c, represents the centroid of the particle. Finally, $\hat{t}^{\alpha}$ is the outword unit normal to the branch vector $\boldsymbol{d}^{\alpha}$ as shown by Figure 4.2(a). Also, note that

$$\boldsymbol{u}^{p,\alpha} = \boldsymbol{x}_c^{p,\alpha} - \boldsymbol{X}_c^{p,\alpha} \quad , \quad \boldsymbol{u}^{\alpha} = \frac{1}{2}(\boldsymbol{u}^{p,\alpha} + \boldsymbol{u}^{q,\alpha}) \quad , \quad \boldsymbol{v}^{p,\alpha} = \frac{\partial}{\partial t}\boldsymbol{u}^{p,\alpha} = \frac{\partial}{\partial t}\boldsymbol{x}_c^{p,\alpha}$$

where, the superindices p and q denote the master and slave particles at the α-th contact point in the CCB, the subindex c denotes the centroid of the particles, and $\boldsymbol{X}$

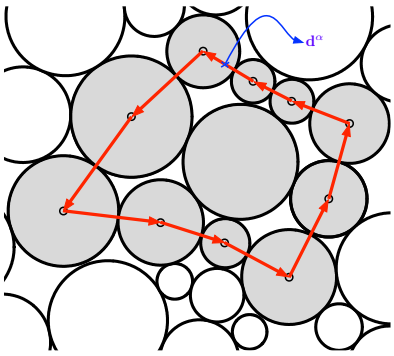

Figure 2.7: Closed-connected and counterclockwise oriented path corresponding to the gray discs domain's "boundary".

is the position of the centroid of the particles in the CCB at the initial configuration. Furthermore, as shown in Figure 4.2(b), we use local: normal and tangent coordinates at each contact point. Thus, from the aforementioned Figure, note that $\boldsymbol{u}^{\alpha} = u_r^{\alpha}\hat{\boldsymbol{r}}^{\alpha} + u_t^{\alpha}\hat{\boldsymbol{t}}^{\alpha}$, with corresponding time derivative $\dot{\boldsymbol{u}}^{\alpha} = \dot{u}_r^{\alpha}\hat{\boldsymbol{r}}^{\alpha} + u_r^{\alpha}\dot{\hat{\boldsymbol{r}}}^{\alpha} + \dot{u}_t^{\alpha}\hat{\boldsymbol{t}}^{\alpha} + u_t^{\alpha}\dot{\hat{\boldsymbol{t}}}^{\alpha}$.

Hence, the tools defined, derived, and described so far in this section will be used in the following subsections to study, from the micro-kinematical point of view, mechanisms and conditions for critical state and consequent residual strength, while extracting physics that will help us understand the mentioned micro-kinematical conditions and mechanisms and its role regarding dilation evolution in confined granular media undergoing loading.

Moreover, it is worth mentioning that choosing different CCBs for equation (2.8) might not yield the same results since the domain bounded by each CCB might change drastically in shape and number of contained particles. However, additivity of the strains computed from two or more neighboring CCBs holds. Furthermore, even tough rotations of the grains contained by or on the CCB may or may not produce macroscopic strain [38, 13], as discussed in the following sections, these effects are, in fact, taken into account by expression (2.8).

Remark 1.

Finally, it is also worth mentioning that the novelty of expression (2.8), which has been derived for first time here, relies on the fact that this expression allows us to

compute directly the *average small strains rate tensor* of a given packing of two-dimensional granular materials without the need of further calculations or derivations. This, in contrast to other previously obtained expression such as the ones introduced by Bagi [10, 8] or Wellmann [91], which were derived to compute the *average small strains tensor*, instead. Thus, in order to compute the corresponding average small strains rate tensor out of the aforementioned expressions, further mathematical derivations and coding is needed. Here, we have used a similar procedure as the one followed by [91], but applying additional assumptions as well as constraints such as the use of closed-connected-boundaries (CCBs). These assumptions and constraints are needed due to the fact that, here, we have derived an expression for the average small strains rate tensor instead of an expression for the average small strains tensor as in the case of cited authors.

Non-associative Mohr-Coulomb and dilation angle

As mentioned previously in this section, dilation is an important phenomenon usually considered in constitutive modeling of granular materials. Hence, the Mohr-Coulomb failure criterion described in subsection 2.2 has to be modified to take into account the effects of dilation in the material's behavior and response to loading. Thus, the mentioned modification is known as the *non-associative Mohr-Coulomb* [14] failure criterion, and is mainly characterized by the plastic strain rate $\dot{\varepsilon}^p$ not being orthogonal to the yield surface of the classical Mohr-Coulomb failure criterion $\tau_{\max} = \sigma \tan(\Phi) + c$ (red line in Figure 2.8, $c = 0$) , but to a different surface, $\tau_{\max} = \sigma \tan(\psi) + c_1$ (blue line in Figure 2.8, $c_1 > 0$), which depends on the dilation angle ψ that, at the same time is a function of the plastic strain rate $\dot{\varepsilon}^p$ as defined by Figure 4.3

Then, the dilation angle ψ can be easily computed using the definition illustrated by Figure 4.3, which basically defines it as the degree of "misalignment" of the plastic strain rate Mohr-Circle with respect to the origin of the cartesian space $\dot{\epsilon}^p - \dot{\epsilon}^p_{12}$, where $\dot{\epsilon}^p$ and $\dot{\epsilon}^p_{12}$ are the volumetric and deviatoric strain rates, respectively.

Moreover, from Figure 4.3, and assuming that the elastic part of the strain rate $\dot{\varepsilon}^e$ is much smaller than the plastic part of the strain rate $\dot{\varepsilon}^p$, we obtain the following expression

$$\sin(\psi) \approx \frac{\dot{\varepsilon}_1 + \dot{\varepsilon}_2}{\dot{\varepsilon}_1 - \dot{\varepsilon}_2} \tag{2.9}$$

Then, applying the local frame of reference shown by Figure 4.2(b) to equation

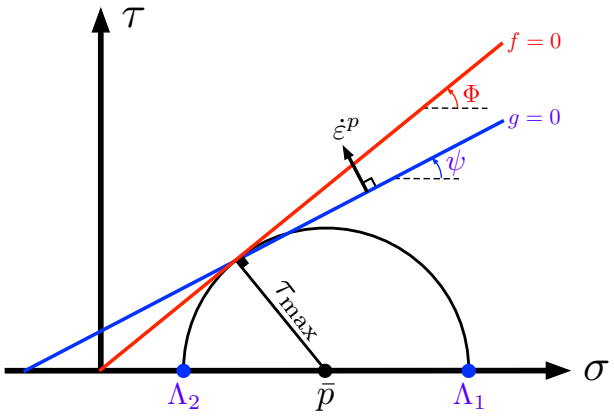

Figure 2.8: Non-associative Mohr-Coulomb model: yield function $f = 0$ and plastic potential $g = 0$.

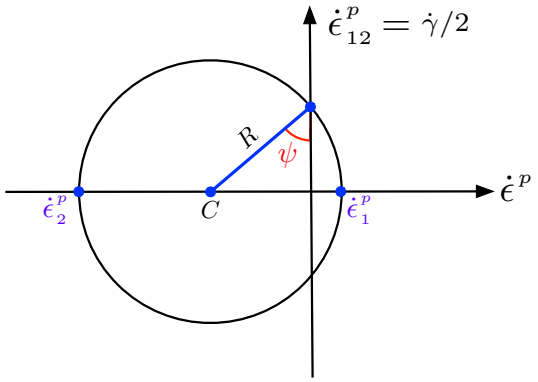

Figure 2.9: Plastic strain rate Mohr's circle and dilation angle definition.

(2.8) and combining it with expression (2.9), we arrive to

$$\sin(\psi) \approx \frac{\sum_{\alpha=1}^{Nc^{CCB}} |\boldsymbol{d}^\alpha|(\dot{u}_t^\alpha - \dot{\delta}^\alpha u_r^\alpha)}{\sqrt{\left\{\sum_{\alpha=1}^{Nc^{CCB}} |\boldsymbol{d}^\alpha| \left\{\dot{u}_r^\alpha \sin(2\delta^\alpha) - \dot{u}_t^\alpha \cos(2\delta^\alpha) + \dot{\delta}^\alpha \left[u_r^\alpha \cos(2\delta^\alpha) + u_t^\alpha \sin(2\delta^\alpha)\right]\right\}\right\}^2 + \left\{\sum_{\alpha=1}^{Nc^{CCB}} |\boldsymbol{d}^\alpha| \left\{\dot{u}_r^\alpha \cos(2\delta^\alpha) + \dot{u}_t^\alpha \sin(2\delta^\alpha) - \dot{\delta}^\alpha \left[u_r^\alpha \sin(2\delta^\alpha) - u_t^\alpha \cos(2\delta^\alpha)\right]\right\}\right\}^2}} \tag{2.10}$$

which defines a fundamental macro constitutive parameter as the dilation angle ψ in

terms of micro-kinematical quantities as fabric, contact displacements and contact velocities in the CBB (see Figure 2.7) of an array of confined particles undergoing loading. Furthermore, note that the numerator in the right-hand-side of equation (2.10) contains only tangent components of the contact velocities in the CBB, suggesting that *the changes in volume in a confined granular material subjected to loading conditions are mainly due to changes in the local tangent components of the velocities at the contact points*, which at the same time lead to different mechanisms such as sliding, rotation, and rolling as studied and described in the following subsections (see Figure 2.13).

Moreover, note that equation (2.10) can be used to study sub-domains inside a given sample, and, therefore, it can be applied to the study of relations between micro, meso, and macro scales. However, in the present work we do not exploit the full potential of the aforementioned expression in the sense of the mesoscale, leaving it for future works.

Example

For this numerical test, we have a two dimensional sample made of 2314 discs with a regular boundary belt (876 discs of radius $r = 0.25$ units, distributed into 4 layers, and with orientation $\delta = 60°$ with respect to the horizontal axis), as shown by Figure 2.10. The boundary belt has been included to facilitate the CCB calculation (see Figure 2.7), which is still a mathematical issue and a currently active area of research in its field (see, for instance, [64]), and has been calibrated so the overall behavior of the polydisperse core is barely affected. Even tough the boundary belt is not necessary for this example (we could have applied a convex hull instead by slightly modifying expression (2.8) and its corresponding related definitions), it is very important for some assumptions and derivations made in the remaining part of this work as well as for Example 2.3.

Inside the boundary belt there are 1438 discs with an average radius of 0.3 units, and 66.74% of polydispersity. The sample departs from a hydrostatic state of stress of 100 units of pressure and, then, undergoes quasi-static axial loading along the vertical axis while keeping the horizontal stress constant. For this test, we use an implicit DEM algorithm [35], where: $k_r = k_t = 7.5E^4$ (units of force per unit of length) are the effective normal and tangent stiffness, respectively, $\dot{u}_2 = 7.5E^{-5}$ (units of length per unit of time) is the vertical loading velocity at the upper wall, and $\theta = 1$ is a numerical integration parameter and restitution coefficient (backward

Euler and perfectly inelastic collision).

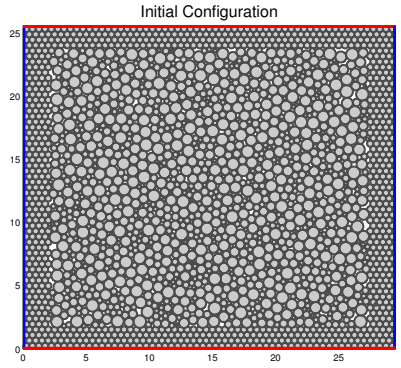

Figure 2.10: Polydisperse sample of 2314 discs with a 4-layers-regular-boundary belt (876 discs of radius $r = 0.25$u, orientation $\delta = 60°$). The discs are confined by a rectangular container ($\sim 29.5 \times 25.62$ square units) with quasi-frictionless walls ($\mu_w = 1E^{-6}$), which, at the same time is subjected to quasi-static axial loading along the vertical axis. The sample departs from an initially hydrostatic loading state of 100 units of pressure.

The main objective of this example is to verify the accuracy and effectiveness of expression (2.10) by comparing the results herein obtained with well known physical trends and models. Thus, we first check on the maximum dilation angles compared to peak and residual strengths for different values of the inter-particle friction coefficient μ, as shown by Figure 2.11.

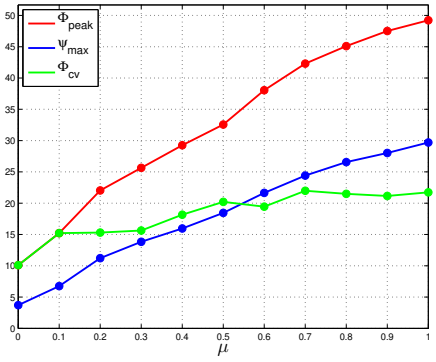

Figure 2.11: For the sample in Figure 2.10. Peak friction angle (red line), maximum dilation angle (blue line), and residual friction (green line), versus inter-particle friction coefficient μ.

The trends shown by Figure 2.11 (peak strength, maximum dilation, and residual strength) are well studied and similar figures can be found, for instance, in [66]. Note that Figure 2.11 shows that the sample of Figure 2.10 also follows the typical independence on the inter-particle friction coefficient μ for high enough values of it, i.e., $\mu \geq 0.4$ in this case.

Finally, we check on the trends and relation between friction and dilation, which have also been well modeled and documented for two and three-dimensional cases (see, for instance, [30, 29]). Here we focus our attention on two specific cases, $\mu = 0.3$ and $\mu = 0.7$ [69], where, in the first case, the residual strength is independent of the inter particle friction, while in the second it is. The values have been chosen so the sample fully behaves without bias due to μ being too low or too high. Corresponding curves for the evolution of the internal friction and dilation angles in terms of the equivalent strain ϵ_s are shown by Figure 2.12.

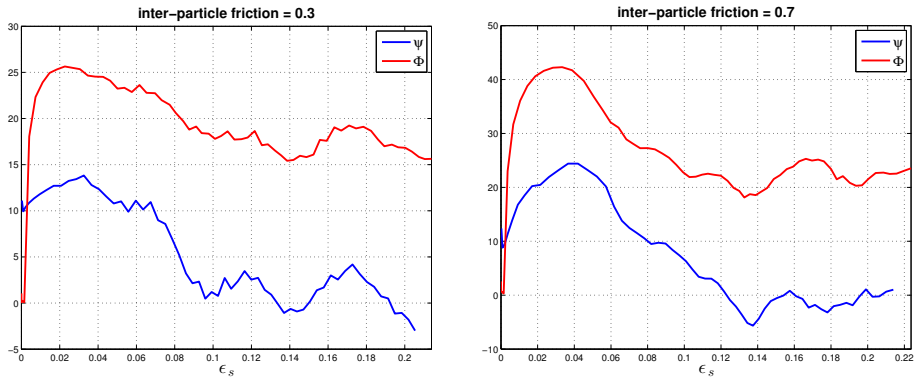

Figure 2.12: For the sample in Figure 2.10. Left: Graph of the evolution of the mobilized friction angle, Φ, and the dilation angle, ψ (computed from equation (2.10)) for an inter-particle friction coefficient $\mu = 0.3$, versus axial equivalent strain ϵ_s. Rigth: Graph of the evolution of the mobilized friction angle, Φ, and the dilation angle, ψ (computed from equation (2.10)) for an inter-particle friction coefficient $\mu = 0.7$, versus axial equivalent strain ϵ_s.

Now, we are able to validate the results shown in Figure 2.12 with respect to three well known models connecting residual strength, maximum dilatation and peak friction for plane strain, i.e., sawtooth [30], Taylor [83], and Bolton [12] as shown in the Table 3.2.

From Table 3.2, we therefore, conclude that, as in [30], Bolton's model is the most accurate, being, on the other hand, the Sawtooth model the least accurate in this

μ	Φ_{peak}	Φ_{cv}	ψ_{max}	Model	Expression	Error
0.3	25.64	15.63	13.83	Sawtooth	$\Phi_{peak} = \psi_{max} + \Phi_{cv}$	14.9%
				Taylor	$\tan\left(\Phi_{peak}\right) = \tan\left(\psi_{max}\right) + \tan\left(\Phi_{cv}\right)$	9.67%
						9.58%
0.7	42.3	21.98	24.41			5.77%
				Bolton	$\Phi_{peak} = 0.8\,\psi_{max} + \Phi_{cv}$	4.11%
						1.87%

Table 2.1: Validation of the results shown in Figure 2.12 using the Sawtooth, Taylor, and Bolton models for plane strain.

case overshooting the actual value for peak strength. Hence, we have validated expression (2.8) qualitatively and quantitatively. This provides a strong basis for the assumptions and derivations regarding critical state kinematics and residual strength independence on the inter-particle friction coefficient, and which are carried out in the subsequent subjections of this article. Further validation and analysis of this array's mechanical behavior and derived expressions will be given in Example 2.3.

Critical state

After verifying in Example 2.3 the accuracy and validity of expression (2.10) to compute the dilation angle ψ in terms of micro-kinematical quantities as fabric, contact displacements and contact velocities in the CBB (see Figure 2.7) of an assembly of confined particles undergoing loading conditions, we are able to use this expression to study from the micro-kinematical point of view an important phenomenon related to dilation such as *critical state* [70, 81, 92] where the volume of a confined assembly of particles undergoing loading does not change in time. This, then enables us to dig deeper into the micro-mechanisms behind residual strength Φ_{cv}, see Example 2.3, that is recalled as the strength at critical state, which, at the same time, remains constant as the loading process evolves into the critical state regime. Thus, when a given array of particles goes into critical state, and from equation (2.10) , note that

$$\dot{\varepsilon}_v = 0 \quad \Rightarrow \quad \boxed{\sum_{\alpha=1}^{Nc^{CCB}} |\boldsymbol{d}^{\alpha}|(\dot{u}_t^{\alpha} - \dot{\delta}^{\alpha} u_r^{\alpha}) = 0} \tag{2.11}$$

and since $|\boldsymbol{d}^{\alpha}| > 0$, we assume a stronger form of the micro-mechanical condition (2.11) for critical state, i.e., $\boxed{\dot{u}_t^{\alpha} = \dot{\delta}^{\alpha} u_r^{\alpha}}$. Moreover, note that, by definition

$$\dot{u}_t^{\alpha} = \underbrace{\dot{u}_1^{\alpha} \sin(\delta^{\alpha}) - \dot{u}_2^{\alpha} \cos(\delta^{\alpha})}_{\text{translation } \left(\dot{u}_{tT}^{\alpha}\right)} + \underbrace{\dot{\delta}^{\alpha} u_r^{\alpha}}_{\text{rotation } \left(\dot{u}_{tR}^{\alpha}\right)}$$

so, applying this last definition to the stronger form of the micro-mechanical condition for critical state (2.11), we have that

$$\boxed{\dot{u}_{tT}^{\alpha} = 0} \qquad @ \text{ critical state} \tag{2.12}$$

where, $\dot{u}_{tR}^{\alpha}$ and $\dot{u}_{tT}^{\alpha}$ are the rotational and translational parts of the local tangent component of the velocity $\dot{u}_t^{\alpha}$ at the α-th contact point in the BCC. Thus, conditions (2.12) imply that at critical state *rotational mechanism furnish most of the grain-scale kinematics* as proposed, for instance, in [20, 2], and observed experimentally by authors such as [51, 19].

On the other hand, these rotational mechanisms can be produced in different ways by sub-mechanisms acting at the contact level, namely, sliding, rotation or rolling of the particles as depicted by Figure 2.13. Hence, we also use the mentioned sub-mechanisms to study and infer into the micro-mechanics of *residual strength* and its independence on the value of the inter-particle friction coefficient, when this is high enough, as a phenomenon parallel and related to critical state of granular materials.

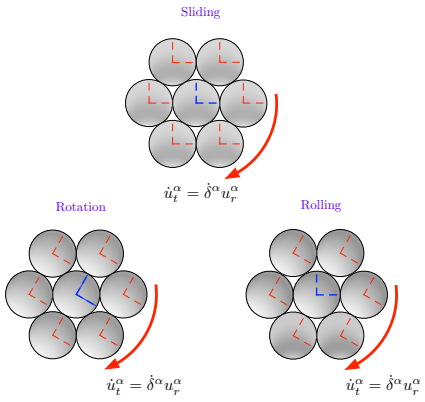

Figure 2.13: The three fundamental mechanism of vorticity in granular materials: sliding, rotation, and rolling

Thus, we close this subsection by introducing an analytical proof of the aforementioned independence of the vortex-like mechanisms on the inter-particle friction coefficient μ when its value is high enough, and on the sensibility of residual

strength for low values of μ [66]. Hence, by parallelism, the sensitiveness and independence of the residual strength Φ_{cv} on low and high enough values of μ is, therefore, proven. Although the proof herein offered is valid for packings made of two-dimensional cohesionless discs with random sizes (polydisperse), there is no loss of generality and, therefore, can be assumed for more general cases.

We begin by considering Coulomb's friction law $|f_t^\alpha| \leq \mu f_r^\alpha$, where f_r^α is taken as positive and can be obtained by assuming Hooke's law $f_r^\alpha = k\Delta r^\alpha$, where by definition, $\Delta r^\alpha := |\boldsymbol{d}^\alpha|_0 - |\boldsymbol{d}^\alpha| = X_r^{q,\alpha} - X_r^{p,\alpha} - (x_r^{q,\alpha} - x_r^{p,\alpha})$, so we can write the displacement of the α-th contact point in the CCB u_r^α in terms of Δ_r^α, and after some manipulation we arrive to the following inequality

$$\boxed{u_r^\alpha \leq -\frac{1}{\mu k}\left(\sum_{\beta=0}^{\alpha-1}|f_t^\beta| + \frac{1}{2}|f_t^\alpha|\right)} \tag{2.13}$$

where $\left|f_t^0\right|$ corresponds to Δr^0 which, at the same time, is the normal stretch of an arbitrary branch vector in the CCB where it can be known or imposed. Hence, condition (2.12) and inequality (2.13) enable us to go into a deeper analysis about the role played by the inter-particle friction coefficient μ on residual strength, proving us with a powerful tool to study each of the rotational sub-mechanisms described in subsection 2.3 (sliding, rotation, and rolling) and illustrated by Figure 2.13 in relation to μ. See Appendix A for details and complete proof.

Example

This example is a continuation of Example 2.3, all the results and data shown here are taken from the same simulation performed for the mentioned example. In this case, *the objective is to carry out some numerical verification of expression (2.12), and to show additional numerical evidence on the analytical proof about the independence of the residual strength on the inter-particle friction coefficient (at critical state) given in the last part of subsection 2.3*.

First, we look at expression (2.12). With this aim, we have plotted the evolution of $\sum_{\alpha=1}^{Nc^{CCB}} |\boldsymbol{d}^\alpha|\, \dot{u}_t^\alpha$ (blue line) and $\sum_{\alpha=1}^{Nc^{CCB}} |\boldsymbol{d}^\alpha|\, \dot{\delta}^\alpha u_r^\alpha$ (red line) with respect to the equivalent strain ϵ_s for inter-particle friction coefficients of $\mu = 0.1$, 0.5 and 0.9 (from left to right, respectively) as shown by the third row of Figure 2.14. Hence, and using the vertical green line that marks the onset of critical state for all the plots, it can be seen that at the mentioned point and thereafter $\sum_{\alpha=1}^{Nc^{CCB}} |\boldsymbol{d}^\alpha|\, \dot{u}_t^\alpha$ converges to $\sum_{\alpha=1}^{Nc^{CCB}} |\boldsymbol{d}^\alpha|\, \dot{\delta}^\alpha u_r^\alpha$, which at the same time implies that $\dot{u}_t^\alpha \longrightarrow \dot{u}_{t_R}^\alpha$ in agreement

with expression (2.12). This in mechanical terms means that all the tangent velocities at the contact points on the CCB are being generated by angular rotations of the corresponding brach vectors.

Thus, the physical phenomenon described in the last paragraph and illustrated by the third row in Figure 2.14, also implies the development of high vorticity or granulance inside the array, as shown by Figure 2.15, which in fact, has been experimentally found to be a dominant mechanism at critical state in two-dimensional arrays [51, 19].

Second, we use the fourth row in Figure 2.14 , where the evolution of the percentage of sliding contact points inside the whole array in terms of the equivalent strain ϵ_s for values of the inter particle friction coefficient $\mu = 0.1$, 0.5, and 0.9 (from left to right, respectively) is plotted to help us extract meaningful physics out of the analytical proof about the independence of the residual strength on the inter-particle friction coefficient (at critical state) given in subsection 2.3. Thus, note from the aforementioned row in Figure 2.14 and from the vertical green line that once critical state kicks in the total number of sliding contact points has reached a pretty well stablished steady state (constant value), which at the same time is the minimum percentage of sliding contact points along the loading process (it also implies that the number of contact points rotating or rolling, see also Figure 2.13, becomes maximum and constant), i.e., at this point and thereafter dissipation is minimum and the flow of contacts going into or leaving sliding mode either remains unchanged or vanishes.

Furthermore, Note that for $\mu = 0.1$ the steady state percentage of sliding contacts is around 22%, while for $\mu = 0.5$ and $\mu = 0.9$ the steady state goes around 4% and 2%. Hence, we conclude (and from additional data for other values of μ) that when the percentage of sliding contact points at steady state goes below 10%, then the corresponding residual strength becomes independent on the inter-particle friction coefficient. This is consistent with the last part of the proof given in Appendix A, where the case in which $\mu \to 0$ is analyzed and a sensitiveness to small values of μ is shown. Hence, this "sensitiveness" is explained from the relatively high percentage of sliding contact points at steady state (around 22% for $\mu = 0.1$) for small enough values of μ, implying a very logical and expected conclusion: *the lower the value of μ the more contact points are sliding*, and therefore *the more dependent on μ becomes the assembly* provided Coulomb's friction law holds, but "paradoxically" μ's value is very close to be null. On the other hand, a low percentage of

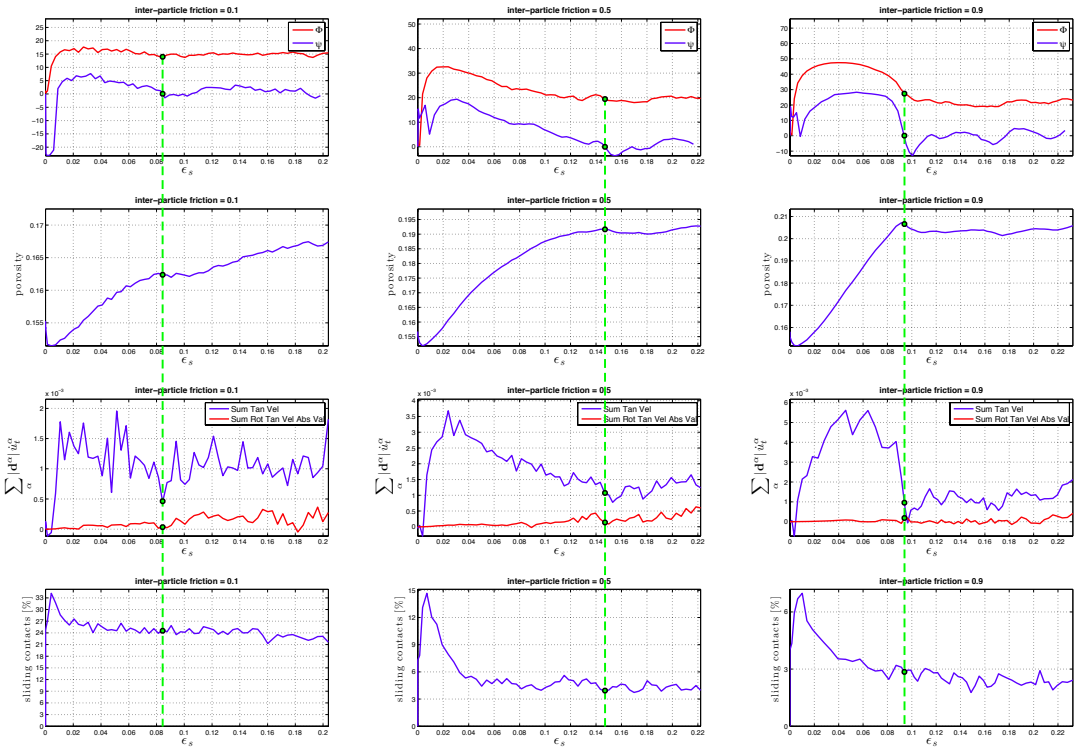

Figure 2.14: For the sample shown by Figure 2.10, for each column (inter-particle friction coefficient $\mu = 0.1$, 0.5, and 0.9), and from top to bottom: friction Φ and dilation ψ (computed from equation (2.10))) angles, porosity, convergence of the critical state micro-mechanical criterion (2.12), percentage of contact points sliding, versus equivalent strain ϵ_s.

contact points at critical state also implies that the two governing micro-mechanical mechanisms are rotation and rolling, which explains the high vorticity as shown by Figure 2.15. Moreover, a similar phenomenon has been also observed in granular systems without friction, or systems with blocked rotations. However, it is worth mentioning that these kinds of systems are unrealistic and usually used as artifacts to qualitatively match the behavior of real angular or "lubricated" materials by simulating them with simpler shapes such as discs or spheres. Furthermore, as mentioned before, the independence of a granular packing on the inter-particle friction coefficient μ has been previously shown [66].

Thus, the analysis introduced in the last paragraph has been simplified and summarized in Table 2.2 for a better and more comprehensive interpretation of the work herein developed.

Independence on:	Inter-particle friction, μ
Main mechanisms:	Rotation and Rolling (Figure 2.13)
Particular Cases:	• *Systems Without Friction*: Grains do not roll nor slide but rotate individually • *Blocked Particle Rotations*: Grains do not roll nor slide but rotate in clusters

Table 2.2: Mechanisms governing critical state vorticity.

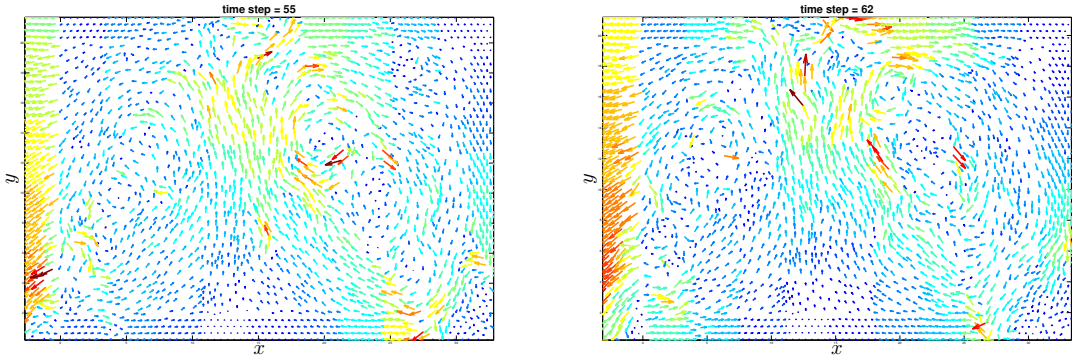

Figure 2.15: Fluctuating part $\dot{\boldsymbol{u}}'^{p}$ of the particles velocity field obtained by Reynolds decomposition with space averaging [24] in each direction during critical state regime for an inter-particle friction coefficient $\mu = 0.6$, and where the arrow color is graded by magnitudes of fluctuation velocity. Left: At time step = 55, with corresponding equivalent strain $\epsilon_s = 0.1826$. Right : At time step = 62, with corresponding equivalent strain $\epsilon_s = 0.2096$.

Finally, we also use the fourth row in Figure 2.14 to shed more light on the last of the micro-mechanical conditions (2.5) for peak strength and its corresponding numerical result shown by Figure 2.5 (Right). Thus, note from the first and fourth rows in Figure 2.14 that even tough the maximum percentage of sliding contact points is not precisely reached at peak friction angle, it is reached very close to it, so at peak strength a very high percentage (close to the maximum percentage) of contacts are, in fact, sliding in agreement with the last of the micro-mechanical conditions (2.5) for peak strength and Figure 2.5 (Right), which imply and show, very high dissipation at peak strength.

2.4 Closure

We have presented an analytical procedure to study continuum-scale phenomenology in two - dimensional non-cohesive granular materials from the grain-scale point of view, and which uses a stress invariant-based constitutive model such as the non-associative Mohr-Coulomb criterion, from where, two key phenomenological

states, i.e., material peak strength (friction angle) and critical state (dilation angle) were directly related to forces, kinematics, and fabric at the grain level. Regarding peak strength, this procedure enabled us to infer two necessary and sufficient conditions that can be applied to both: continuum and grain scale levels, and which give us a deeper insight on the underlying frictional micro-mechanisms furnishing macroscopic peak behavior as well as related buckling phenomenon. Moreover, for critical state, this procedure helped us to analytically unravel the dominant micro-kinematical mechanisms driving the macroscopic behavior, which, at the same time, led us to an analytical proof of the independence and sensitiveness of the residual strength on high and low values of the inter-particle friction coefficient, respectively. Finally, this framework was validated through three numerical tests, which were also used to illustrate the potential of the framework in helping us analyze and understand macroscopic properties and phenomenon starting at the grain level.

Chapter 3

EFFECTS OF GRAIN MORPHOLOGY ON CRITICAL STATE: A COMPUTATIONAL ANALYSIS

Published on: *Acta Geotechnica* [33].

3.1 Introduction

The role played by grain morphology in the strength and physical behavior of a given granular material subjected to confinement has been broadly and intuitively accepted throughout the history of soil and geomechanics. However, even though some works [73, 54, 53, 77, 17, 49] have already looked into the connections between these two apparently different features of the same material, there are still important relationships to be unraveled. Furthermore, due to the complex morphological characteristics of real grains, this subject has been mostly studied from the experimental setting, which does not always count with the necessary tools and technology to properly measure fundamental phenomena, and, when effective, a good amount of time and resources need to be expended in designing, setting up, and running a given experiment. This has always represented a major issue that has given rise to the use of emergent techniques such as computational simulation through mathematical models and numerical methods that, once validated and calibrated, can mimic the real experiment, allowing for the study of the same phenomena in a faster, less expensive and safer way. Since the late 1970s, a series of explicit and implicit numerical models called discrete element methods (DEM) [23] has been widely used to understand the grain-to-grain interactions and their connections with the material's macroscopic behavior. However, these numerical techniques face several limitations related in particular to capturing the shapes and textures of real grains. Many models and assumptions ranging from spherical and polyhedral grain shapes [26, 1] to rotational constraints of the grains [60] have been implemented and used to account for and mimic the effects produced by real particle shapes in granular processes. With the advent of new computational techniques together with a increase in processing capabilities, discrete element methods have also incorporated more sophisticated techniques such as particle clustering [27, 7] that have allowed for better and more accurate approaches of reality in terms of particle shapes. However, none of these techniques have thoroughly succeeded in

mimicking and, therefore, in studying the effects of particle morphology as well as quantifying the amount of detail needed when mimicking a real grain to actually obtain a similar quantitative and qualitative mechanical behavior to the one displayed by the real material. The combination of new experimental techniques such as x-ray computed tomography (XRCT) [42] and mathematical representation of real shapes through the use of NURBS [4, 44], has proven very effective but computationally costly, so further efforts have continued in order to gain computational efficiency with these new technologies.

The objective of this work is, as shown by Figure 4.1, to take advantage of a new DEM scheme applied for first time here to study the connections between real grain morphology, i.e., sphericity and roundness, and critical state (CS) parameters such as critical state line slope λ and intercept Γ, and critical state friction angle Φ_{cs}. We have chosen sphericity and roundness as the morphological parameters to be used in this study due to their widespread use within the fields of geotechnics, geomechanics and soil mechanics. Sphericity has several different definitions, but the one used in this work is

$$S = \frac{r_{in,max}}{r_{cir,min}} \tag{3.1}$$

where $r_{in,max}$ is the maximum inscribable radius and $r_{cir,min}$ is the minimum circumscribable radius of a given particle. Roundness is defined as

$$R = \frac{\sum_{1}^{N} \frac{r_i}{N}}{r_{cir,min}} \tag{3.2}$$

where r_i is the radius of curvature at the ith corner and N is the total number of corners. Classical works such as [77, 17, 86, 36, 68, 37, 11] have already used the aforementioned parameters (using the same definitions) to study the connections between particle morphology and constitutive behavior. Thus, the ultimate goal is to *quantify and qualify the dependency of the CS parameters on each morphological feature*. Furthermore, part of the aforementioned goal is to answer a fundamental question: *how much detail does an avatar model actually need to account for in order to faithfully reproduce the mechanical response of its real counterpart?* Hence, we begin the present work by introducing the fundamentals of the new level set discrete element method (LS-DEM) [34], that enables the digitalization and DEM simulation of real grain shapes. Then, LS-DEM is used to generate a digital version (avatar) of a two-dimensional real experiment [51], that allows us to validate the method and calibrate its parameters. It is worth mentioning that in the validation

process we have been able to match the experimental results not only qualitatively but also quantitatively as depicted by Figure 3.5. Finally, some additional observations and remarks about the experiment are also included.

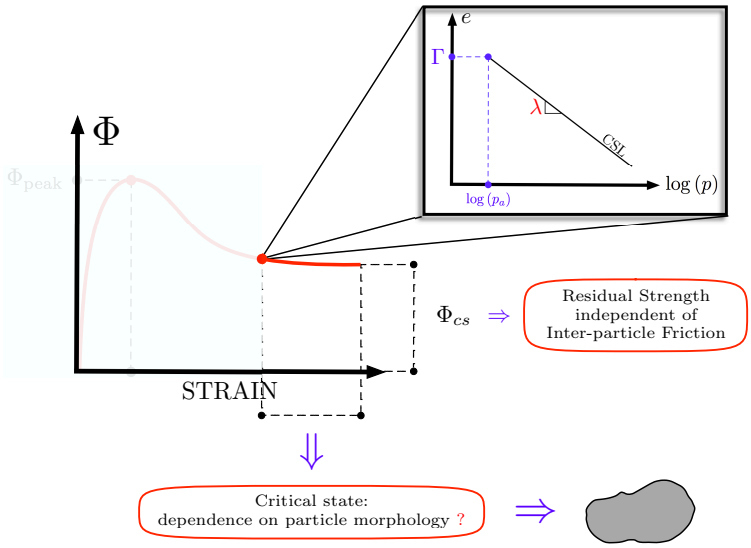

Figure 3.1: Critical state parameters such as CSL slope λ, CSL intercept Γ, and CS friction angle Φ_{cs}, do not depend on the inter-particle friction coefficient. However, it has been experimentally shown [17] that these parameters depend heavily on the particle's morphology via sphericity and roundness. For this study, the CSL slope λ and intercept Γ were obtained by taking each sample (for each type of particle) into critical state (as described in Section 4.4) for different values of the applied normal pressure, i.e., 8.7, 21.7, 43.5, 87.0, 174 348 and 696 kPa. Then, a graph $\log_{10}(p)$ v.s. e (void ratio) is obtained and the critical state line is approximated by a least squares fitting. Finally, the CSL intercept Γ is computed for all the particle shapes at a reference pressure of 1.78 Pa (close enough to the e-axis).

Once LS-DEM has been calibrated, we use it to capture the shape of twenty different two-dimensional cross sections of real grains [17], which have been previously classified according to their morphological features. Then, for each of these real grain shapes, we run simulations using the same experimental set up and boundary conditions as the calibration process, and from where the values of the three critical state parameters (CSPs) previously mentioned are computed. With these results, our investigation focuses on the characterization of each CSP in terms of grain sphericity and roundness as well as in terms of the grain's regularity. Then, we add geometrical idealizations/simplifications that are morphologically equivalent to each of the five real original shapes. These "idealized" grains allows us to isolate and study the effect of the "imperfections" of real shapes on the values of the

CSP, thus, helping us to have a better understanding of how much detail, in terms of shape, may be needed to obtain a good enough approximation to the actual value of each of the CSP. While the term "good enough" is specific to each application or use of the CSP, having a basic idea about the sensitivity of each type of particle to idealization may contribute to a deeper understanding of the impact that detail and shape have on the macroscopic behavior of a granular array.

Hence, the key contribution of the work presented here is the application of a new numerical tool (LS-DEM) to the study of the connections between grain-scale features such as sphericity and roundness that, so far, have been exclusive to the realm of experimental granular mechanics, and macro-scale parameters such as those characterizing critical state. This opens a new avenue for numerical simulation and analysis of the behavior of real and complex granular materials, with potentially countless applications, uses and capabilities.

Finally, the main observations and remarks have been summarized in a table (see, Table 3.2), which is attempted as a consulting tool for basic knowledge on when to simplify a particle's shape in order to obtain a rough, but still good, approximation to the actual value of a given CS parameter.

3.2 Level Set Discrete Element Method

The Level Set Discrete Element Method (LS-DEM) [34] is a variant of the discrete element method [23] that is able to account for particle shape using level sets as a basis for geometric representation. Level sets are versatile in that they are able to capture both smooth edges, such as those found in discs and disc clumping representations, as well as sharp corners, such as those found in polygonal representations. Furthermore, contact algorithms involving level sets are inexpensive. Finally, the use of level sets in the characterization of X-Ray Computed Tomographic images of granular assemblies [85] allows seamless transition from characterization to simulation.

Level Set Description

A level set is a scalar-valued implicit function $\phi(\boldsymbol{x})$ whose value is the signed distance from a point $\boldsymbol{x}$ to an interface [63]. In the context of LS-DEM, the aforementioned interface is the particle's surface, and consequently, $\phi(\boldsymbol{x})$ is unique for a given particle shape.

Values of level set functions are stored at discrete grid points, and values between

grid points are found via interpolation of stored values at surrounding grid points. As such, a level set is able to define the surface of a particle (Figure 3.2), albeit in a much different manner than other particle representations such as polygons or clumping. Level set functions can either be constructed via analytic formulations of geometric shapes or through the image-based method described in [85], both of which are utilized in this work to generate the idealized and real shapes, respectively.

Boundary Node Discretization

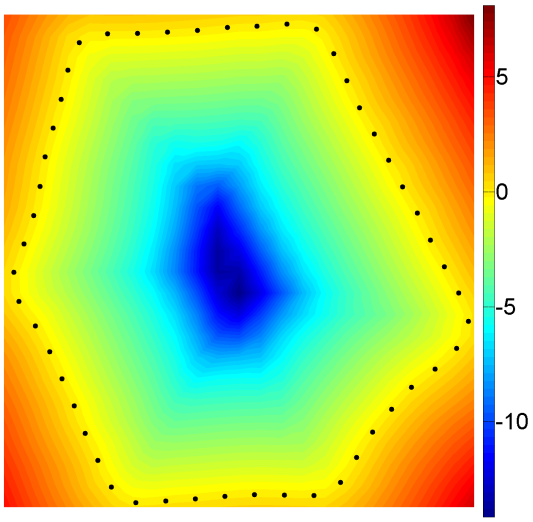

Figure 3.2: Particle representation. The value of the level set function is indicated by color, and boundary node discretization points are plotted in black.

LS-DEM uses a node-to-surface contact algorithm that is utilized in finite element models [41] as well as discrete element models [4] for the handling of nonconvex particles with multiple contact points as well as computational ease, whereby nodes are seeded onto the surface of each particle. The density of nodes on a given particle is a matter of choice and has implications on particle behavior; however, we find that seeding with a maximum node-to-node spacing of less than $d/10$, where d is the particle diameter, is adequate to capture particle morphology as higher nodal densities have a negligible impact on behavior. Contact is then determined by checking each node of a master particle against the boundary of a slave particle for penetration.

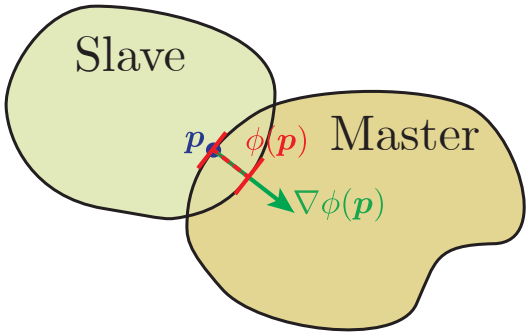

Figure 3.3: Illustration of intersecting particles. Point $\boldsymbol{p}$ of the master particle, seeded from boundary node discretization, is penetrating the slave particle, with penetration distance $\phi(\boldsymbol{p})$ and contact normal $\nabla\phi(\boldsymbol{p})$. Overlap is exaggerated for clarity.

Level Set Contact Algorithm

The contact algorithm is the closest point projection (CPP) of all master nodes onto a slave level set. Given a master node at point $\boldsymbol{p}$ and slave particle represented by the level set $\phi(\boldsymbol{x})$, the penetration distance $g(\boldsymbol{p})$ and the contact normal $\boldsymbol{\nu}(\boldsymbol{p})$ are found by the CPP algorithm, which is as follows:

1. $g(\boldsymbol{p}) = \phi(\boldsymbol{p})$: the penetration distance is equal to the value of the level set function.

2. $\boldsymbol{\nu}(\boldsymbol{p}) = \nabla\phi(\boldsymbol{p})$: the contact normal is equal to the gradient of the level set function. The level set formulation ensures that the magnitude of the gradient is unity.

Figure 3.3 shows an example of a master node penetrating a slave particle. Due to the level set formulation, $g(\boldsymbol{p})$ and $\boldsymbol{\nu}(\boldsymbol{p})$ are very computationally inexpensive since they can be found from a single bilinear interpolation of grid points of ϕ surrounding $\boldsymbol{p}$. Nodal shear displacements (for frictional purposes) are computed as in [4] once the contact normal $\boldsymbol{\nu}(\boldsymbol{p})$ is found.

Equations of Force and Motion

The equations of force and motion follow directly from the original discrete element method [23] with the only differences being

1. Each particle's nodes are treated independently, where each node contributes

and stores its own normal and frictional forces and moments which are then summed across all contacting nodes for that particle.

2. LS-DEM includes moments from eccentric normal forces [22, 4] which do not exist in the original discrete element method due to particles being discs.

It is important to note that, during motion, $\phi(\boldsymbol{x})$ remains in a reference configuration and that all contacts are calculated by moving nodes of the master particle (in the current configuration) into the reference configuration of the slave's level set, computing contact forces, and moving those forces to the current configuration. This prevents the need to ever update $\phi(\boldsymbol{x})$ which can be quite costly if it lies on a fine grid.

See Appendix B for more details on the technical aspects and theory of LS-DEM.

3.3 Calibration and Validation

The objective of this section is to calibrate the recently developed LS-DEM according to the setup and results obtained by [51] regarding fundamental physical phenomena such as eddies and vortices in dense granular two-dimensional flows made of discs undergoing shear. Using LS-DEM, we first try to reproduce the curves obtained in [51] using the same disc size distribution as in the real experiment, i.e., equal amount of discs with diameters 12, 15, and 20 *mm*, used to prevent crystallization.

The avatar experiment contains 384 discs sheared, as in the original experiment, by a belt-like system (top and bottom layers of red semi-circles with a 6 *mm* radius and a centre-to-centre spacing of 14 *mm*, see lower part of Figure 3.4) while subjected to periodic boundary conditions on the left and right walls. Different shear rates, $\dot{\Gamma}$, between 0.08 to 0.8 s^{-1} are applied with the belts to match those used in [51], which also vary between 0.08 to 0.8 s^{-1}. The cyan curve in Figure 3.5 corresponds to the average of the normalized curves obtained for each shear rate, while the red curve represents the theoretical approach introduced in [51]. Here, we have followed the same procedure as in the experimental counterpart (blue curve in Figure 3.5).

The procedure described in the former paragraphs is repeated several times while tuning material parameters and coefficients needed by the LS-DEM scheme such as global damping and particle's stiffness until matching the experimental results as closely as posible, and as shown by Figure 3.5. The values of the tuned parameters and coefficients are displayed in Table 3.1. Furthermore, note that the particle's

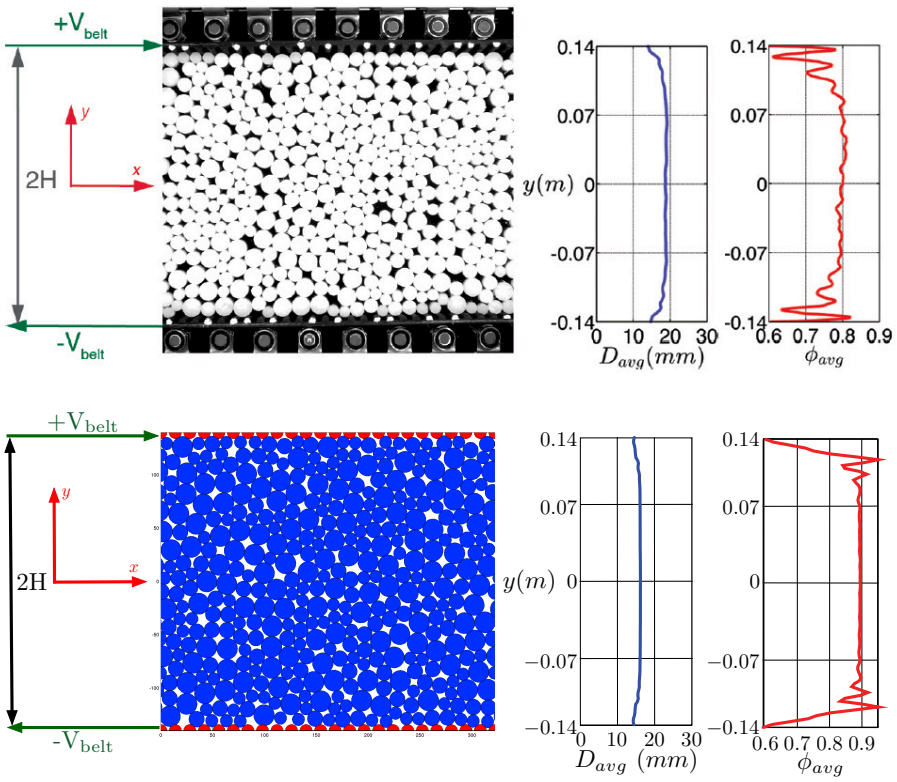

Figure 3.4: Upper Figure: Original experiment (Stadium Shear Device) with plastic cylinders. Time averaged profiles of average particle diameter (blue) and solid fraction (red). Lower Figure: LS-DEM avatar experiment. Time averaged profiles of average particle diameter (blue) and solid fraction (red).

density corresponds to nylon, which is the material used for the discs in the experimental setting. In the same way, inter-particle friction and belt friction correspond to those from nylon and rubber. For particle and belt stiffness, we have calibrated it to give physically reasonable deformations with respect to the applied pressure. This, left global damping as the only parameter that was entirely tuned to match the experimental results.

From the LS-DEM avatar experiment, we observe that the phenomena under study is pressure dependent. Hence, the shapes of the curves of Figure 3.5 could change drastically according to the pressure applied on, or produced by the walls (top and bottom). This pressure dependency of the strain rate $\dot{\gamma}$ is not included as part of the scope of [51] but we think it is worth mentioning so it can be taken into account for future works on the subject.

Our simulations also show that the phenomena under study is global damping de-

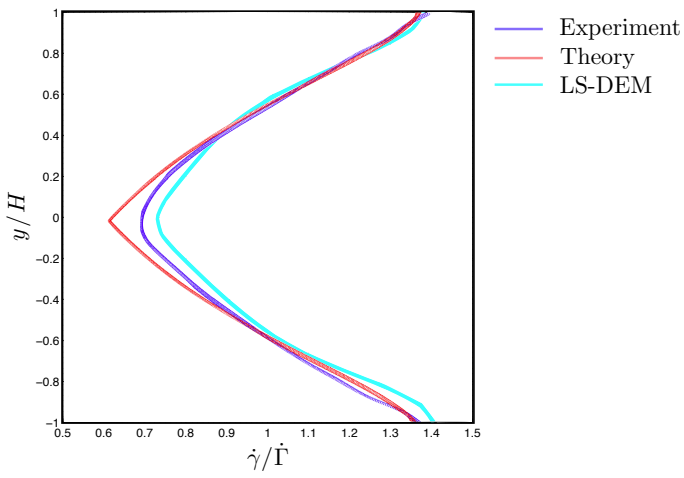

Figure 3.5: Experiment (blue line), theoretical approach (introduced in [51], red line), LS-DEM (cyan line). Averaged normalized shear rate profile.

	value	unit
Particle density	1150	kg/m^2
Particle stiffness	2.6×10^7	N/m
Belt stiffness	2.6×10^6	N/m
Inter-particle friction	0.25	-
Belt friction	0.6	-
Global damping	0.7	$1/s$
Contact damping	0	$1/s$

Table 3.1: Values of the tuned mechanical parameters and coefficients used for the LS-DEM avatar experiment.

pendent (reflected in the experiment as friction between the top and bottom of the cylinders with the glass cover and base). The original work [51] claims that the results were obtained in the absence of base friction; however, our results suggest that the amount of global damping does, indeed, affect the shape of the velocity profile.

On the other hand, and according to Figure 3.4, the average profiles corresponding to the average diameter D_{avg} and solid fraction ϕ_{avg} that were obtained from our simulations do not much their experimental counterparts. We are not sure of how these results were computed or derived by [51]. However, we have carried out simulations for different values of grain stiffness and global damping without being able to match the corresponding experimental results with enough accuracy. Fur-

thermore, from a quick calculation of the average diameter, i.e., $(12mm + 15mm + 20mm)/3 = 15.666mm$ it is clear that the results from our simulations are closer to this "quick average" than the ones computed by [51].

Once the set of parameters and coefficients was calibrated, we were able to obtain very close results to those from the real experiment [51], as can be concluded from Figure 3.5. However, we could not properly match the values for the time average profiles of average particle diameter and solid fraction (see, Figure 3.4), where we obtained lower and higher values, respectively.

Finally, in this section, we have shown that LS-DEM can also be used for classical shapes as discs and spheres and that we can calibrate the method to match real experimental results not only qualitatively but also quantitatively as best as possible.

3.4 Particle Morphology and Morphology Idealization Effects on Critical State Parameters

Once the avatar experiment has been calibrated, we proceed with our main aim of studying the effects played by particle morphology, i.e., how changes in sphericity and roundness (as defined by [17]) affect the macroscopic behavior of a given array of particles. These changes in macroscopic behavior due to the particle's morphology have been broadly and intuitively accepted, but there are only a few works [77, 17] that actually look for comprehensive correlations and physical relationships between these two different scales cohabiting and interacting at the same time as a granular media reacts to external excitations. For our study, we use some of the shapes corresponding to two-dimensional slices of real particles given in [17], and shown in Figure 3.6. Each real shape is located right next to its corresponding morphological "idealization", and according to its roundness and sphericity values (x and y axis).

In particular, we focus our work on critical state parameters such as CSL slope λ, CSL intercept Γ, and CS friction angle Φ_{cs} (see, Figure 4.1), which have already been shown to be independent of the inter-particle friction coefficient [82, 66] (for values of the inter-particle friction coefficient μ greater than 0.1), reason for which we rule out this morphological parameter (that is a measure of smoothness, see [17]) from this study, narrowing our attention to only sphericity S, and roundness R.

As we wonder about the ways in which particle morphology affects macroscopic behavior, an important question raises: *how much detail does an avatar model ac-*

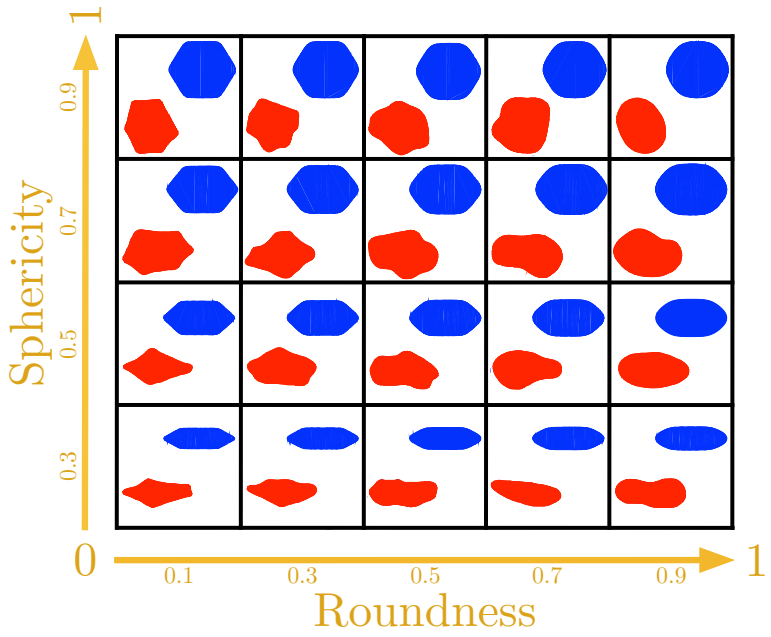

Figure 3.6: Real particles taken from Figure 1 in [17] and corresponding idealized particles used in the present work to study the effects of morphology and idealization on critical state parameters. The particles have been classified according to roundness (x-axis) and sphericity (y-axis).

tually need to account for in order to faithfully reproduce the mechanical response of its real counterpart? While "faithfully" is a relative and broad term that heavily depends on the context, i.e., the type of uses and application as well as the accuracy needed for each one, this is a very relevant question that, once answered, might help to simplify as well as optimize procedures and computational cost for some cases and applications. Hence, in the present study, we have also included "idealized" particles with similar values of sphericity and roundness as the ones computed from their corresponding real counterparts (see, Figure 3.6), which, in turn, will help us to understand how the amount of "detail" given to the avatar affects or modifies the macroscopic response.

Remark 1.

Although it was already mentioned in section 4.1, it is worth emphasizing the reasons that led us to the choice of sphericity and roundness as the parameters to study the effects of grain morphology on critical state was due to their widespread use within the fields of geotechnics, geomechanics, and soil mechanics. Classical works such as [77, 17, 86, 36, 68, 37, 11] have already used roundness and sphericity to

study the connections between grain morphology and constitutive behavior.

Furthermore, it is well known that these parameters provide relevant information regarding the grain and sub-grain scales: sphericity gives information about the morphological features related to the grain's diameter scale $O(d)$, whereas roundness takes into account morphological information coming from a smaller scale $O(d/10)$. This distinction allows us to identify and separate the mechanical effects induced by each of these scales.

Sensitiveness to Idealization and Dependency on Regularity

In this subsection, we analyze the sensitiveness to idealization of each individual CS parameter, i.e., λ, and Γ which has been computed for all the particle shapes at a reference pressure of 1.78 Pa (close enough to the void ratio axis), and Φ_{cs} as well as their individual dependency on the particle's regularity ρ, defined as the average between sphericity and roundness [17]. This analysis may be useful for some applications where only one or a set of CS parameters are needed or more relevant, and the simulation process wants to be optimized. Thus, one may take into account this analysis (or a similar one) to decide on whether or not to use an idealized particle instead of its real equivalent to compute the aforementioned set or subset of parameters.

- λ: In general, real particles seem to be more sensitive to changes in regularity, ρ, than the idealized ones. The difference in the slopes, corresponding to the linear interpolations, gives a ratio real to ideal of 2.55 (see Figure 4.2). The goodness of fitting is also higher for real particles, $R^2 = 0.91$, compared to $R^2 = 0.72$ in the case of idealized particles.. This indicates that the surface $\lambda^{\text{real}}(S, R)$ is smoother and flatter than the surface $\lambda^{\text{ideal}}(S, R)$ as evidenced by Figure 4.5.

- Γ: From Figure 4.3, note that real particles are more sensitive to changes in regularity, ρ, than idealized particles, showing slopes of 18.26° and 5.54°, respectively in the linear fittings. This corresponds to a ratio real to idealized of 3.4. In the same way, the goodness of fitting is also higher for real particles, $R^2 = 0.9$, versus $R^2 = 0.54$ for idealized particles, indicating, once again, a much smoother and flatter surface $\Gamma^{\text{real}}(S, R)$, as confirmed by Figure 4.7.

- Φ_{cs}: Idealized particles are slightly more sensitive to changes in regularity, ρ, than real ones as shown by Figure 4.4. The ratio real to ideal of the slopes of

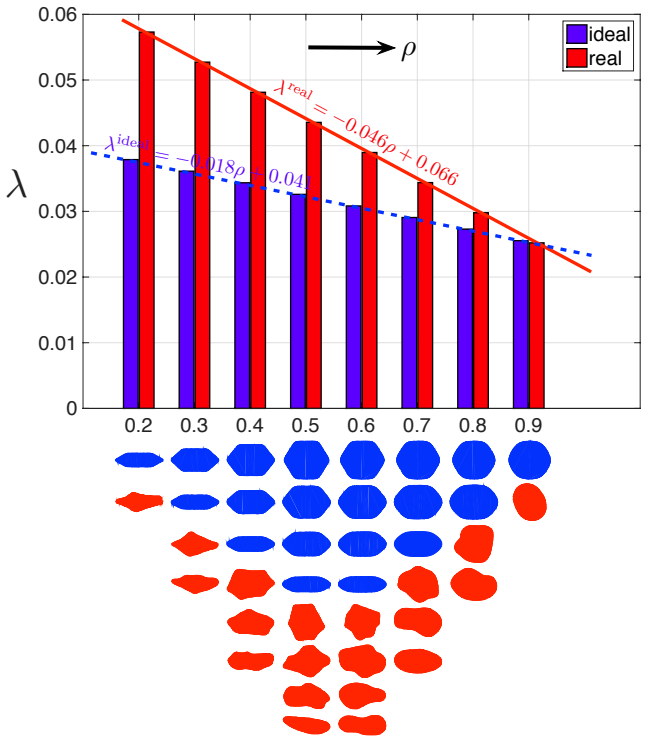

Figure 3.7: Values of the CSL slope, λ, of ideal (blue columns) and real (red columns) particles sorted with respect to particle's regularity, ρ.

the corresponding linear fittings is 0.83, indicating a similar behavior in both cases. Regarding goodness of fitting both types of particles show similar values as well: $R^2 = 0.67$ and $R^2 = 0.52$ for real and idealized particles, respectively. This shows that none of the surfaces $\Phi_{cs}^{real}(S,R)$ and $\Phi_{cs}^{ideal}(S,R)$ are smooth and flat, as can also be inferred from Figure 4.9.

Moreover, it is worth noting that all the CSP under analysis, in general, show higher values for real grains than in the case of their idealized counterparts, as clearly illustrated by Figures 4.2 to 4.4.

Unlike [17], we consider λ highly dependent on regularity, ρ. For instance, in the ideal case, whose slope is 0.018, which, in fact, seems negligible, we observe that λ goes from ≈ 0.038 at $\rho = 0.2$ to ≈ 0.025 at $\rho = 0.9$ (see Figure 4.2). This represents a change of 34.2% in the value of λ. In the same way, the values of Γ in the idealized case go from ≈ 0.43 to ≈ 0.36 for the same values of ρ as in λ (see Figure 4.3). This accounts for a change in the value of Γ of $\approx 16\%$. Φ_{cs} for the idealized particles, and evaluated at the same values of ρ as the in the cases of

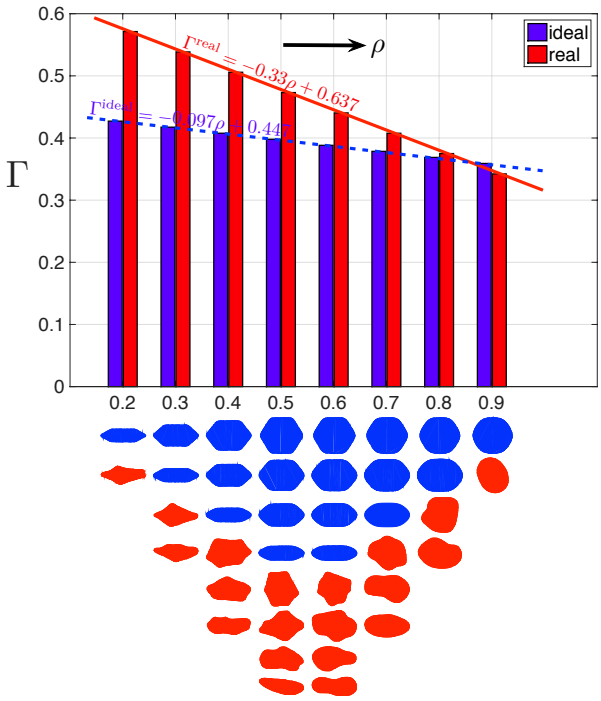

Figure 3.8: Values of the CSL intercept, Γ, of ideal (blue columns) and real (red columns) particles sorted with respect to particle's regularity, ρ.

λ and Γ, goes from $\approx 27°$ to $\approx 16°$, giving a change of $\approx 41\%$ in the values of this parameter (see Figure 4.4). The percentages of changes of λ, Γ and Φ_{cs} for the real case are approximately 57%, 40%, and 35%, respectively. Note that CSP corresponding to the real particles, except for Φ_{cs}, are much more sensitive with respect to ρ (see, Table 3.2), with λ showing the most variability, unlike what is claimed by [17].

This suggests that taking into account the values of the slopes of the linear fittings solely may be misleading in the analysis on how a parameter depends on other, especially in this case, where the nature of each critical state parameter is different, but each parameter is plotted against the same range of values of the same variable, ρ. Finally, from Figures 4.2, 4.3 and 4.4, note that a general trend holds equally for all the parameters independently if they come from real or idealized particles, i.e., *as* ρ *increases* λ, Γ, *and* Φ_{cs} *decrease*, which was also reported in [17].

Dependency on Sphericity and Roundness: Real v.s. Ideal

Plotting the critical state parameters λ, Γ, and Φ_{cs} in terms of regularity, ρ, makes the plots simpler and easier to read. However, by doing so, a good amount of detail

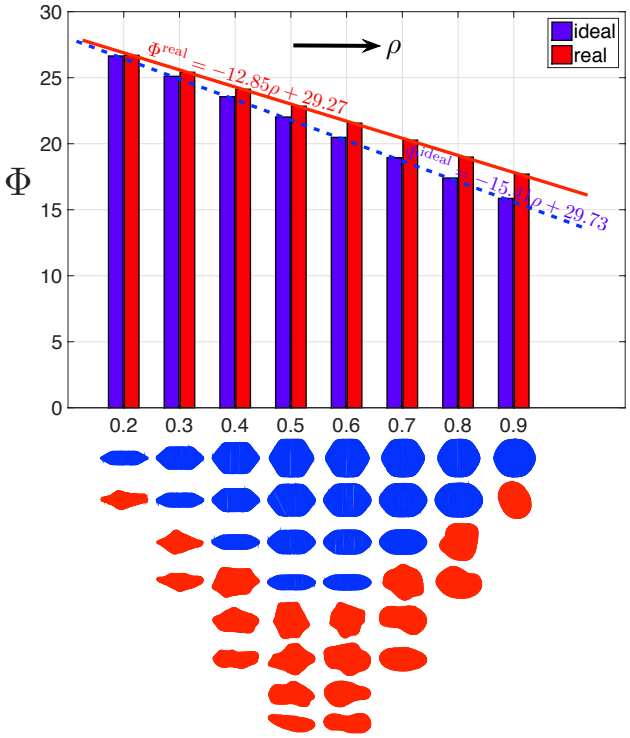

Figure 3.9: Values of the CS friction angle, Φ_{cs}, of ideal (blue columns) and real (red columns) particles sorted with respect to particle's regularity, ρ.

regarding the behavior of the aforementioned critical state parameters with respect to specifically sphericity and/or roundness is lost. These details are preserved and can be read in the contour levels shown in Figures 4.5, 4.7 and 4.9, which have been computed from 20 different grains according to values of roundness and sphericity shown by Figure 1 in [17].

As mentioned before, from the goodness of fitting we concluded that the contour levels corresponding to the surfaces $\lambda^{\text{real}}(S,R)$ and $\Gamma^{\text{real}}(S,R)$ are much smoother and flatter than the equivalent surfaces for idealized particles. This, in fact, is confirmed by Figures 4.5 and 4.7. Furthermore, note that Γ^{ideal} shows a lot of variation with a valley whose deepest level is reached at sphericity 0.7 and roundness going from 0.5 to 0.9. Within the same lines and ideas as before we introduce the following "topographic" analysis for each variable (surface).

λ^{real} **(Figure 4.5, Left):** in this case, the CSL's slope depends on both: roundness and sphericity, showing more dependency on the latter for lower values of the former, and a similar level of dependency on roundness for low values of

sphericity as well.

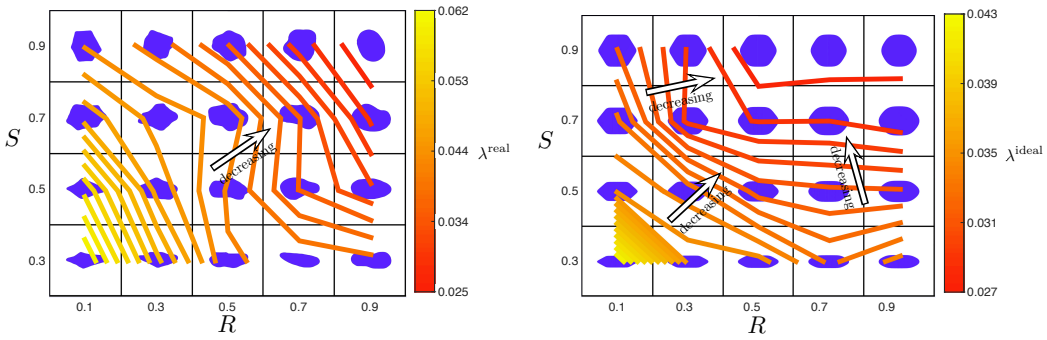

Figure 3.10: Left: $\lambda^{\text{real}}(S,R)$ surface contour lines. Right: $\lambda^{\text{ideal}}(S,R)$ surface contour lines. A simulation for each type of particle has been carried out always applying the same amount of normal pressure. Thus, 20 points (as in the table of Figure 1 in [17]) are obtained for each parameter: $\lambda^{\text{real}}(S,R)$ and $\lambda^{\text{ideal}}(S,R)$. Then, a surface is fitted for each case.

λ^{ideal} **(Figure 4.5, Right):** this variable depends on a similar level on sphericity and roundness. It shows high dependency on roundness for low values of sphericity and becomes almost independent on roundness for high values of sphericity. In the same way, it shows high dependence on sphericity for low values of roundness and lower dependency on sphericity for high values of roundness.

Γ^{real} **(Figure 4.7, Left):** this parameter seems to depend more on roundness than sphericity, depending more on the latter for low values of roundness and barely depending on sphericity for high values of the former. On the other hand, the CSL intercept of real particles shows dependency on roundness for high and low values of sphericity.

Γ^{ideal} **(Figure 4.7, Right):** in this case, the intercept shows high dependency on roundness for low values of sphericity, and little dependency for high values of sphericity. The intercept shows some dependency on sphericity for high values of roundness, and more dependency for low values of roundness. The surface also has a deep valley with its deepest level at sphericity 0.7 and roundness going from 0.5 to 0.9.

$\Phi_{\text{cs}}^{\text{real}}$ **(Figure 4.9, Left):** from the Figure, we conclude that this parameter depends more on sphericity than roundness, even though, this does not imply indepen-

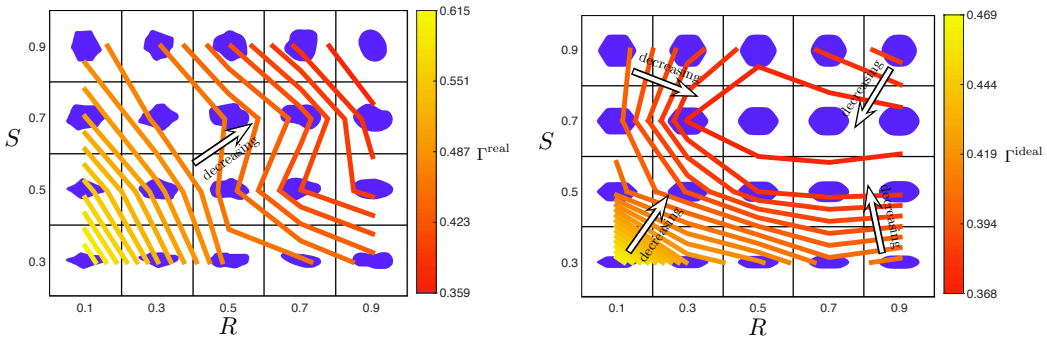

Figure 3.11: Left: $\Gamma^{\text{real}}(S,R)$ surface contour lines. Right: $\Gamma^{\text{ideal}}(S,R)$ surface contour lines. A simulation for each type of particle has been carried out always applying the same amount of normal pressure. Thus, 20 points (as in the table of Figure 1 in [17]) are obtained for each parameter: $\Gamma^{\text{real}}(S,R)$ and $\Gamma^{\text{ideal}}(S,R)$. Then, a surface is fitted for each case.

dency on the latter. The surface is crossed by a small "hill" going from the long hex to the disc (higher to lower point).

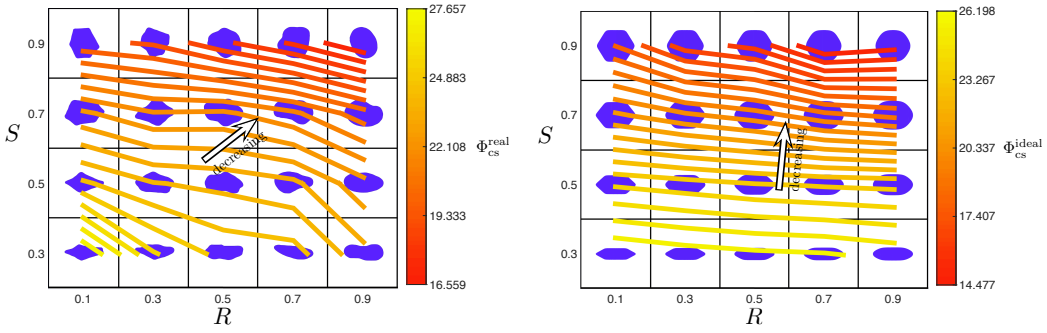

Figure 3.12: Left: $\Phi_{\text{cs}}^{\text{real}}(S,R)$ surface contour lines. Right: $\Phi_{\text{cs}}^{\text{ideal}}(S,R)$ surface contour lines. A simulation for each type of particle has been carried out always applying the same amount of normal pressure. Thus, 20 points (as in the table of Figure 1 in [17]) are obtained for each parameter: $\phi_{\text{cs}}^{\text{real}}(S,R)$ and $\phi_{\text{cs}}^{\text{ideal}}(S,R)$. Then, a surface is fitted for each case.

$\Phi_{\text{cs}}^{\text{ideal}}$ (Figure 4.9, Right): depends more on sphericity when roundness is high and less when roundness is low. At the same time, this parameter depends more on roundness when sphericity is high and barely depends on roundness when sphericity is low.

Finally, Table 3.2 has been designed to be used as a chart of recommendations.

For example, the fitting slope ratio (real/ideal), gives us information about which of the CS parameters are, in general, the most and least sensitive to idealization. Hence, a recommendation to be drawn if, for instance, the parameter of interest is Φ_{cs}, may be, in general, using idealized particles instead of real ones since the mentioned ratio shows, in this case, insensitiveness to idealization. Thus, a good enough, and also conservative, approximation of the value of Φ_{cs} could be obtained from the idealized particles. The same procedure cannot be applied for the other two CS parameters, and decisions about substituting real by ideal particles should be more carefully made according to further recommendations given in this section and summarized in Table 3.2.

	λ	Γ	Φ_{cs}
Fitting slope ratio (real/ideal)	≈ 2.55	≈ 3.4	≈ 0.83
CSP max var wrt ρ (Real)	$\approx 57\%$	$\approx 40\%$	$\approx 35\%$
CSP max var wrt ρ (Ideal)	$\approx 34\%$	$\approx 16\%$	$\approx 41\%$
Dependency (Real)	more on R than S, but on both	equally on R and S	more on S than R, but on both
Dependency (Ideal)	more on S than R, but on both	equally on R and S	mostly on S

Table 3.2: Dependency of the CSP on R, S, and Idealization.

3.5 Closure

We have introduced a new DEM scheme (LS-DEM) that, by means of the use of level sets, enables the inclusion of real grain shapes into a classical discrete element method. Furthermore, we have shown some of the most important capabilities and potentialities of LS-DEM by calibrating it to match actual experimental results not only qualitatively, but also quantitatively. This calibration has been then used to study the influence of grain morphology (sphericity, roundness, and regularity) on critical state (macroscopic) parameters such CSL slope and intercept as well as CS friction angle, for which we have been able to establish well defined trends and relationships. Moreover, we have investigated the importance that the amount of detail/accuracy used in capturing a real grains's shape can have on the values of the CS parameters. With this aim, we have also included idealized (simplified) grain shapes that are morphologically equivalent to the real grain shapes used in this study.

Thus, from Figures 4.2, 4.3, and 4.4 it is evident that, for ideal and real grain shapes, all the CSPs decrease as regularity (ρ) increases. Hence, and starting with the CSL slope (λ) decrease, we conclude that as grains are more regular, they reach their maximum compaction at lower pressures. In other words, compaction becomes

less pressure dependent as grain regularity increases. In addition, the decrease in the CSL intercept (Γ) tells us that more grain regularity means that regular grains reach CS at a more compacted stage than irregular grains, whereas a decrease in the CS friction angle (Φ_{cs}) suggests that more regularity implies less strength, i.e., grain irregularities contribute to the increase in the strength of a given array of grains.

Moreover, we have found that the CS friction angle is, in general, the CSP which shows less sensitiveness to idealization, so simplified geometries may be sometimes preferred to study or compute this parameter. In the same way, except for Φ_{cs}, CSPs computed from real grain shapes show more dependency on the grain's regularity than their counterparts from idealized grains. Finally, the CSL intercept appears as the only CSP that depends equally on roundness and sphericity. On the other hand, the dependency of the other two CSP is slightly more tilted towards sphericity than roundness. These main findings and observations have been summarized in Table 3.2, which could also be used as a consulting tool for basic clues about when it is possible to simplify a particle's shape in order to obtain a rough, but still good, approximation of the actual value of a given CS parameter.

Chapter 4

A GEOMETRY-BASED ALGORITHM FOR CLONING REAL GRAINS

In review: *Granular Matter*, GRMA-D-16-00049.

4.1 Introduction

The use of the discrete element analysis (DEM) in geomechanics [23, 22] has played an central role when it comes to understanding micro- and meso-mechanical behavior of granular media and its connections to the engineering (macro) scale [74, 67, 58, 3, 32]. The inclusion of arbitrary shapes within DEM schemes has been an object of research in the last thirty-five years [89, 65, 31, 4, 33]. Specifically, DEM schemes that are able to take into account real grain shapes began to be explored in the last fifteen years [7, 27, 89, 4]. Now, powerful experimental and numerical tools such as 3D X-ray computed tomography (3DXRCT), non-uniform rational B-splines (NURBS), and level sets (LS), have enabled us for the first time to develop DEM schemes [4, 34] (e.g. NURBS-DEM, LS-DEM) capable of creating numerical avatars from a sample of real grains and including them into DEM simulations.

The inclusion of real shapes in DEM simulations has provided goemechanicians with new capabilities to dig deeper into the answers to some fundamental scientific questions such as, *What is the effect of grain morphology in the mechanical meso- and macro- behavior of a confined granular medium subjected to loading conditions?* In other words, how is the macro-strength in a granular medium affected by grain morphology? [77, 17, 86, 36, 68, 37, 11].

Even though new DEM schemes previously mentioned have lent us new capabilities to perform more realistic and accurate simulations, it is difficult to obtain the requisite data for them: X-ray computed tomography (XRCT) equipment is usually expensive, needs experienced technicians to be manipulated, and is not available at every institution around the globe for practical purposes, and the size of the scanned samples is limited to a few thousand grains.

In the past two years there have been a few attempts to computationally simplify and overcome the experimental issues mentioned in the last paragraph, but these attempts have been more directed towards studying mathematical and numerical ways

of understanding in depth grain morphology as well as reconstructing it by means of Fourier series and spherical harmonics [94, 95], rather than directly addressing the issues in question. In the present work, we propose the first attempt to actually overcoming the mentioned issues by developing a *computational algorithm that is able not only to extract what we have called the morphological DNA of a sample of real grains, i.e., aspect ratio/sphericity, roundness, principal geometric directions, and spherical radius distributions, but also able to generate new "cloned" grains that satisfy these same properties*. Now, with this new tool, an arbitrary number of real shaped grains that satisfy certain morphological features can be generated at will and DEM simulations at any scale can be carried out, limited only by available computational power.

With this aim, once a real sample of grains (in this case we use a Martian regolith simulant) has been scanned using 3DXRCT, and the three dimensional images of each grain have been turned into a corresponding level set [85], the present study has been carried out in the steps depicted by Figure 4.1.

First, the algorithm extracts the morphological DNA from the digitalized sample of real grains (avatars). Second, once the morphological DNA has been extracted, the algorithm creates a basic structure called the clone's embryo (equivalent ellipsoid), by sampling [76] values from the parent's aspect ratio and minimum principal direction distributions. Third, the embryo is developed by sampling of radius values from the spherical distributions corresponding to each point of the embryo's spherical mesh. Finally, the embryo is "polished" with a laplacian (curvature) based smoother [52] until it matches a sampled roundness value.

We use the cloning algorithm to generate a pool of grains from which we re-extract the same morphological parameters (DNA) that were obtained from the parents. With this, we compare the clones' distributions to the corresponding ones obtained from a similar pool randomly picked from the sample of parents. Conclusions, observations, guides, and recommendations about the quality and efficiency of the cloned grains as well as the cloning algorithm are drawn. Then, the volume-surface ratio distribution (a parameter not involved in the cloning process) is also computed from both pools. This is used for results verification and quality control (error/mutation). We close the present work by analyzing and describing the algorithm's drawbacks and knobs (parameters) as well as potential improvements.

Finally, it is worth mentioning that the algorithm introduced by the present work is not a genetic algorithm [47]. Here, the use of similar jargon may misguide the

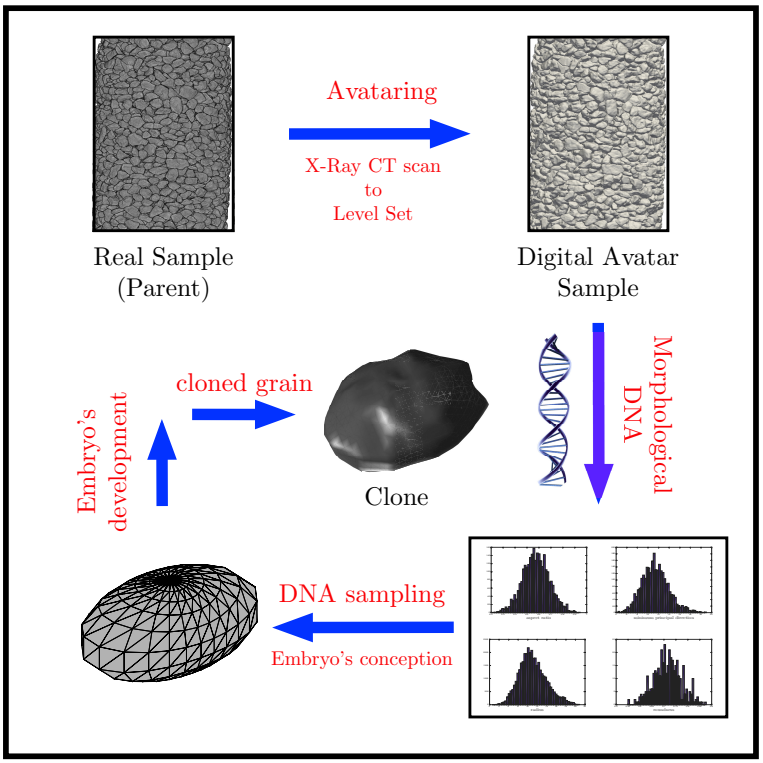

Figure 4.1: Granular digital cloning process: here we describe the process of digital cloning of a grain taken from a specific type of granular material (e.g. Martian regolith simulant). A grain from a real sample is first turned into a 3D image and then converted into a level set, which allows us to digitally compute the grain's morphological parameters (aspect ratio, roundness, principal directions, etc.). This process is repeated for each grain of the sample and distributions of the morphological parameters are drawn (morphological DNA extraction). Then, new genes (morphological parameters) are randomly sampled from these distributions so an embryo (equivalent ellipsoid) can be generated and developed giving birth to a new grain (clone) that bears the same morphological features as the grains in the parent sample but is not equal to any of them.

reader and cast some confusion on whether or not the introduced algorithm is part of a family of genetic algorithms. Thus, for instance, the geometric stochastic algorithm (GSC) being introduced does not have objective nor fitness functions as in the case of genetic algorithms. Moreover, the former does not optimize a population of candidate solutions as in the case of the latter. Instead, our algorithm randomly samples morphological parameters computed from a pool of "parents" (real grains), which are not considered to be a possible solution to any given problem, and therefore, need no further optimization as in the case of genetic algorithms. In that sense, our algorithm, combines the morphological parameters randomly sampled from the

"parents" to geometrically create new grains that match those parameters, reason why we have called it a geometric stochastic cloning (GSC) algorithm. Furthermore, a cloning process for grain's morphology could also be designed in terms of genetic algorithms, and some similarities with GSC may be found. However, in our case, we have used a Monte Carlo sampling method [76] which makes the cloning process simpler in terms of structure and coding.

4.2 Extracting the morphological DNA from a sample of real grains

For this part of the process we have already obtained the corresponding numerical avatars of the real grains [33, 85, 6], so a level set (LS) function $\phi(\boldsymbol{x})$ for each grain has been computed. We use $\phi(\boldsymbol{x})$ to extract what we consider to be the morphological DNA, i.e., aspect ratio, minimum principal directions, roundness, volume/surface ratio and spherical radius distributions of a whole sample of sand grains (Martian regolith simulant) as shown by Figures 4.2, 4.3, 4.4, and 4.5, respectively. In the aforementioned process we use the definition of roundness given by [17], which is also combined with a laplacian method that allows us to compute the radius of curvature ($r \propto 1/\Delta\phi(\boldsymbol{x})$) at different points of each grain's surface. In the same way, we use $\phi(\boldsymbol{x})$ to numerically compute all the other morphological features herein mentioned.

Thus, for the aspect ratio distributions (Figure 4.2), note that the Martian regolith simulant has a mean aspect ratio of 0.58 and a standard deviation of 0.11. Since the distribution has a gaussian shape, we conclude that 68% of the grains have aspect ratios between 0.47 and 0.69. Furthermore, since the aspect ratio is, in fact, a measure of sphericity, this information suggests that most of the grains tend to be slightly spherical, or, at least, elliptically shaped (elongated).

The grains' minimum principal directions distribution (see Figure 4.3) also follows a gaussian shape with mean 0.71 mm and standard deviation of 0.16 mm, which implies that most of the grains have minimum diameters between 0.55 and 0.87 mm, implying that Martian regolith simulant can be, in fact, classified as sand.

The distribution corresponding to the grains' roundness also deserves some statistical analysis (see Figure 4.4). In this case, note that the mean has a value of 0.62 with a corresponding standard deviation of 0.1, which suggests that most of the grains have roundness between 0.52 and 0.72 from where we conclude that, in general, Martian regolith simulant can be considered to be composed by a mix which goes from grains with smooth enough surfaces to grains with edges and vertices.

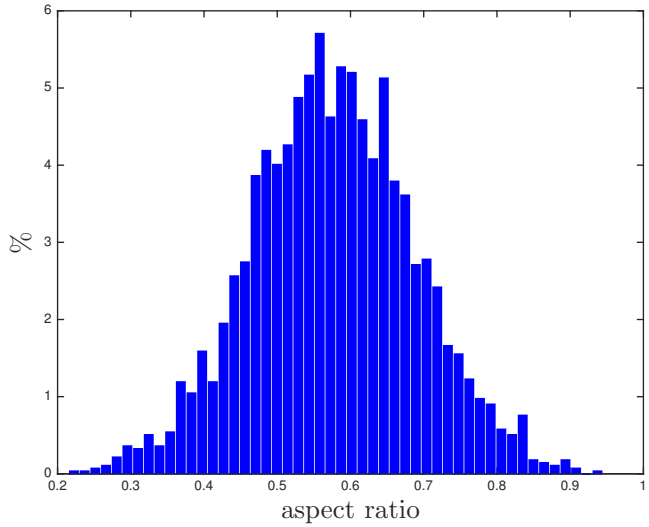

Figure 4.2: Aspect ratio distribution corresponding to a sample of Martian regolith simulant containing 2769 grains.

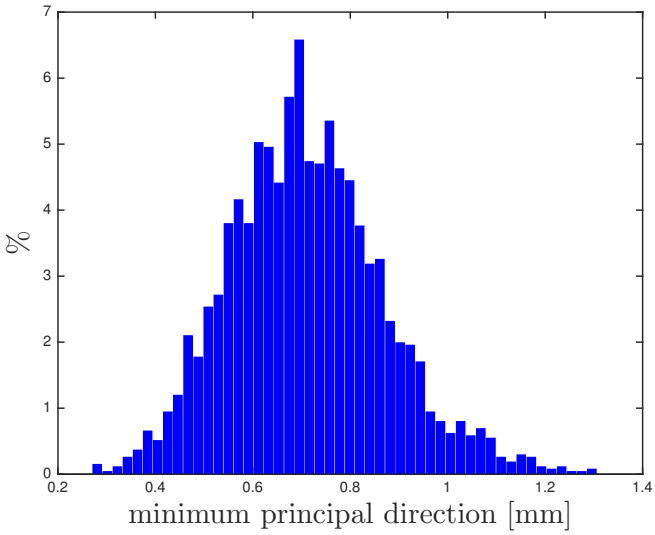

Figure 4.3: Minimum principal directions distribution obtained from a sample of Martian regolith simulant made of 2769 grains.

Now, for the volume-surface ratio note from Figure 4.5 that this distribution has a mean of 0.12 mm and a standard deviation of 0.023. Hence, most of the grains have volume-surface ratios between 0.097 and 0.143 mm, which implies that Martian regolith simulant grains, in general, have many edges, flat faces and vertices as previously inferred from the grains roundness distribution (see Figure 4.4). Fur-

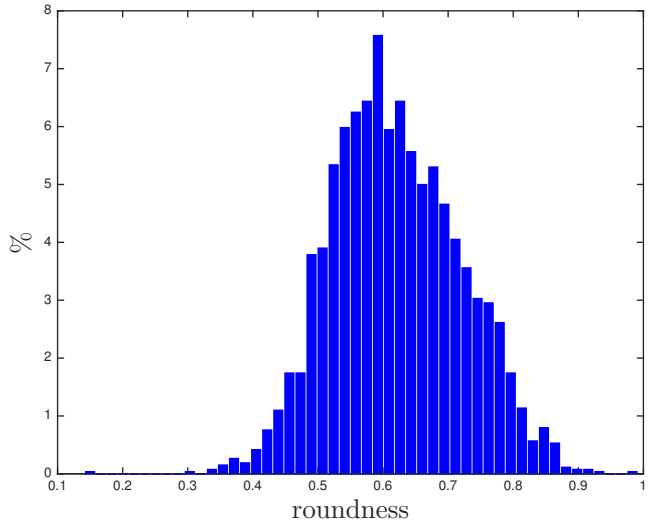

Figure 4.4: Roundness distribution computed from a sample of Martian regolith simulant with 2769 grains.

thermore, since the cloning algorithm does not use this distribution to generate the clones from the parents, we use this distribution later on this work to keep track of the error and mutation of the clones.

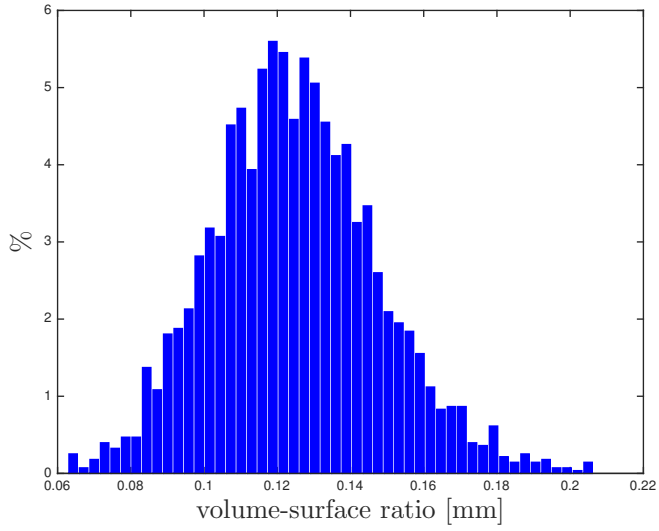

Figure 4.5: Volume-surface ratio distribution extracted from a sample of Martian regolith simulant made of 2769 grains.

Spherical radius distributions

We can also use the LS function to create a distribution $f(R)$ of radius R for each given couple $(0 \leq \Phi \leq 2\pi, 0 \leq \Theta \leq \pi)$ (azimuthal and polar angles) from the entire sample as shown in Figure 4.6. Then, for the mentioned sampling, we first split the azimuthal and polar directions into a number of equally spaced discrete points. Then, we get the values of all the grain's spherical radius at the same coordinate point (Φ, Θ), which is taken as the center of a "rectangle" whose boundaries are located at half the distances between (Φ, Θ) and the previous and next mesh points in the azimuthal and polar directions, respectively, and from where the radius distribution corresponding to (Φ, Θ) is obtained. In order to give consistency to this calculation, we have previously rotated the grains so they align to their corresponding principal directions, taking the longer and shorter ones as $(\Phi = 0, \Theta = \pi/2)$ and $\Theta = \pi$ (north pole), respectively.

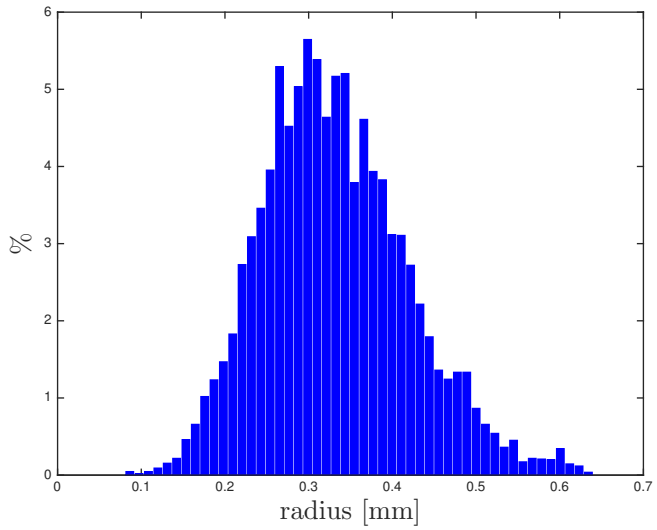

Figure 4.6: Grain radius distribution drawn from a sample of Martian regolith simulant made of 2769 grains. This distribution corresponds to all the grain's radius at $(\Phi = \pi/16, \Theta = 15\pi/16)$ of a spherical mesh split into $16 \times (8 + \text{poles})$ discrete points along the azimuthal and polar directions, respectively.

4.3 Cloning algorithm: from embryo to clone

Once we have extracted the grain's morphological DNA as described in Section 4.2 and Figure 4.1, a new grain that satisfies these morphological features, but is not equal to any of its "parents", can be now generated by using this so-called DNA. For this, we have come up with a process based on stochastic sampling from the distri-

butions obtained in Section 4.2 by means of a Monte Carlo method [76]. Since the aforementioned process uses stochastic sampling of geometrically meaningful features (grain morphology) to generate new grains "clones" that satisfy these features, it can be considered as a geometric stochastic cloning (GSC) process.

Geometric stochastic cloning algorithm

As mentioned at the beginning of the current section, we use a Monte Carlo method to sample the morphological DNA features from the distributions obtained from the parent grains as described in Section 4.2. However, a cloning algorithm had to be designed so any number of new "clones" can be generated in the same consistent and methodological way.

Embryo's conception: equivalent ellipsoid

The first step in the cloning algorithm is generating a grain's embryo (see Figure 4.7). Thus, we first Monte Carlo sample a value from the parents aspect ratio distribution (see Figure 4.2). Once we have obtained the mentioned aspect ratio value, we proceed to sample a minimum principal direction value (see Figure 4.3). Then, using these two values we compute a corresponding maximum principal direction: **aspect ratio** = **min.-prin.-dir.**/**max.-prin.-dir.**. Finally, using the values of the minimum and maximum principal directions, a mid principal direction is uniformly sampled $U($**min.-prin.-dir.**, **max.-prin.-dir.**$)$. Then, once all the principal directions have been computed, an ellipsoid (embryo) is generated in spherical coordinates by using the same spherical mesh as the previously used to extract the spherical radius distributions from the parents. An equivalent ellipsoid or embryo is shown by Figure 4.7.

Embryo's development: shape and roundness matching

Once the embryo has been generated (see Figure 4.7), the next step in the cloning algorithm is to develop the embryo into an actual digitally cloned grain. We now use the spherical radius distributions $f(R)$ (see Figure 4.6) previously obtained from the parent grains and described in Subsection 4.2. Then, since these distributions are gaussian, we can rewrite them in the form $f(R \mid \mu, \sigma^2)$, where μ is the mean and σ is the standard deviation. Thus, if $f(R \mid \mu, \sigma^2)$ is the spherical radius distribution corresponding to a given point (Φ, Θ) in the mesh, we look for the same point in the mesh of the equivalent ellipsoid, which already has a corresponding radius R^*. Then, we make $\mu = R^*$, so we end up with a distribution $f(R \mid R^*, \sigma^2)$ from

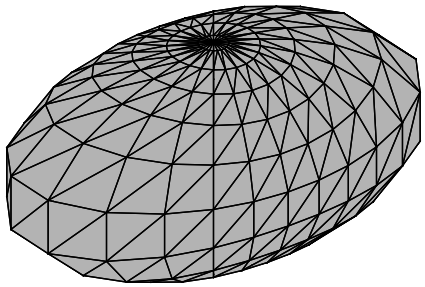

Figure 4.7: Grain's embryo (equivalent ellipsoid) with a spherical mesh of 16 × (8 + poles) discrete points along Φ and Θ, respectively.

where a radius value R^{**} is randomly sampled and assigned to that point of the equivalent ellipsoid. In other words, each (Φ, Θ, R^{*}) in the equivalent ellipsoid mesh evolves into (Φ, Θ, R^{**}) in the developing embryo's mesh. Furthermore, it is worth mentioning that the mesh used to develop the embryo into a clone has to be consistent with the mesh used to extract the radius distributions from the parents, i.e., if a spherical mesh of 16 × (8 + poles) discrete points along Φ and Θ was used to extract the radius distributions from the parents, the same mesh has to be used to sample the corresponding values of the radius at the same points.

Then, once the clone's spherical mesh has been generated, we turn it into an LS function whose grid can be calibrated at will for more or less accuracy. At this point, the cloning algorithm proceeds to generate new embryos until they match the size of the pool of clones to be generated. With all the embryos' LS functions, Monte Carlo sampling is again applied to the roundness distribution previously obtained from the parent grains (see Figure 4.4), and an equivalent number of roundness values are randomly picked from it. In addition, each embryo's roundness is computed. Then, the randomly sampled roundness and the embryos roundness are sorted as well as matched in a one-to-one correspondence. If the embryo's roundness is lower than its corresponding randomly sampled roundness, a laplacian (curvature) based algorithm [52] is applied so the embryo is "polished" until it reaches the sampled roundness, otherwise the embryo is left unpolished and the process is repeated for

the whole pool of embryos. Here, the clones development is ended and their LS saved. Figure 4.8 shows 5 parent grains (digital avatars) and 5 cloned grains of Martian regolith simulant.

4.4 Mutation: algorithm's error and morphological equivalence

In this section we evaluate the main morphological features of the cloned grains with respect to the ones obtained from their original counterparts. Two samples of Martian regolith simulant (parents and clones) of 1000 grains each, are analyzed.

First, we compare the aspect ratio distributions of parents and clones (see Figure 4.9). As can be noted from the figure, parents (red line) and clones (blue line) have very similar aspect ratio distributions. However, note that the mean of the the clones distribution is off with respect to the mean of the parents distribution with an error of 11.16%, while the standard deviation of the clone's distribution has an error of 1.23% with respect to its counterpart.

In the case of roundness, as shown by Figure 4.10, the distributions of parents and clones (red and blue lines) have an error of 0.48% corresponding to the mean of one distribution with respect to the mean of the other, and an error of 7.07% in the case of the standard deviations.

This errors come from the left tail of the clones roundness distribution (see Figure 4.10). As described at the end of Subsection 4.3, we Monte Carlo sample roundness values from the parents' roundness distribution, then we compute the developed embryos' roundness and sort the values creating a one-to-one correspondence: in the cases where an embryo's roundness is lower than its corresponding sampled roundness, the embryo is polished with the laplacian (curvature) based algorithm until matching the sampled value, if the embryo's roundness is higher than its corresponding sampled value the embryo is left unpolished. Thus, as the cloning algorithm is currently calibrated, it is generating embryos with minimum roundness values around 0.44, as can be noticed from Figure 4.10. Hence, further calibration of the cloning algorithm as well as research are needed in order to improve the the clones' roundness matching for lower values.

On the other hand, for the diameters distributions of parents and clones (see Figure 4.11, left), the means of the distributions are off with an error of 1.77%, while the error coming from standard deviations is 19.45%. The parents yield a coefficient of uniformity $C_u = D_{60}/D_{10} = 1.41$ and a coefficient of curvature $C_c = D_{30}/(D_{10} \times D_{60}) = 0.95$, that are similar to the ones obtained from the clones $C_u = 1.49$ and

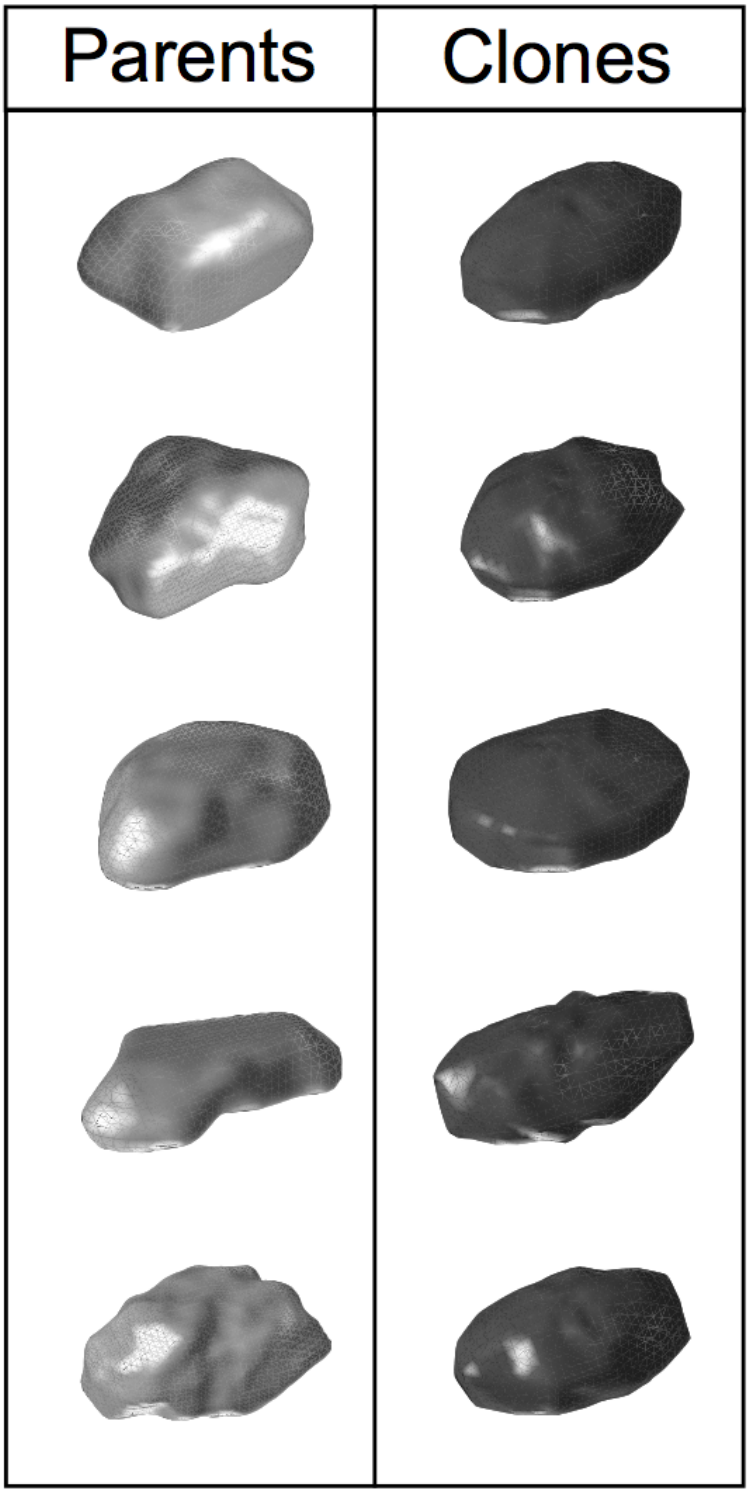

Figure 4.8: Random samples for visual inspection: five parents (left column) and five clones (right column) of Martian regolith simulant.

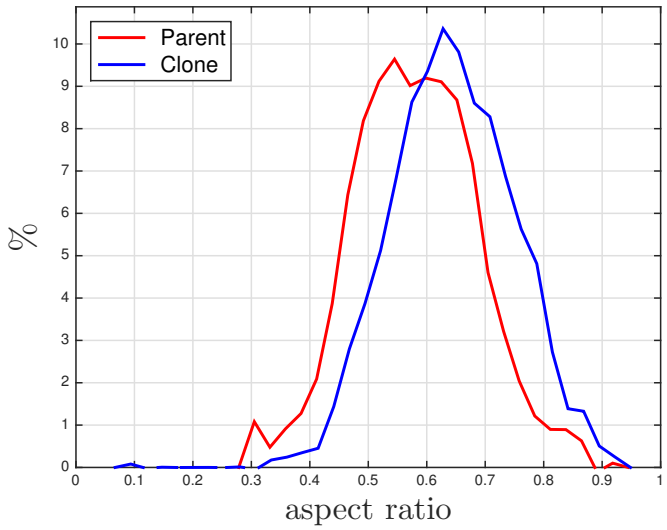

Figure 4.9: Aspect ratio distributions taken from samples of parents and clones (1000 grains each) of Martian regolith simulant.

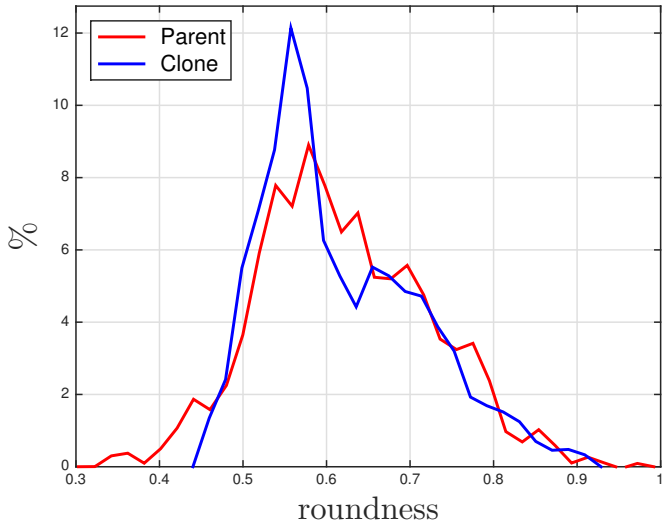

Figure 4.10: Roundness distributions computed from samples of parents and clones (1000 grains each) of Martian regolith simulant.

C_c = 0.93, where D_{10}, D_{30}, and D_{60} are the grain diameters at 10, 30, and 60% passing, respectively. Note that C_c is almost the same for parents and clones giving an error of 1.5%, while in the case of C_u there is an error of 5.84%, as can be inferred from Figure 4.11 (right), which shows that parents and clones have almost the same D_{60}, and similar values of D_{30} as well as D_{10}.

Note that the source of error in the standard deviations is given by the right tail of the clones distribution, which corresponds to few rare cases with bigger diameters (here some mutation introduced by the algorithm itself). This error can be considered as negligible if we take a look at the coefficients C_u and C_c, which are very similar for both parents and clones.

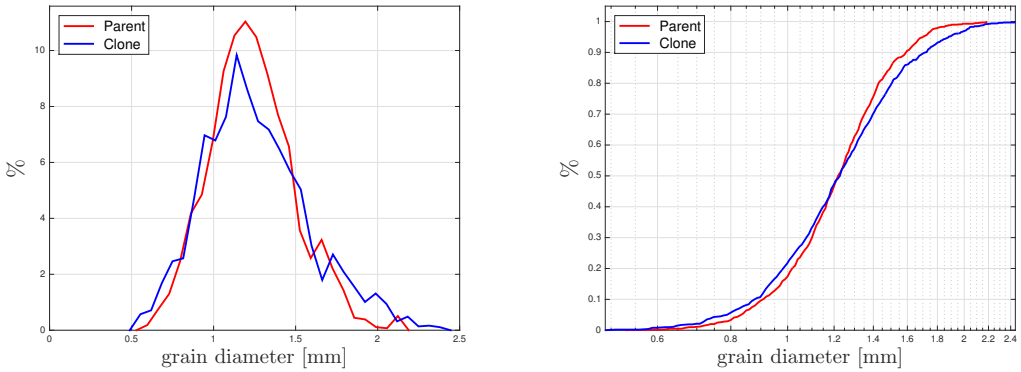

Figure 4.11: Left: grains diameter distributions drawn from samples of parents and clones (1000 grains each) of Mohave regolith simulant. Right: percentage of grains passing versus $\log(D)$, where D is the grain's diameter, and corresponding to the left figure.

Finally, for the volume-surface ratio distributions, as depicted by Figure 4.12, we have obtained an error given by the means misalignment of 4.01%, and an error of 36.57% in the case of the standard deviations. As can be inferred from the cloning algorithm described in Section 4.3, we did not aimed to match the volume-surface ratio. However, note, from this analysis and Figure 4.12, that the error of the means is small and, therefore, this parameter is also nailed by the cloning process, at least, in the case of Martian regolith simulant.

Moreover, note that the error given by the standard deviations is induced once again by the tails of the clones' distribution, showing a few cases of mutation due to the algorithm itself.

Cloning algorithm drawbacks

This is a first attempt to successfully generate new computational grains that statistically "inherit" the morphological features displayed by their parents (a sample of digitalized real grains). Thus, the algorithm herein described can be seen as the "dummy algorithm" of grain cloning. Therefore, it possesses some flaws and

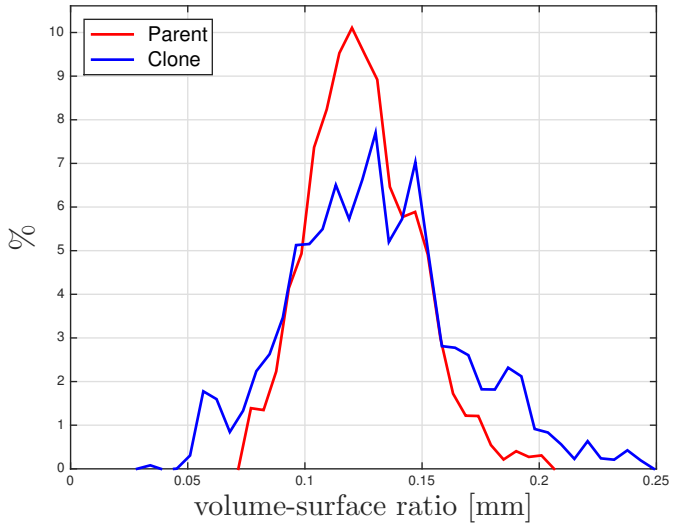

Figure 4.12: Volume-surface ratio distributions obtained from samples of parents and clones (1000 grains each) of Martian regolith simulant.

drawbacks that can be improved and overcome with an extra amount of work and research.

In this subsection, we broadly describe the main flaws and drawbacks related to the cloning algorithm, which could be improved in order to obtain a better quality in the morphological properties inherited by the clones, so the error (mutation) in the clone grains' morphological parameters is minimized.

Roundness calculation

The first challenge that we faced when beginning with the present work was the numerical computation of roundness from a digital (LS or any other computational representation) version of a real grain. As described in Section 4.2, we stuck to the definition provided by [17] and used a finite difference laplacian method to obtain the radius of curvature at each point of a grain's surface. Here we found the first source of error. Since we decided to use a finite difference method that is first applied at the grid points which are closer to the actual grain surface point, and then, linear interpolation is also applied to find the laplacian's value at the surface point. Here we have a source of error that comes not only from the finite difference scheme used but also from the linear interpolation. Note that this source of error could be improved by using a finite difference scheme with a more sophisticated stencil as well as higher order interpolation.

Both the finite difference and the linear interpolation errors, can be improved by using a finer LS grid, but this would notably increase computational cost. Thus, further research has to be done to improve the accuracy of these computations with coarse LS grids.

On the other hand, from the definition of roundness introduced by [17], the radius of curvature is to be computed only at certain important points ('corners') on the grain's surface. These points can be visually and intuitively found by a technician with some experience in computing grain roundness, but there is no a simple enough way of telling the computer what surface points to use or not for the computation of the grain roundness. The algorithm uses only the grain's surface points where the radius of curvature is less than that of the radius of the maximum sphere that can be inscribed in the grain. This introduces an error related to overestimation of this property.

In this regard, more research is needed to develop an algorithm capable of "recognizing" the crucial morphological points involved in the calculation of roundness.

Roundness Matching

As described in Section 4.4, the lowest roundness values of the developed embryos tend to be higher than the parents lowest roundness values. This implies that further tuning is needed for the cloning algorithm in order to generate developed embryos with lower roundness values so they can be "polished" until matching lower roundness values sampled from the parents distribution.

Moreover, the embryo's roundness is also computed using the the same finite difference scheme previously described in this subsection, which means that there is error coming from that part of the method. Since each developed embryo is polished until it matches a corresponding sampled roundness value, we have an iterative process, in which for each iteration, a laplacian (curvature) based polisher (with its own source of error) is used, and then the embryo's roundness is computed once again to check if its current state of development has matched the sampled roundness value. Thus, for each iteration we have a source of error (mutation) coming from the roundness calculation and from the polishing algorithm. Finally, it is worth mentioning that level set reinitialization could also be included in the future as part of the roundness matching algorithm to obtain more accurate results.

Algorithm knobs

When developing algorithms that attempt to tackle or approach physically driven phenomena, it is almost a rule of thumb to find parts where "knobs", i.e., tolerances, coefficients, or ranges have to be included as well as tuned in order to obtain the desired results. A whole brach of research is actually devoted to reduce these so-called knobs and optimize algorithmic efficiency. This may go from new physical models to pure code optimization.

Thus, in this first attempt to develop an algorithm that efficiently generates morphological clones out of a sample of real grains, as can be expected, we have also included a few "knobs" that are briefly described in the following lines.

A first knob has to do with the number of cells that want to be used to generate the clone's level set grid. This not only affects the computational cost but also changes the accuracy of the morphological properties being obtained. A second knob is related to the spherical mesh used for both, sampling the parents radius distribution at a given point (Φ,Θ) as wells as generating the embryo (equivalent ellipsoid) and developing it from the stochastic sampling of the radius distribution at a given spherical point. Here, we also have a third knob that controls how broad the sampling process is with respect to each radius distribution mean $\mu = R^*$. We have included this knob in order to avoid the sampling of "rare" cases (tails) in the radius distribution $f(R \mid R^*, \sigma^2)$ for each (Φ,Θ) that could lead to the generation of "deformed" clones. Hence, we tune this knob in terms of standard deviations.

A fourth knob is assigned to the accuracy (LS grid size) that is required for the clone's LS. A fifth knob takes care of the number of points on the embryo's LS surface used to compute its roundness at each iteration of the "polishing" process to match a given sampled roundness value from the parents distribution. Two final knobs come from the laplacian based polisher. These control the intensity (attack) and the number of iterations to be done within the laplacian based polisher for each iteration of the roundness matching algorithm.

Therefore, we end up with seven knobs to be carefully tuned throughout the grain cloning algorithm in order to reach "good enough" results. Finally, it is worth mentioning that these knobs can be further tuned in order to achieve more accurate results than the ones obtained for the present work.

4.5 Closure

We have introduced a computational algorithm that enables us to "clone" the grain morphologies of a sample of real digitalized grains (avatars). This gives us the capability of generating as many cloned grains as desired, so a numerical DEM simulation can be carried out with an arbitrary amount of grains (limited only by the user's computational power), which satisfy the same morphological features displayed by their real parents, yielding a similar mechanical response.

The algorithm is morphology/geometry based, relying purely on statistical distributions of what we have called the grain's "morphological DNA", i.e., aspect ratio, roundness, principal geometric directions, and spherical radius. Once this morphological DNA has been computationally extracted from the digitalized sample of real grains, the algorithm creates a basic structure called the clone's embryo (equivalent ellipsoid), by Monte Carlo sampling values from the parent's aspect ratio and minimum principal direction distributions. Then, the embryo is developed by sampling radius values from the spherical distributions corresponding to each point of the embryo's spherical mesh. Finally, the developed embryos' roundness are computed as well as corresponding roundness value are sampled from the parents distribution and the developed embryos are "polished" with a laplacian (curvature) based smoother until matching the sampled roundness value.

Then, we used the cloning algorithm to generate a pool of 1000 grains from which we have re-computed the same morphological parameters (DNA) that were extracted from the parents and used for the clones creation. We compared their distributions to the corresponding ones obtained from a pool of the same size and made out of randomly picked parents. The results are shown in Section 4.4, Figures 4.9 to 4.11. We concluded that the clones, in general, morphologically match their parents.

Moreover, from the pool of clones we also computed the volume-surface ratio distribution and compared to results obtained from the parents (see Figure 4.12). Note that this parameter is not part of the cloning algorithm but instead was used for quality control. From the results, we conclude that even though the volume-surface ratio is not part of the cloning process, the algorithm is capable of matching it as well. Finally, the algorithm drawbacks, knobs and potential improvements are analyzed as well as described in Subsection 4.4.

Chapter 5

CONCLUSIONS AND FUTURE WORK

5.1 Conclusions

This thesis presented the development and use of an analytical-computational framework to deepen the understanding of physical relations between continuum and grain scales in confined granular media subjected to arbitrary loading. For this, on the computational side, we have used, tested, and developed cutting-edge discrete element schemes (DEM) that go from polydisperse granular packings made only of discs to three dimensional granular "cloning", passing through the use of real two and three dimensional granular shapes (avatars). On the analytical side, with help of the aforementioned computational tools, we have derived expressions as well as trends that, in turn, allowed us to unravel some important physical connections between grain and continuum scales.

First, material peak strength (friction angle) and critical state (dilation angle) were directly related to forces, kinematics, and fabric at the grain level. Hence, we inferred two necessary and sufficient conditions that can be applied to both: continuum and grain scale levels, and that, at the same time, give us a deeper insight on the underlying frictional micro-mechanisms furnishing macroscopic peak behavior and related buckling phenomenon. Moreover, for critical state, this procedure helped us to analytically understand the dominant micro-kinematical mechanisms driving the macroscopic behavior. Thus, enabling us to analytically proof the independence and sensitiveness of the residual strength on high and low values of the inter-particle friction coefficient, respectively.

Second, we apply a new DEM scheme (LS-DEM) that, by means of the use of level sets, enables the inclusion of real grain shapes into a classical discrete element method. Then, we used this to dig deeper into the physical connections between grain and continuum scales by studying the influence of grain morphology (sphericity, roundness, and regularity) on critical state parameters such as CSL slope and intercept as well as CS friction angle, for which we have been able to establish well defined trends and relationships. Furthermore, we have also inquired into the importance that the amount of detail/accuracy used in capturing a real grains's shape can have on the CS parameters.

Third, we introduced a first geometric stochastic cloning (GSC) algorithm to "clone" the grain morphologies of a finite sample of real digitalized grains. This enables us to generate as many cloned grains as desired, so a numerical DEM simulation is now limited only by the user's computational power. These cloned grains satisfy the same morphological features displayed by their real parents, hence yielding a similar mechanical response. The algorithm relies on statistical distributions of the "morphological DNA", that is first computationally extracted from a digitalized sample of real grains. Then, the algorithm uses Monte Carlo samplings to create a basic structure called the clone's embryo, which is further developed with the help of Monte Carlo samplings and the use of a laplacian (curvature) based smoother. Finally, a sample of one thousand clones is generated and its morphological parameters are compared to their counterparts from a similar sample with the same number of grains, which were randomly sampled from the original real sample (Mohave regolith simulant).

5.2 Future Work

Many possible directions can be explored in the future to broaden the scope of the analytical-computational framework that we have introduced in this thesis. An immediate step to take would be looking for analytical expressions that include the effects of grain morphology on the macroscopic strength, i.e., friction and dilation angles. In the same way, here we have inquired into the connections between grain and continuum scales in two dimensional packings (plain strain). Then, it would be very important to expand the framework herein introduced to three- dimensional packings by, once again, taking advantage of the three-dimensional level set avataring process and the cloning algorithm introduced in Chapter 4. In this regard, the main drawbacks as well as possible improvements of the cloning algorithm have been detailed in subsection 4.4, so the algorithm can be further improved and used to help to enrich the analytical-computational framework introduced in chapters 2 and 3.

We close this thesis by asking the following fundamental questions concerning the micro-macro connections in three-dimensional granular materials, for which the answers are currently unclear or need further research:

1. *What are the effects of grain morphology on two and three-dimensional granular media peak strength?*

2. *What are the effects of grain morphology on three dimensional granular media critical state parameters?*

3. *In what percentage the improvements that we have suggested here for the cloning algorithm will actually enhance it? Or are there other and better ways of optimizing it?*

Here, homogenization theory, mathematical techniques of optimization, other stochastic schemes, and further developments in level set methods may provide the necessary tools as well as ideas to properly address these questions.

BIBLIOGRAPHY

[1] F. Alonso-Marroquin and H. J. Herrmann. “Calculation of the incremental stress-strain relation of a polygonal packing”. In: *Physical Review E* 66 (2002), p. 021301.

[2] A. Anandarajah. “Critical state of granular materials based on the sliding-rolling theory”. In: *Journal of Geotechnical and Geoenvironmental Engineering* 134 (2008), pp. 125–135.

[3] J. E. Andrade and C. F. Avila. “Granular element method (GEM): linking inter-particle forces with macroscopic loading”. In: *Granular Matter* 14 (2012), pp. 1–13.

[4] J. E. Andrade et al. “Granular Element Method for Computational Particle Mechanics”. In: *Computer Methods in Applied Mechanics and Engineering* 241-244 (2012), pp. 262–274.

[5] J. E. Andrade et al. “Multiscale modeling and characterization of granular matter: from grain scale kinematics to continuum mechanics”. In: *Journal of the Mechanics and Physics of Solids* 59 (2011), pp. 237–250.

[6] J. E. Andrade et al. “Multiscale ‘tomography-to-simulation’ framework for granular matter: the road ahead”. In: *Géotechnique Letters* 2 (2012), pp. 135–139.

[7] A.K. Ashmawy, B. Sukumaran, and A. V. Hoang. “Evaluating the influence of particle shape on liquefaction behavior using Discrete Element Method”. In: *Proceedings of the thirteenth international offshore and polar engineering conference (ISOPE 2003) Honolulu, Hawaii*. 2003.

[8] K. Bagi. “Analysis of microstructural strain tensor for granular assemblies”. In: *International Journal of Solids and Structures* 43.10 (2006), pp. 3166 – 3184.

[9] K. Bagi. “Microstructural stress tensor of granular assemblies with volume forces”. In: *Journal of Applied Mechanics* 66.4 (1999), pp. 934 –936.

[10] K. Bagi. “Stress and strain in granular assemblies”. In: *Mechanics of Materials* 22.3 (1996), pp. 165 –177.

[11] P. J. Barrett. “The shape of rock particles, a critical review”. In: *Sedimentology* 27.3 (1980), pp. 291–303.

[12] M.D. Bolton. “The Strength and Dilatancy of Sands”. In: *Géotechnique* 36.1 (1986), pp. 65 –78.

[13] S. Bonelli et al. “On the denition of an average strain tensor for two-dimensional granular material assemblies”. In: *International Journal of Solids and Structures* 49.7-8 (2012), pp. 947–958.

[14] R. I. Borja. *Plasticity Modeling and Computation*. Springer, 2013.

[15] R. I. Borja and J. E. Andrade. "Critical state plasticity, Part VI: Meso-scale finite element simulation of strain localization in discrete granular materials". In: *Computer Methods in Applied Mechanics and Engineering* 195 (2006), pp. 5115–5140.

[16] B. Cambou et al. "Homogenization for granular materials". In: *European Journal of Mechanics* A/Solids 14.2 (1995), pp. 255–276.

[17] G. C. Cho, J. Dodds, and J. C. Santamarina. "Particle shape effects on packing density, stiffness, and strength: Natural and crushed sands". In: *Journal of Geotechnical and Geoenvironmental Engineering* 132.5 (2006), pp. 591–602.

[18] J. Christoffersen, M. M. Mehrabadi, and S. Nemat-Nasser. "A micromechanical description of granular material behavior". In: *Journal of Applied Mechanics* 48 (1981), pp. 339–344.

[19] G. Combe et al. "Experimental evidence of granulence". In: *AIP Conference Proceedings*. Vol. 1542. Sydney, Australia, 2013, pp. 453 –456.

[20] S. L. Conway, T. Shinbrot, and B. J. Glasser. "A Taylor Vortex Analogy in Granular Flows". In: *Nature* 431 (2004), pp. 433–437.

[21] C. A. Coulomb. "Essai sur une application des règles de maximus et minimis à quelques problèmes de statique relatifs à l'architecture". In: *Memoires de Mathématique et de Physique, Présentés a l'Académie Royale des Sciences, par divers Savans, et lûs dans ses Assemblées* 7 (1776), pp. 343–382.

[22] P. A. Cundall. "Formulation of a three-dimensional distinct element model - Part I: A scheme to detect and represent contacts in a system composed of many polyhedral blocks". In: *International Journal of Rock Mechanics and Mining Sciences* 25.3 (1988), pp. 107–116.

[23] P. A. Cundall and O. D. L. Strack. "A discrete numerical model for granular assemblies". In: *Géotechnique* 29 (1979), pp. 47–65.

[24] R. G. Deissler. *Turbulent Fluid Motion*. Combustion. Taylor & Francis, 1998.

[25] D. C. Drucker and W. Prager. "Soil mechanics and plastic analysis or limit design". In: *Quarterly of Applied Mathematics* 10 (1952), pp. 157–165.

[26] S. A. Galindo-Torres et al. "Breaking processes in three-dimensional bounded granular materials with general shapes". In: *Computer Physics Communications* 183 (2012), pp. 266–277.

[27] X. Garcia and J.-P. Latham; J. Xiang; J.P. Harrison. "A clustered overlapping sphere algorithm to represent real particles in discrete element modelling". In: *Geotechnique* 59 (9 2009), pp. 779–784.

[28] S. A. Hall et al. “Discrete and continuum analysis of localized deformation in sand using X-ray micro CT and volumetric digital image correlation”. In: *Géotechnique* 60 (2010), pp. 315–322.

[29] H. Hinrichsen and D. E. Wolf, eds. *The Physics of Granular Media*. Weinheim: Wiley-VHC Verlag GmbH & Co. KGaA, 2004.

[30] G. T. Houlsby. *How the Dilatancy of Soils Affects their Behaviour*. Soil Mechanics Report 121. University of Oxford, 1991.

[31] G. T. Houlsby. “Potential particles: a method for modelling non-circular particles in DEM”. In: *Computers & Geotechnics* 36 (2009), pp. 953–959.

[32] Alex X. Jerves and José E. Andrade. “A micro-mechanical study of peak strength and critical state”. In: *International Journal for Numerical and Analytical Methods in Geomechanics* (2015).

[33] Alex X. Jerves, Reid Y. Kawamoto, and José E. Andrade. “Effects of grain morphology on critical state: a computational analysis”. In: *Acta Geotechnica* (2015), pp. 1–11. ISSN: 1861-1133. DOI: 10.1007/s11440-015-0422-8. URL: http://dx.doi.org/10.1007/s11440-015-0422-8.

[34] Reid Kawamoto et al. “Level set discrete element method for three-dimensional computations with triaxial case study”. In: *Journal of the Mechanics and Physics of Solids* 91 (2016), pp. 1 –13. ISSN: 0022-5096. DOI: http://dx.doi.org/10.1016/j.jmps.2016.02.021. URL: http://www.sciencedirect.com/science/article/pii/S002250961530154X.

[35] K. Krabbenhoft et al. “Granular contact dynamics using mathematical programming methods”. In: *Computers and Geotechnics* 241-244 (2012), pp. 262–274.

[36] W. C. Krumbein. “Measurement and Geological Significance of Shape and Roundness of Sedimentary Particles”. In: *Journal of Sedimentary Research* 11.2 (1941), pp. 64–72.

[37] W. C. Krumbein and L. L. Sloss. *Stratigraphy and Sedimentation*. 2nd. San Francisco, CA, USA: Freeman and Company, 1963.

[38] N.P. Kruyt, O. Millet, and F. Nicot. “Macroscopic strains in granular materials accounting for grain rotations”. In: *Granular Matter* 16.6 (2014), pp. 933–944.

[39] N.P. Kruyt and L. Rothenburg. “Micromechanical definition of the strain tensor for granular materials”. In: *Journal of Applied Mechanics* 63.3 (1996), pp. 706–711.

[40] P. V. Lade and J. M. Duncan. “Elastoplastic stress-strain theory for cohesionless soil”. In: *Journal of the Geotechnical Engineering Division, ASCE* 101 (1975), pp. 1037–1053.

[41] T.A. Laursen. *Computational Contact and Impact Mechanics: Fundamentals of Modeling Interfacial Phenomena in Nonlinear Finite Element Analysis*. Springer, Berlin, 2002.

[42] X. Lee, W. C. Dass, and C. W. Manzione. "Characterization of the Internal Microstructure of Granular Materials Using Computerized Tomography". In: *Review of Progress in Quantitative Nondestructive Evaluation*. Ed. by D. O. Thompson and D. E. Chimenti. Vol. 12. New York: Plenum Press, 1993, pp. 1675–1680.

[43] N. Lenoir et al. "3D digital image correlation applied to X-ray microtomography images from triaxial compression tests on argillaceous rock". In: *Strain* 43 (2007), pp. 193–205.

[44] K.-W. Lim, K. Krabbenhoft, and J. E. Andrade. "On the contact treatment of non-convex particles in the granular elemnt method". In: *Computational Particle Mechanics* 1.3 (2014), pp. 257–275.

[45] Keng-Wit Lim et al. "Multiscale characterization and modeling of granular materials through a computational mechanics avatar: a case study with experiment". In: *Acta Geotechnica* (2015), pp. 1–11.

[46] A.E.H. Love. *A Treatise of Mathematical Theory of Elasticity*. Cambridge University Press, 1927.

[47] K. F. Man, K. S. Tang, and S. Kwong. *Genetic Algorithms: Concepts and Designs with Disk*. Ed. by M. Johnson and M. Grimble. 2nd. Secaucus, NJ, USA: Springer-Verlag New York, Inc., 1999. ISBN: 1852330724.

[48] H. Matsuoka and T. Nakai. "Stress-deformation and strength characteristics of soil under three different principal stresses". In: *Proceedings of the Japanese Society of Civil Engineers* 232 (1974), pp. 59–70.

[49] T. Matsushima and C. S. Chang. "Quantitative evaluation of the effect of irregularly shaped particles in sheared granular assemblies". In: *Granular Matter* 13.3 (2011), pp. 269–276.

[50] M.M Mehrabadi, M. Oda, and S. Nemat-Nasser. "On statistical description of stress and fabric in granular materials". In: *International Journal of Numerical Analysis on Methods of Geomechanics* 6 (1982), pp. 95 –108.

[51] T. Miller et al. "Eddy Viscosity in Dense Granular Flows". In: *Physical Review Letters* 111 (2013), p. 058002.

[52] Ian M. Mitchell. *A toolbox of level set mathods (Version 1.1)*. University of British Columbia. 2007.

[53] K. Miura et al. "Mechanical Characteristics of Sands with Different Primary Properties". In: *Soils and Foundations* 38.4 (1998), pp. 159–172.

[54] K. Miura et al. "Physical Characteristics of Sands with Different Primary Properties". In: *Soils and Foundations* 37.3 (1997), pp. 53–64.

[55] O. Mohr. “Welche umstände bedingen die elastizitätsgrenze und den bruch eines materiales?” In: *Zeitschrift des Vereines Deutscher Ingenieure* 44 (1900), pp. 1524–1530; 1572–1577.

[56] M. A. Mooney, R. J. Finno, and M. G. Viggiani. “A unique critical state for sand?” In: *Journal of Geotechnical and Geoenvironmental Engineering* 124 (1998), pp. 1100–1108.

[57] I. Newton. *Philosophiae Naturalis Principia Mathematica*. Ed. by J. Streater. 1st. London: for the Royal Society, 1687.

[58] M. Nitka et al. “A micro-macro (DEM-FEM) model of the behavior of granular solids”. In: *1st International Symposium on Computational Geomechanics (ComGeo I)*. Juan-les-Pins, France, 2009, pp. 38–48.

[59] M. Oda and K. Iwashita. *Mechanics of granular materials: an introduction*. Rotterdam, Netherlands: CRC Press / Balkema, 1999.

[60] M. Oda, K. Iwashita, and T. Kakiuchi. “Importance of particle rotation in the mechanics of granular materials”. In: *Powders and Grains*. Ed. by R. P. Behringer and J. T. Jenkins. Rotterdam, Netherlands: A. A. Balkema, 1997, pp. 207–210.

[61] M. Oda, T. Takemura, and M. Takahashi. “Microstructure in shear band observed by microfocus X-ray computed tomography”. In: *Géotechnique* 54 (2004), pp. 539–542.

[62] X. Oliver and C. Agelet de Saracíbar. *Mecánica de medios continuos para ingenieros*. Barcelona, Spain: Ediciones UPC, 2000.

[63] S. Osher and R. Fedkiw. *Level Set Methods and Dynamic Implicit Surfaces*. 2003 edition. Springer, 2003.

[64] Jin-Seo Park and Se-Jong Oh. “A New Concave Hull Algorithm and Concaveness Measure for n-dimensional Datasets”. In: *Journal of Information Science and Engineering* 28 (2012), pp. 587 –600.

[65] A. A. Peña, P. G. Lind, and H. J. Herrmann. “Modeling slow deformation of polygonal particles using DEM”. In: *Particuology* 6 (2008), pp. 506 –514.

[66] A. A. Peña et al. “Biaxial test simulations using a packing of polygonal particles”. In: *International Journal for Numerical and Analytical Methods in Geomechanics* 32 (2008), pp. 143–160.

[67] J. F. Peters et al. “Characterization of force chains in granular material”. In: *Physical Review E* 72 (2005), p. 041397.

[68] M. C. Powers. “A New Roundness Scale for Sedimentary Particles”. In: *Journal of Sedimentary Research* 23.2 (1953), pp. 117–119.

[69] D. C. Procter and R. R. Barton. “Measurements of the angle of interparticle friction”. In: *Géotechnique* 24 (1974), pp. 581–604.

[70] A. L. Rechenmacher and R. J. Finno. “Shear band displacements and void ratio evolution to critical state in dilative sands”. In: *Bifurcation and Instabilities in Geomaterials*. Ed. by J. F. Labuz and A. Drescher. A. A. Blakema Publishers, 2003, pp. 13–22.

[71] O. Reynolds. “On the Dilation of Media Composed of Rigid Particles in Contact, with Experimental Illustrations”. In: *Philosophical Magazine* 20 (1885), pp. 469 –481.

[72] L. Rothenburg and R. J. Bathurst. “Analytical study of induced anisotropy in idealized granular materials”. In: *Géotechnique* 39 (1989), pp. 601–614.

[73] L. Rothenburg and R. J. Bathurst. “Micromechanical features of granular assemblies with planar elliptical particles”. In: *Geotechnique* 42.1 (1992), pp. 79–95.

[74] L. Rothenburg and A.P.S. Selvadurai. “A micromechanical definition of the Cauchy stress tensor for particular media”. In: *Mechanics of Structured Media*. Ed. by A. P. S. Selvadurai. Amsterdam: Elsevier, 1981, pp. 469–486.

[75] P. W. Rowe. “The stress-dilatancy relation for static equilibrium of an assembly of particles in contact”. In: *Proceedings of The Royal Society A: Mathematical, Physical and Engineering Sciences* 269.1339 (1962), pp. 500–527.

[76] Reuven Y. Rubinstein and Dirk P. Kroese. *Simulation and the Monte Carlo method*. 2nd. John Wiley & Sons Ltd., 2008.

[77] J. C. Santamarina and G. C. Cho. “Soil behaviour: The role of particle shape”. In: *Advances in geotechnical engineering: The Skempton Conference*. Ed. by R. J. Jardine, D. M. Potts, and K. G. Higgins. Vol. 1. London: Thomas Telford Ltd, 2004, pp. 604–617.

[78] M. Satake. “A discrete-mechanical approach to granular materials”. In: *International Journal of Engineering Science* 30.10 (1992), pp. 1525–1533.

[79] M. Satake. “Tensorial form definitions of discrete-mechanical quantities for granular assemblies”. In: *International Journal of Solids and Structures* 41.21 (2004), pp. 5775–5791.

[80] G. De Saxce, J. Fortin, and O. Millet. “About the numerical simulation of the dynamics of granular media and the definition of the mean stress tensor”. In: *Mechanics of Materials* 36.12 (2004), pp. 1175–1184.

[81] A. Schofield and P. Wroth. *Critical State Soil Mechanics*. New York: McGraw-Hill, 1968.

[82] A. Skinner. “A note on the influence of interparticle frction on the shearing strength of a random assembly ofd spherical particles”. In: *Geotechnique* 19.1 (1969), pp. 150–157.

[83] D.W. Taylor. *Fundamentals of Soil Mechanics*. New York: Wiley, 1948.

[84] X. Tu and J. E. Andrade. “Criteria for static equilibrium in particulate mechanics computations”. In: *International Journal for Numerical Methods in Engineering* 75 (2008), pp. 1581–1606.

[85] I. Vlahinic et al. “Towards a more accurate characterization of granular media: extracting quantitative descriptors from tomographic images”. English. In: *Granular Matter* (2013). doi:10.1007/s10035-013-0460-6, pp. 1–13. ISSN: 1434-5021.

[86] H. Wadell. “Volume, Shape, and Roundness of Rock Particles”. In: *The Journal of Geology* 40.5 (1932), pp. 443–451.

[87] O. R. Walton and R. L. Braun, eds. *Simulation of rotary-drum and repose tests for frictional spheres and rigid sphere clusters*. Nov. 1993.

[88] R.G. Wan and P.J. Guo. “Stress dilatancy and fabric dependencies on sand behavior”. In: *Journal of Engineering Mechanics* 130.6 (2004), pp. 635–645.

[89] L. Wang, J. Y. Park, and Y. Fu. “Representation of real particles for DEM simulation using X-ray tomography”. In: *Construction and Building Materials* 21 (2005), pp. 338–346.

[90] J. Weber. “Recherches concernant les contraintes intergranulaires dans les milieux pulvérulents”. In: *Bulletin de Liaison des Ponts-et-Chaussees* 20 (1966), pp. 1 –20.

[91] C. Wellmann, C. Lillie, and P. Wriggers. “Homogenization of granular material modeled by a three-dimensional discrete element method”. In: *Computers and Geotechnics* 35 (2007), pp. 394–405.

[92] D. M. Wood. *Soil Behaviour and Critical State Soil Mechanics*. Cambridge University Press, 1990.

[93] A. Yamaji. *An Introduction to Tectonophysics: Theoretical Aspects of Structural Geology*. TERRAPUB, 2003.

[94] B. Zhou and J. Wand. “Random generation of natural sand assembly using micro x-ray tomography and spherical harmonics”. In: *Géotechnique Letters* 5 (2015), pp. 6–11.

[95] Bo Zhou, Jianfeng Wang, and Budi Zhao. “Micromorphology characterization and reconstruction of sand particles using micro X-ray tomography and spherical harmonics”. In: *Engineering Geology* 184 (2015), pp. 126–137.

Appendix A

CRITICAL STATE INDEPENDENCE ON μ

- *Sliding*, if all the particles in the CCB are sliding, then from expression 2.12 and 2.13, we have

$$\dot{u}_t^\alpha = \dot{\delta}^\alpha u_r^\alpha = -\frac{\dot{\delta}^\alpha}{\mu k}\left(\sum_{\beta=0}^{\alpha-1}|f_t^\beta| + \frac{1}{2}|f_t^\alpha|\right)$$

but, note that, in this case, every $|f_t^\beta| = \mu k \Delta_r^\beta$, and $|f_t^\alpha| = \mu k \Delta_r^\alpha$, so the last expression becomes

$$\dot{u}_t^\alpha = \dot{\delta}^\alpha u_r^\alpha = -\dot{\delta}^\alpha\left(\sum_{\beta=0}^{\alpha-1}\Delta r^\beta + \frac{1}{2}\Delta r^\alpha\right)$$

and $\dot{u}_t^\alpha$ *does not depend on the inter-particle friction coefficient,* μ.

- *Rotation and rolling*, if all the particles in the CCB are either rotating or rolling, or under any combination of these two submechanisms. Then, from expression 2.12 and 2.13, and for $\dot{\delta}^\alpha > 0$ (clockwise) and $\dot{\delta}^\alpha < 0$ (counter-clockwise), we have

$$\dot{u}_t^\alpha = \dot{\delta}^\alpha u_r^\alpha < -\frac{\dot{\delta}^\alpha}{\mu k}\left(\sum_{\beta=0}^{\alpha-1}|f_t^\beta| + \frac{1}{2}|f_t^\alpha|\right) \quad \text{and} \quad \dot{u}_t^\alpha = \dot{\delta}^\alpha u_r^\alpha > -\frac{\dot{\delta}^\alpha}{\mu k}\left(\sum_{\beta=0}^{\alpha-1}|f_t^\beta| + \frac{1}{2}|f_t^\alpha|\right) \tag{A.1}$$

respectively. Thus, note that it is enough to have only one $|f_t^\beta| < \mu f_r^\beta$ or only one $|f_t^\alpha| < \mu f_r^\alpha$ to satisfy these last inequalities. Then, note as well, that the contact points at which $|f_t^\beta| < \mu f_r^\beta$ or $|f_t^\alpha| < \mu f_r^\alpha$, do not depend on μ, and if there were any sliding contact points for which $|f_t^\beta| = \mu f_r^\beta$ or $|f_t^\alpha| = \mu f_r^\alpha$, then those contact points would depend on μ, but by the same argument used for the sliding case, $\dot{u}_t^\alpha$ *do not depend on* μ.

- *Small values of* μ, in expressions (A.1), note that when $\mu \to 0$, then $|\dot{\delta}^\alpha||f_t^\beta| \leq |\dot{\delta}^\alpha|\mu k \Delta r^\beta \to 0$ and $|\dot{\delta}^\alpha||f_t^\alpha| \leq |\dot{\delta}^\alpha|\mu k \Delta r^\alpha \to 0$ at a faster or equal rate than

$\mu k \to 0$, due to the fact that $|\dot{\delta}^{\alpha}|$, Δr^{α}, $\Delta r^{\beta} \ll 1$. Thus,

$$\text{when} \quad \mu \to 0 \quad , \quad \text{then} \quad \underbrace{\dot{u}_t^{\alpha} = \dot{\delta}^{\alpha} u_r^{\alpha} \to 0}_{\text{static (trivial)}} \quad \text{or} \quad \underbrace{\dot{u}_t^{\alpha} = \dot{\delta}^{\alpha} u_r^{\alpha} \to \mp\infty}_{\text{sliding (slipping)}}$$

and $\dot{u}_t^{\alpha}$ *is sensitive to values of* μ.

Finally, since this applies for any closed-connected boundary (CCB), and since the bulk (macroscopic) behavior is an average of the behavior of all the sub-domains enclosed by their corresponding CCB's in a given assembly of particles. Then, this proof holds for any subdomain of a two-dimensional array of discs undergoing critical state, and vice versa.

Appendix B

LEVEL SET DISCRETE ELEMENT METHOD

Taken from: *Journal of the Mechanics and Physics of Solids* [34].

B.1 Level set functions

A level set function is a scalar-valued implicit function $\phi(\boldsymbol{p})$ whose value is the signed distance from a point $\boldsymbol{p}$ to an interface [63]. In the context of LS-DEM, the interface is the particle's surface. Consider a grain particle surface such as the one in Figure B.1(a). Contour lines can be added around the grain surface as in Figure B.1(b). These contour lines represent the distance or 'elevation' from the grain surface, positive outside the grain and negative inside the grain. Next, a grid can be superimposed over the contours as in Figure B.1(c) and the elevation can be found at each grid point. Figure B.1(d) illustrates the elevation at each grid point, and this is the level set function which is stored in computer memory and is the geometric basis of LS-DEM.

Although level set functions can be constructed through the method above, i.e., using point-distance formulas to arrive at Figure B.1(d), all of the level set functions in the present work were generated from XRCT images of experiments on real grains using level set-based imaging algorithms in [85].

Through interpolation of values at surrounding grid points, the value of the level set function at any point can be evaluated (Figure B.1(e)). Define $\Omega^+ = \{\boldsymbol{p} \mid \phi(\boldsymbol{p}) > 0\}$ the outside of the grain and $\Omega^- = \{\boldsymbol{p} \mid \phi(\boldsymbol{p}) < 0\}$ the inside of the grain. Then, the original grain surface (Figure B.1(f)) can be reconstructed by finding the set of points $\partial\Omega = \{\boldsymbol{p} \mid \phi(\boldsymbol{p}) = 0\}$ (the "zero level set") via interpolation.

B.2 Interpolation in level set functions

For use in the level set discrete element method, we must be able to compute two quantities from a level set function ϕ: its value $\phi(\boldsymbol{p})$ and its gradient $\nabla\phi(\boldsymbol{p})$ at any point $\boldsymbol{p}$ within its grid boundaries. This is done through interpolation of values of the discretized level set function at grid points surrounding $\boldsymbol{p}$. Any order of interpolation can be used, but linear interpolation was used here for its simplicity and speed. Let:

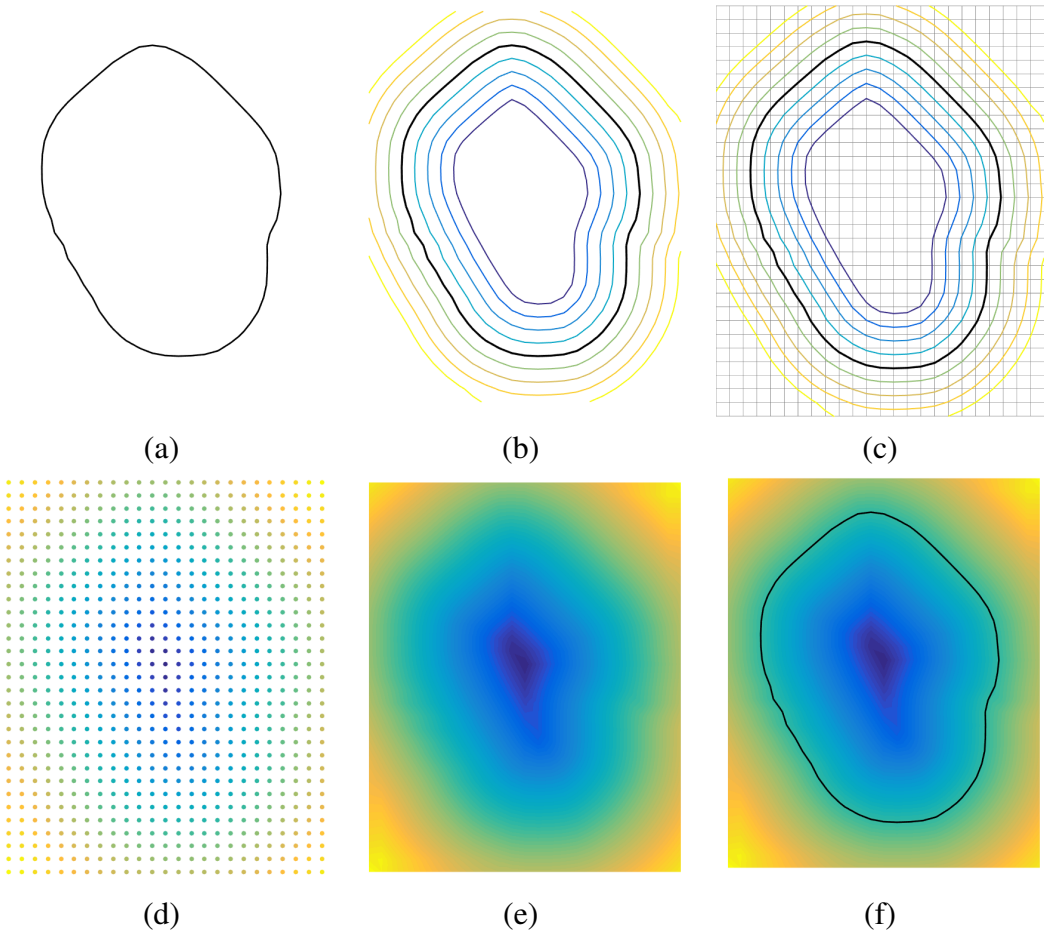

Figure B.1: Illustration of a level set function. (a) Grain particle surface. (b) Contour lines representing signed distance from surface. (c) Superimposition on grid. (d) Discretized level set function. (e) Level set function with interpolation between grid points. (f) Reconstruction of original grain surface via interpolation. Note that the level set functions shown here are 2D for illustrative purposes only.

1. ϕ be stored on a uniform grid with grid spacing g in all directions.

2. $\boldsymbol{p}$ be a point in space with components p_x, p_y, and p_z and surrounded by grid points $\boldsymbol{p}_{abc}$ with $a, b, c \in \{0, 1\}$ as shown in Figure B.2. Furthermore, let $\boldsymbol{p}_{000}$ have components (x_0, y_0, z_0).

3. $x = \dfrac{(p_x - x_0)}{g}$, $y = \dfrac{(p_y - y_0)}{g}$, $z = \dfrac{(p_z - z_0)}{g}$

4. $\phi_{abc} = \phi(\boldsymbol{p}_{abc})$ for convenience in notation.

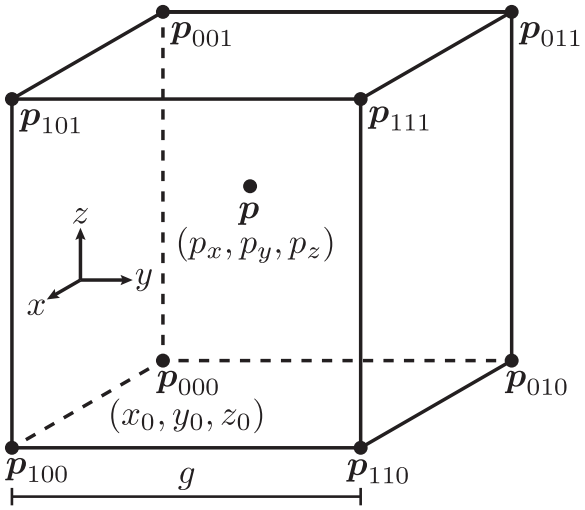

Figure B.2: Schematic of point $\boldsymbol{p}$ with surrounding grid points $\boldsymbol{p}_{abc}$.

Using trilinear interpolation to find $\phi(\boldsymbol{p})$,

$$\phi(\boldsymbol{p}) = \sum_{a=0}^{1}\sum_{b=0}^{1}\sum_{c=0}^{1} \phi_{abc}[(1-a)(1-x)+ax][(1-b)(1-y)+by][(1-c)(1-z)+cz] \tag{B.1}$$

The gradient of the level set function $\nabla\phi(\boldsymbol{p})$, using trilinear interpolation, is

$$\nabla\phi(\boldsymbol{p}) = \begin{pmatrix} \sum_{a=0}^{1}\sum_{b=0}^{1}\sum_{c=0}^{1} \phi_{abc}(2a-1)[(1-b)(1-y)+by][(1-c)(1-z)+cz] \\ \sum_{a=0}^{1}\sum_{b=0}^{1}\sum_{c=0}^{1} \phi_{abc}[(1-a)(1-x)+ax](2b-1)[(1-c)(1-z)+cz] \\ \sum_{a=0}^{1}\sum_{b=0}^{1}\sum_{c=0}^{1} \phi_{abc}[(1-a)(1-x)+ax][(1-b)(1-y)+by](2c-1) \end{pmatrix} \tag{B.2}$$

Note that the interpolation functions to find $\phi(\boldsymbol{p})$ and $\nabla\phi(\boldsymbol{p})$ are not functions of grid size. Therefore, the time complexity of these calculations are constant; they do not increase if ϕ is refined to a finer grid.

B.3 Inertial properties

The inertial properties, i.e., mass, center of mass, and moment of inertia, of a given grain must be known for its use in LS-DEM. These quantities are computed directly from the grain's level set function. Define the smoothed Heaviside function $H(\phi)$ as

$$H(\phi) = \begin{cases} 0 & \text{if } \phi < -\epsilon \\ \frac{1}{2}(1 + \frac{\phi}{\epsilon} + \frac{\sin(\frac{\pi\phi}{\epsilon})}{\pi}) & \text{if } -\epsilon < \phi < \epsilon \\ 1 & \text{if } \phi > \epsilon \end{cases} \tag{B.3}$$

where ϵ is a smoothness parameter. $\epsilon = 1.5$ was used in the present work. The mass of a grain of uniform density ρ and grid spacing g represented by level set function ϕ is

$$m = \rho g^3 \sum_{i=1}^{I} \sum_{j=1}^{J} \sum_{k=1}^{K} H(-\phi(x_i, y_j, z_k)) \tag{B.4}$$

where $\phi(x_i, y_j, z_k)$ is the value of ϕ at grid point (x_i, y_j, z_k), and I, J, and K are the number of grid points in the x, y, and z directions, respectively, of ϕ. In other words, the mass is proportional to the summation of $H(-\phi)$ over every grid point of ϕ. The components of its center of mass are

$$\begin{aligned} c_x &= \frac{\rho g^3}{m} \sum_{i=1}^{I} \sum_{j=1}^{J} \sum_{k=1}^{K} H(-\phi(x_i, y_j, z_k)) x_i \\ c_y &= \frac{\rho g^3}{m} \sum_{i=1}^{I} \sum_{j=1}^{J} \sum_{k=1}^{K} H(-\phi(x_i, y_j, z_k)) y_j \\ c_z &= \frac{\rho g^3}{m} \sum_{i=1}^{I} \sum_{j=1}^{J} \sum_{k=1}^{K} H(-\phi(x_i, y_j, z_k)) z_k \end{aligned} \tag{B.5}$$

Finally, the components of its moment of inertia are

$$I_{11} = \rho g^3 \sum_{i=1}^{I}\sum_{j=1}^{J}\sum_{k=1}^{K} H(-\phi(x_i, y_j, z_k))[(y_j - c_y)^2 + (z_k - c_z)^2]$$

$$I_{22} = \rho g^3 \sum_{i=1}^{I}\sum_{j=1}^{J}\sum_{k=1}^{K} H(-\phi(x_i, y_j, z_k))[(x_i - c_x)^2 + (z_k - c_z)^2]$$

$$I_{33} = \rho g^3 \sum_{i=1}^{I}\sum_{j=1}^{J}\sum_{k=1}^{K} H(-\phi(x_i, y_j, z_k))[(x_i - c_x)^2 + (y_j - c_y)^2]$$

$$I_{23} = I_{32} = -\rho g^3 \sum_{i=1}^{I}\sum_{j=1}^{J}\sum_{k=1}^{K} H(-\phi(x_i, y_j, z_k))(y_j - c_y)(z_k - c_z)$$

$$I_{13} = I_{31} = -\rho g^3 \sum_{i=1}^{I}\sum_{j=1}^{J}\sum_{k=1}^{K} H(-\phi(x_i, y_j, z_k))(x_i - c_x)(z_k - c_z)$$

$$I_{12} = I_{21} = -\rho g^3 \sum_{i=1}^{I}\sum_{j=1}^{J}\sum_{k=1}^{K} H(-\phi(x_i, y_j, z_k))(x_i - c_x)(y_j - c_y)$$

B.4 Boundary node discretization

LS-DEM uses a node-to-surface contact algorithm that is utilized in finite element models [41] as well as discrete element models [4] for the handling of nonconvex particles with multiple contact points as well as computational ease, whereby nodes are seeded onto the surface $\partial\Omega$ of each particle (Figure B.3). The density of nodes on a given particle is a matter of choice and has implications on particle behavior; however, we find that seeding with a maximum node-to-node spacing of less than $d/10$ (roundness scale), where d is the particle diameter, is adequate to capture particle morphology as higher nodal densities have a negligible impact on behavior. Contact is then determined by checking each node of a master particle against the boundary of a slave particle for penetration. Because each node is checked for contact, the computational cost of contact is proportional to of the number of nodes seeded onto the master particle. Note that the number of nodes seeded onto a particle does not change its underlying geometry, which is defined by its level set function, unlike polyhedra and clumping methods where changing the number of vertices or spheres completely modifies their geometries. Thus, more advanced schemes such as adaptive seeding near areas of contact during time integration are possible if such precision is desired.

B.5 Contact

As mentioned in the previous section, contact in LS-DEM is handled through a node-to-surface contact algorithm. Let grain i have nodes $\boldsymbol{m}_a^i$ with $\{a \in \mathbb{Z} \mid 1 \leq$

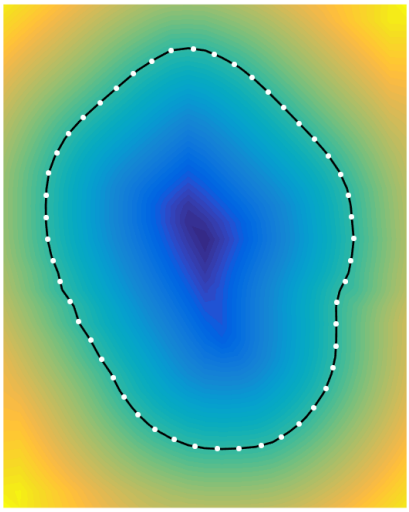

Figure B.3: Example of boundary node discretization with nodes in white seeded on the grain surface, shown in 2D for illustrative purposes only.

$a \leq A\}$, where A is the number of nodes seeded onto i. Contact is determined between master grain i and slave grain j by checking all nodes $\boldsymbol{m}_a^i$ of grain i with the level set function ϕ^j of grain j. Then,

$$d_a^{j,\,i} = \phi^j(\boldsymbol{m}_a^i) \tag{B.6}$$

$$\hat{\boldsymbol{n}}_a^{j,\,i} = \frac{\boldsymbol{\nabla}\phi^j(\boldsymbol{m}_a^i)}{\|\boldsymbol{\nabla}\phi^j(\boldsymbol{m}_a^i)\|} \tag{B.7}$$

where $d_n^{j,\,i}$ and $\hat{\boldsymbol{n}}_a^{j,\,i}$ are the penetration distance and outward contact normal of j, respectively, between grains i and j at node $\boldsymbol{m}_a^i$ (see Figure B.4). These contact equations are very simple and easy to compute due to the formulation of the level set function, whose value at any point represents the distance from that point to the surface, and its gradient at any point represents, in principle, the unit outward normal at that point. However, due to the level set function's discrete nature, the magnitude of $\boldsymbol{\nabla}\phi^j(\boldsymbol{m}_a^i)$ is very close, but not equal, to unity and therefore is normalized.

If at least one node $\boldsymbol{m}_a^i$ of master grain i is penetrating slave grain j, that is, if $\exists \boldsymbol{m}_a^i \mid \phi^j(\boldsymbol{m}_a^i) < 0$, then we consider the two grains to be in contact, and thus, interparticle forces must be computed.

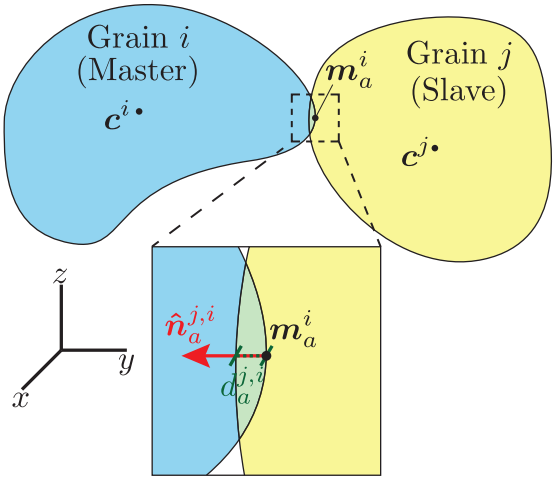

Figure B.4: Illustration of two contacting grains.

B.6 Forces and moments

To compute forces from penetrations, any contact model can be used, but we used a linear elastic contact model for the purposes of this study. Thus, the contact normal force contribution from node $\boldsymbol{m}_a^i$ on grain i is

$$\boldsymbol{F}_{n,a}^i = \begin{cases} -k_n d_a^{j,i}\, \hat{\boldsymbol{n}}_a^{j,i} & \text{if } d_a^{j,i} < 0 \\ \boldsymbol{0} & \text{else} \end{cases} \tag{B.8}$$

where k_n is the normal contact stiffness. By action and reaction, the contribution of contact normal force $\boldsymbol{F}_{n,a}^j$ from node $\boldsymbol{m}_a^i$ on grain j is

$$\boldsymbol{F}_{n,a}^j = -\boldsymbol{F}_{n,a}^i \tag{B.9}$$

The moment $\boldsymbol{M}_{n,a}^i$ contributed by the contact normal force $\boldsymbol{M}_{n,a}^i$ at node $\boldsymbol{m}_a^i$ on grain i is

$$\boldsymbol{M}_{n,a}^i = (\boldsymbol{m}_a^i - \boldsymbol{c}^i) \times \boldsymbol{F}_{n,a}^i \tag{B.10}$$

where $\boldsymbol{c}^i$ is the centroid of grain i. Similarly, the moment $\boldsymbol{M}_{n,a}^j$ contributed by the contact normal force at node $\boldsymbol{m}_a^i$ on grain j is

$$\boldsymbol{M}_{n,a}^j = (\boldsymbol{m}_a^i - \boldsymbol{c}^j) \times \boldsymbol{F}_{n,a}^j \tag{B.11}$$

where $\boldsymbol{c}^j$ is the centroid of grain j. For the calculation of frictional forces, LS-DEM uses a Coulomb friction model similar to [4, 23]. For a given node $\boldsymbol{m}_a^i$, frictional

forces (and related moments) only exist if $\boldsymbol{F}^i_{n,a} \neq \boldsymbol{0}$. The relative velocity $\boldsymbol{v}_a$ of node $\boldsymbol{m}^i_a$ to grain j is

$$\boldsymbol{v}_a = \boldsymbol{v}^i + \boldsymbol{\omega}^{\boldsymbol{i}} \times (\boldsymbol{m}^i_a - \boldsymbol{c}^i) - \boldsymbol{v}^j - \boldsymbol{\omega}^{\boldsymbol{j}} \times (\boldsymbol{m}^i_a - \boldsymbol{c}^j) \tag{B.12}$$

where $\boldsymbol{v}^i$, $\boldsymbol{v}^j$, $\boldsymbol{\omega}^{\boldsymbol{i}}$, and $\boldsymbol{\omega}^{\boldsymbol{j}}$ are the translational and angular velocities of grains i and j. The incremental shear displacement $\Delta \boldsymbol{s}_a$ is then

$$\Delta \boldsymbol{s}_a = [\boldsymbol{v}_a - (\boldsymbol{v}_a \cdot \hat{\boldsymbol{n}}^{j,\,i}_a)\hat{\boldsymbol{n}}^{j,\,i}_a]\Delta t \tag{B.13}$$

The shear force $\boldsymbol{F}^i_{s,a}$ on grain i contributed by node $\boldsymbol{m}^i_a$ is updated as such:

$$\boldsymbol{F}^i_{s,a} \leftarrow \boldsymbol{Z}\boldsymbol{F}^i_{s,a} - k_s \Delta \boldsymbol{s}_a \tag{B.14}$$

where $\boldsymbol{Z}$ is the rotation matrix that rotates the normal vector $\hat{\boldsymbol{n}}^{j,\,i}_a$ at the current timestep to the normal vector at the previous timestep and k_s is the shear contact stiffness. The Coulomb friction law dictates $\boldsymbol{F}^i_{s,a}$ be capped at a fraction of the normal force $\boldsymbol{F}^i_{n,a}$:

$$\boldsymbol{F}^i_{s,a} \leftarrow \frac{\boldsymbol{F}^i_{s,a}}{\|\boldsymbol{F}^i_{s,a}\|} \min(\|\boldsymbol{F}^i_{s,a}\|,\, \mu\|\boldsymbol{F}^i_{n,a}\|) \tag{B.15}$$

where μ is the interparticle friction coefficient. By action and reaction,

$$\boldsymbol{F}^j_{s,a} = -\boldsymbol{F}^i_{s,a} \tag{B.16}$$

The moment $\boldsymbol{M}^i_{s,a}$ contributed by node $\boldsymbol{m}^i_a$'s shear force on grain i is

$$\boldsymbol{M}^i_{s,a} = (\boldsymbol{m}^i_a - \boldsymbol{c}^i) \times \boldsymbol{F}^i_{s,a} \tag{B.17}$$

Similarly, the the moment $\boldsymbol{M}^j_{s,a}$ contributed by node $\boldsymbol{m}^i_a$'s shear force on grain j is

$$\boldsymbol{M}^j_{s,a} = (\boldsymbol{m}^i_a - \boldsymbol{c}^j) \times \boldsymbol{F}^j_{s,a} \tag{B.18}$$

The total contact force on grain i is found by summing all nodal contact forces:

$$\boldsymbol{F}^i_{tot} = \sum_{a=1}^{A} (\boldsymbol{F}^i_{n,a} + \boldsymbol{F}^i_{s,a}) \tag{B.19}$$

By action and reaction,

$$\boldsymbol{F}^j_{tot} = -\boldsymbol{F}^i_{tot} \tag{B.20}$$

The total contact moment on each grain is found by summing all nodal contact moments:

$$\boldsymbol{M}^i_{tot} = \sum_{a=1}^{A} (\boldsymbol{M}^i_{n,a} + \boldsymbol{M}^i_{s,a}) \tag{B.21}$$

$$\boldsymbol{M}^j_{tot} = \sum_{a=1}^{A} (\boldsymbol{M}^j_{n,a} + \boldsymbol{M}^j_{s,a}) \tag{B.22}$$

B.7 Motion

Given a grain's inertial properties and the force and moment on it, the translational velocity, angular velocity, position, and rotation of the grain are updated using an appropriate time integration scheme. In the present work, the scheme described in [4, 87] was used to update the positions of the center of mass and nodes of each grain, so it is not included here for the sake of brevity.

It is important to note that, to minimize computational cost, the level set function of each grain is never updated as it moves; each level set function remains in a reference configuration. To accommodate this, when computing contact, the nodes $\boldsymbol{m}^i_a$ of grain i (in the global frame) are moved temporarily into the reference configuration of grain j's level set function. From there, contact forces and moments are found (in the reference configuration of grain j) and then moved back to the global frame.